University of Cyprus
Department of Civil and Environmental Engineering

Master of Science (M.Sc.) Civil Engineering

In-situ permeability of the unsaturated zone of Nicosia Marl from field wetting experiments

Loizos Pogiatzis

Thesis submitted is in partial fulfilment of the degree of

Master of Science

June 2022

Table of Contents

ACKNOWLEDGMENTS

I would like to thank the supervisor of this thesis, Dr. Dimitrios Loukidis, for his guidance and cooperation during the course of the research. I would also like to thank the member of the examination committee, Dr. Panos Papanastasiou for the time he allocated for the evaluation of my thesis.

Finally, I would like to extend my deepest gratitude to the members of the research team of the project EXPASOL at the University of Cyprus, Mr. Thrasivoulos Stylianou, Dr. Ploutarchos Tzampoglou and Dr. Georgia Lazarou, since without them this thesis would have not been made possible.

ABSTRACT

The construction of infrastructure in areas with problematic ground conditions, such as the expansive soil of Nicosia marl in Cyprus, points to large economic losses. This research investigates hydraulic and water retention properties of Nicosia marl, namely the in-situ permeability and the hysteretic soil-water characteristic curve, in an effort to understand the potential of infiltration and migration of rainwater inside the unsaturated zone of the soil profile.

To achieve this, first the Nicosia marl was examined by laboratory testing after field sampling from three different sites at the University of Cyprus campuses for the determination of the soil-water characteristic curve using a chilled mirror hygrometer. Then, the data acquired by installed field volumetric water content and matric suction monitoring sensors were used in FE simulations for the back calculation of the in-situ permeability in both vertical and horizontal direction. The results indicate that the in-situ permeability is 3 to 4 orders of magnitude larger than the one measured in the laboratory on intact samples. This is attributed to the presence of the shrinkage cracks and the inherent structural fissures of the material.

1. INTRODUCTION

Most structures located in areas where expansive soils are prevalent are quite likely to show failures with time that are very costly to repair. For example. the average annual cost for the period 1974-2006 is estimated to be 2.1 million euros for the Nicosia region alone and 10 to 20 million euros per year for the whole of Cyprus, much higher than the cost of other natural disasters (Lazarou, 2020), and if not addressed in time they can even become dangerous.

The term expansive describes clay soils that absorb and lose water in wet and dry conditions, respectively, with simultaneous intense development of expansion-shrinkage. The associated volumetric changes are commonly reflected in damages to the foundations and structures (Fig. 1). These volumetric deformations are directly related to suction changes when soils are not fully saturated. Unsaturated soil is a material whose ratio of the volume of voids occupied by water to the total volume of voids is less than one.

Expansive clays exhibit the phenomenon of volumetric deformation due to electrostatic forces and van der Waals forces. Due to these forces, clay when in contact with water binds with it, increasing the thickness of the diffuse double layer (Fig. 7) and consequently their volume. During a drying phase, the diffuse double layer thickness is reduced, as well as their volume.

Figure 1. Examples of damage to structures due to uneven settlement of their foundations due to their construction in expansive soils.

One type of soil that exhibits this behavior is the marl of the Nicosia formation, which outcrops in large areas of the island of Cyprus. Marl is a cohesive geomaterial that is a mixture of calcite and clay, in which the percentage of calcium carbonate ($CaCO_3$) ranges between 35 - 65%. The water adsorption capacity of this formation is due to its high content of clay minerals, especially montmorillonite.

In Cyprus, swelling behavior is observed during the rainy-winter months, which is followed by the shrinkage during the dry-summer months. Seasonal fluctuations in the degree of soil saturation take place within the so-called active zone, the depth of which varies between 2 and 8 m from the soil surface (Lazarou, 2020).

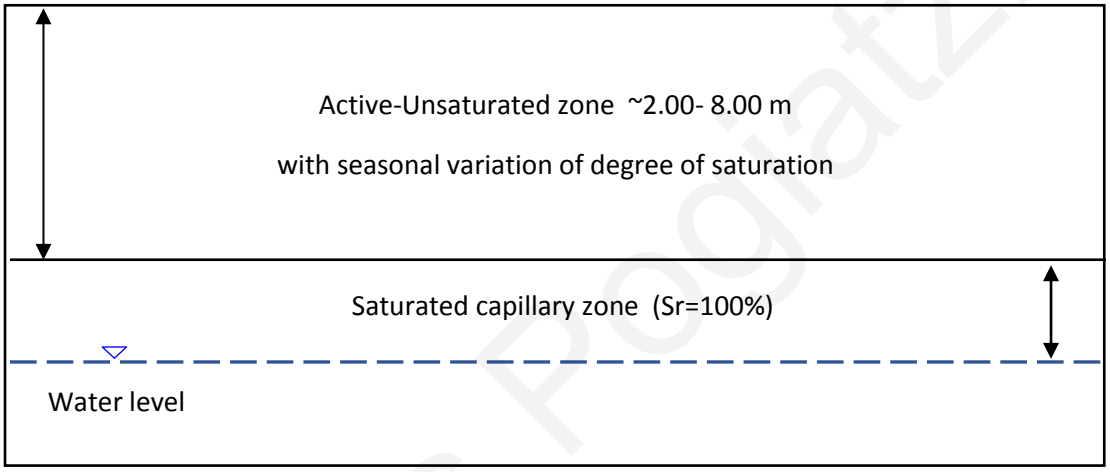

Figure 2. Schematic representation of the active zone of unsaturated condition.

For the study of soils that show a high potential for volume change due to seasonal changes in moisture content, the monitoring of ground moisture changes over time is particularly important. To achieve this, it is necessary to construct and study the soil-water characteristic curve (SWCC) which is defined by the mass of water in the soil the pore water energy state. This is the most important property associated with expansive soil behavior, and one of the most important tools used for the quantification of suction and for the determination of soil mechanical parameters and hydraulic characteristics.

Lately suction in expansive soils under unsaturated conditions has been considered as an independent stress variable and widely used in geotechnical engineering to evaluate the potential failure of foundations and in slope stability analysis, amongst other (Eyo et al., 2020).

In order to better understand the geotechnical behavior of this type of soil, leading eventually to the reduction of dangerous failures and the decrease of the total annual cost of damages in Cyprus, the significant effect of suction in relation to the moisture content of these soils and hence the pertinent mechanisms, in the context of this work the in-situ permeability of Nicosia marl in the unsaturated zone, was studied by numerical simulation (FEM) analyses of field data from ground monitoring stations, ground wetting experiments, laboratory and other in-situ work, which included the drilling of exploratory boreholes, measurements of matric and total suction, and determination of the soil-water characteristic curves.

Initially, using the samples collected during field work (Fig. 13), the properties of the formation study were determined. Also, in the context of research project EXPASOL at the University of Cyprus, the data of 3 wetting experiments with continuous recordings of the volumetric moisture content and matric suction, thanks to the installation of electronic sensors in the subsoil at 3 different Sites with Nicosia marl outcrops, were used to establish the in-situ hydraulic characteristics of Nicosia marl through back-calculations using finite element analyses in Plaxis 2D. The objective of the in-situ permeability testing is to determine the in-situ horizontal and vertical permeability of the Nicosia marl.

2. KNOWLEDGE BACKGROUND

2.1 Geology of Cyprus

The core of the geology of Cyprus is the 92-million-year-old Troodos ophiolite complex. The geological evolution of the area where Cyprus is today was submarine and it has five main tectonic episodes: (a) the genesis of the Troodos oceanic crust, (b) the attachment to it of older rocks (200 to 75 million years) on its southern and western margins (Mammonia Complex), (c) the tectonic calm that prevailed in the period from 75 to 10 million years, characterized by the underwater deposition of predominantly pelagic calcareous sediments and the gradual decrease of the depth of the sea basin d) the thrust of the Kyrenia mountain range to the north side of the Troodos Ophiolite and (e) the final elevation of the island in its current form.

Cyprus is divided into four geotectonic zones: the Troodos ophiolite which includes the Arakapas sequence, the Mammonia complex, the Kyrenia sequence and the autochthonous sedimentary sequence. The most important tectonic event that led to the creation of Troodos and the emergence of Cyprus from the sea, is the collision of the outskirts of the Arabian Peninsula with the sinking trench of the African Plate, over which Troodos was formed. This resulted in the detachment of the Troodos ophiolite and its counterclockwise rotation by 90^{o}, the pushing of the Mammonia complex on the curbs of the Troodos geotectonic zone and their merging into one unit. With the subsidence and the corresponding adjustments, the slabs moved further north so that their southern curbs were found in the area where the Kyrenia mountain range would eventually adhere. To the south of this region, tectonic calm prevailed, with marine sedimentation in sea basins that gradually became shallow, with the Troodos emerging slowly from the Miocene onwards.

The thrusting of the Kyrenia range was an important tectonic event, which occurred at the end of the Miocene and mainly affected the northern part of the region that would form Cyprus. It consistent of the pushing of a series of allochthonous limestones towards south, on the edges of the Troodos zone, folding and pushing all the new sediments encountered along the way. East of Cyprus, the Tethys Sea closed, and the Mediterranean Sea acquired almost its current shape. However, the African plate did not stop moving north. In the context of balancing the trends inside the Earth, the relative motion of the plates was differentiated, and their limits were adjusted. Thus, a new subduction zone was developed south and west of Cyprus and the two plates now slide parallel to each other to the east. In this geometric shape, as the African and

especially the Arabian plate moves under Turkey, it pushes it and forces it to move west along two main sliding faults. In this way the African plate sinks to the south of Cyprus which had a decisive effect on the genesis and geological evolution of the island. (Constantinou et al., 2002).

2.1.1 Messinian

The formation of Kalavasos consists of gypsum and gypsum marls which appear around the Troodos Mountains. Gypsum deposits, also known as evaporates, cover large areas, but their lateral continuity was interrupted as result of tectonic and erosion. Gypsum and alite deposits (mineral salt) up to 2 Km thick have been discovered beneath the deeper parts of the Mediterranean. Evaporites formed in Messinian (Upper Miocene 7-5 m years) and represent a very important event in the area of the Mediterranean geological evolution, known as the "salinity crisis" of Messinian.

During this time the relative movement of the plates of Africa and Eurasia was such that brought about the closure of the Straits of Gibraltar and the severance of the Mediterranean by Atlantic Ocean. The evaporation was greater than the inflow of river water into the Mediterranean resulting in a drop in sea level well below to the Atlantic Ocean and the creation of extensive basins, in which gypsum and mineral deposits were deposited.

2.1.2 Pliocene

With the end of the Miocene and the beginning of the Pliocene, about 5 million years ago, and due to a change in the relative motion of the lithosphere plates of Africa and Eurasia, communication between the Mediterranean and the Atlantic Ocean was restored in the Straits of Gibraltar. Thus, the Mediterranean was flooded by the waters of the Atlantic. At the same time, the Cyprus Arc was reactivated, and the African plate began to sink under the Eurasian. From this time period the events accelerated, and Cyprus began to emerge at a more intense pace and to take its current form. The formation of Nicosia consists of sedimentary rocks deposited during this new sedimentation cycle, which began immediately with the opening of the Straits of Gibraltar and the flooding of the Mediterranean by Atlantic waters. These rocks, of course, sit in unconformity on the older geological formations of Cyprus. In this new cycle

of sedimentation, the deposited geomaterials were mainly marls with interferences of fine-grained and coarse-grained sandstones and calcarenites.

From the bottom up there is a gradual transition from fine-grained sediments to coarser, such as sandstones. This transition reflects the gradual rise of Cyprus and the continuous reduction of the depth of the sea basin. Typical occurrences of the formation exist in the wider area of Nicosia and in its full development the formation has a thickness of 900 m. It is subdivided into several members, consisting of fossilized yellow or gray-green marls, fossilized calcareous sandstone (calcarenites) and sandstone. The formation is rich in fossils of shells, mollusks, and tassels.

2.1.3 Nicosia Marl

The most important marl in Cyprus in relation to the built environment is the Pliocene marl of the Nicosia geological formation. The marl of Nicosia which deposited in a shallow sea environment during the Pliocene has a substantial thickness of several hundred meters and is divided in two parts. The two parts are clearly distinguished in color with the upper part having a characteristic khaki color and the lower one a gray color (Fig. 3). The upper part of this formation is particularly sandy and stiff.

Of particular importance is the marl's active zone, which extends to a depth of about 8 m from the soil surface, where the greatest seasonal fluctuations of natural humidity prevail. Despite the risk of the construction of structures on expansive soils such as Nicosia marl, many buildings are located on a surface layer overlying the marl, of coarse-grained soil of few meters in thickness, that drastically reduces the percentage of damages. Although the type of damage is also affected by the type of foundation (strip, spread, mat foundation), building on mat foundations was found to be more likely to cause extensive damage to the construction. (Lazarou, 2020).

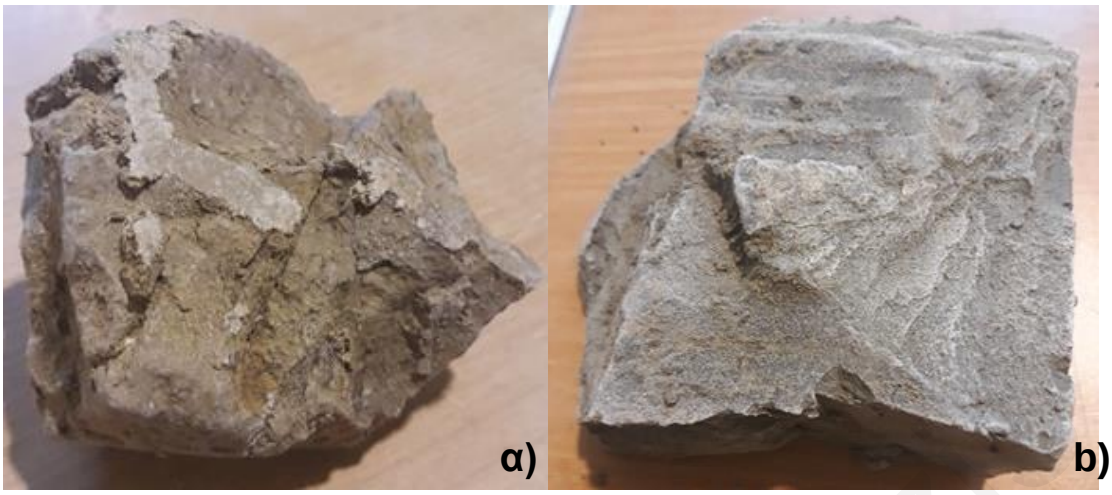

Figure 3. Nicosia Marl, a) brown-khaki marl and b) gray marl

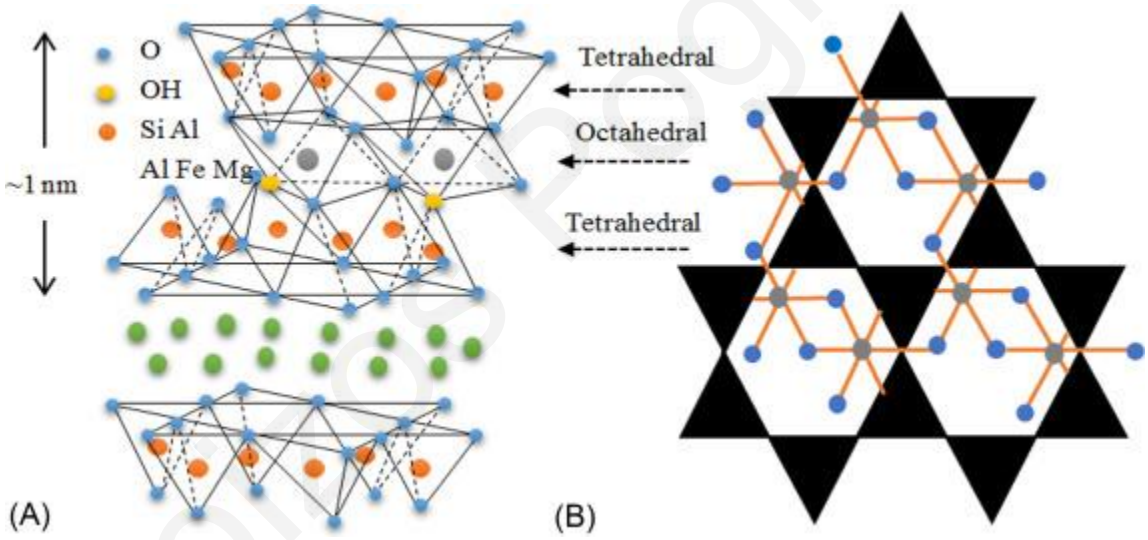

Figure 4. Montmorillonite crystal structure (Wang & Wang, 2019)

2.2 Clay minerology and structure

Clays mainly come from the erosion of aluminosilicate rocks. By corrosion and hydrolysis, the alkaline components are converted to soluble salts which move with the water and the hydrated aluminosilicate minerals, the free silicon oxide and the unchanged minerals remain in place.

These erosion products are transported after water and deposited at the bottom of the basin where the water ends, whether it is a riverbed, the bottom of a lake or the sea.

Most of the clay minerals (Fig. 5) are Hydrous Aluminium Silicates or Lamellar Aluminosilicates and they are extremely hydrophobic (Clinton, 2015). The term clay is used to describe a size (<0.002mm) or a class of a mineral. Their main structure consists of combinations of two units, the Aluminium or Magnesium Octahedron and the Silicon Tetrahedron, which are stacked together in sheets or in chains (Mitchell & Soga., 2005). Montmorillonites (Fig. 4,6) are clay minerals have a crystal structure with ratio of Aluminum - Silica - water of 1:4:1 and are characterized by the ability to absorb large amounts of water. Other elements also participate in their structure, such as Iron, Calcium, and Magnesium. Montmorillonite is the main clay mineral of bentonitic clays. Nicosia Marl reaches montmorillonite content of 25%. (Hobbs et al., 1986).

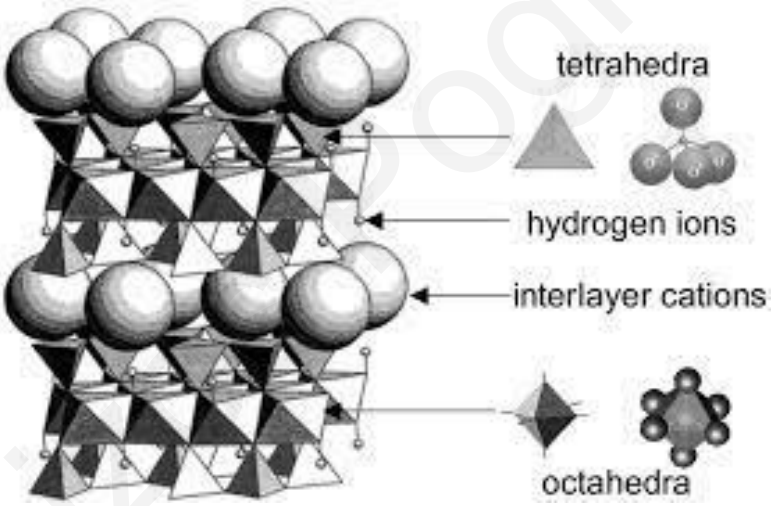

Figure 5. Clay mineral crystal structure (Williams & Shelley, 2010).

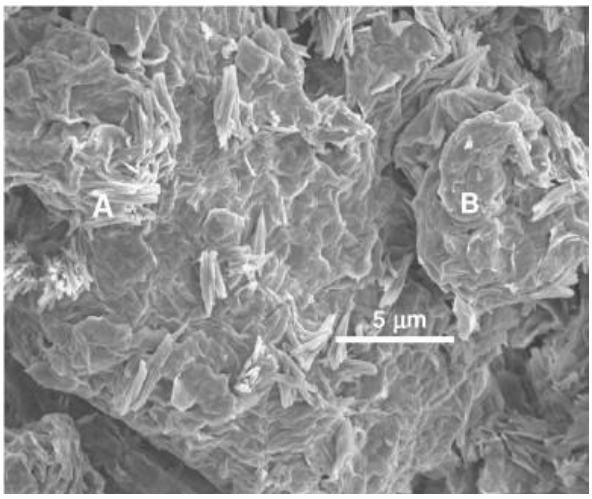

Figure 6. SEM image of Montmorillonite clay.

The diffuse double (Fig 7) layer is the charged surface of the particles and the adjacent distributed in the liquid, ionic charge, and according to the most successful theory for the description of the diffuse double layer, the Gouy-Chapman theory, ions form a layer of specifically adsorbed water, next to the particle surfaces and the double layer is diffuse beyond this layer. Flocculation, swelling potential and pore fluid changes, then can be predicted, considering factors such as particle forces, pH, and ion size.

As thicker the diffuse double layer is, the particles in suspension have less tendency to flocculate but more swelling pressure in expansive soils. Also, the higher the electrolyte concentration, the higher the compression of the diffuse double layer. In addition, high pH values lead to greater negative particle charge, and the orientation of water around the clay particles gives clay soils their plastic properties (Liaki, 2006). Thus, when an unsaturated clay soil gets wet, the extra amount of water results in an increase in the volume of the double layer, leading to an increase in the overall soil volume. Oppositely, when the material dries, the volume of the double layer decreases and as a result there is a decrease in the volume of the soil.

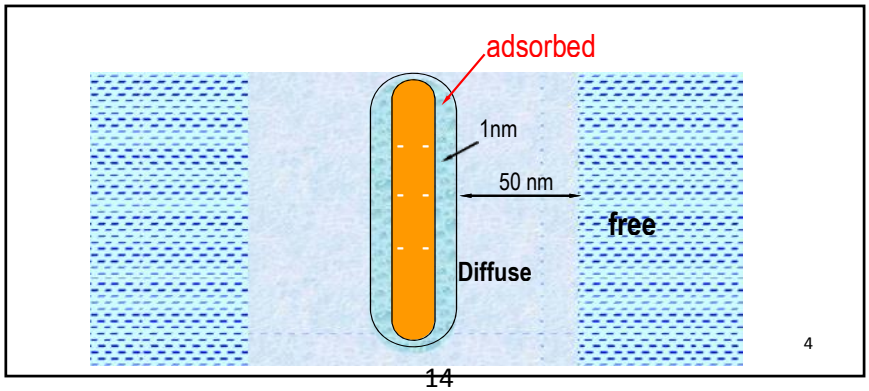

Figure 7. Clay particle in water.

Table 1. Volumes of water adsorbed in 1 nm thick double layers for saturated clays at a void ratio of 2.5. (Fernandez & Quigley, 1989)

Clay mineral	Specific surface (m^2/g)	Volume of absorbed water in DDL (% pore volume)
Kaolinite	20	2
Illite	100	9
Montmorillonite	800	70

.

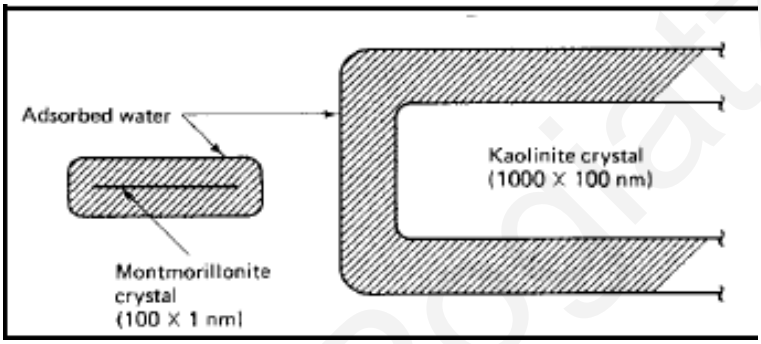

Figure 8. Relative sizes of absorbed water layers on sodium Montmorillonite and sodium Kaolinite.

Figure 8 shows a sodium Montmorillonite and Kaolinite crystal with layers of adsorbed water. The thickness of the adsorbed water is approximately the same, but because of the size differences, the montmorillonite will have much greater activity, higher plasticity, and greater swelling shrinkage and volume change due to loading.

In unsaturated soils, coefficient of hydraulic conductivity *k* depends significantly on suction, in contrast to fully saturated soils where it depends mainly on the void ratio. In saturated soils, *k* obtains its maximum value, while it decreases dramatically in dry conditions. Except the direct methods for its determination, the hydraulic permeability can also calculated theoretically utilizing the soil water characteristic curves, and the physical properties of the material such as mass and volume.

Hydraulic conductivity coefficient calculated by Flexible wall permeameter tests (Loukidis et al., 2020) conductivity *k* was found to be equal to 1.4×10^{-7} cm/sec and 6.4×10^{-9} cm/sec for the

samples obtained from brown-khaki marl from BH 1 at 4.5- 5.5, Test pit 1 (1.3 m) and a shallow sample from Site 2. (Loukidis et al., 2020).

2.3 Soil-Water Characteristic Curve

The wetting-drying phases of clay minerals play a very important role in the mechanical behavior of unsaturated soils, and they have been extensively studied by many researchers, (Likos & Lu, 2013) with the construction of the so-called soil–water characteristic curve (SWCC), also known as water retention curve.

Soil-water characteristic curves (SWCCs) describe the relation between volumetric water content (θ) and suction (s) and are known to exhibit hysteresis with respect to the wetting history (Fig. 9). Water content obtained along any drying path generally is greater than that obtained at the same suction along a wetting path. Suction for a given water content can vary by a factor of two or more depending on the history of wetting and drying. (Likos & Lu, 2013).

2.3.1 SWCC terminology and description

The key stress state variable for the SWCC description is soil suction, which consists of three components:

1. Matric suction (i.e., $u_a - u_w$, where u_a is the pore air pressure and u_w is the pore water pressure), which relates to the height of water capillary rise into an unsaturated soil.
2. Osmotic suction is resulting from the concentration of salts in the soil water.
3. Total suction: is the sum of matric and osmotic suctions.

The water content defines the amount of water contained within the pores of the soil. Volumetric water content θ_w (volume of water in soil divided by total volume of soil, or V_w/V) is most often used in the expression of the SWCC (Satyanaga et al., 2020). SWCC is usually plotted in a semi-logarithmic scale, i.e., volumetric water content is in arithmetic scale, and matric suction is in logarithmic scale. As we can see in Figure 9, SWCC can be described as three distinct stages - the transition stage, the boundary effect stage, and the residual stage. The slope of the curve on which the inflection point is found defines two separation points, namely

the air entry value (AEV) suction and the residual conditions (residual suction or residual water content). The AEV (or bubbling pressure) represents the suction value at which air begins to enter the soil's largest voids. The suction at the residual condition is termed the residual suction value (RSV) or residual soil suction and signifies the suction corresponding to the residual moisture content. The residual moisture content is the minimum moisture content beyond which there is no appreciable change in moisture with suction. It should be noted that if the wetting curve is considered then the point referred to as the water-entry value (WEV) is defined as the suction at which there is a significant increase in the water content as the wetting progresses. (Eyo et al., 2020).

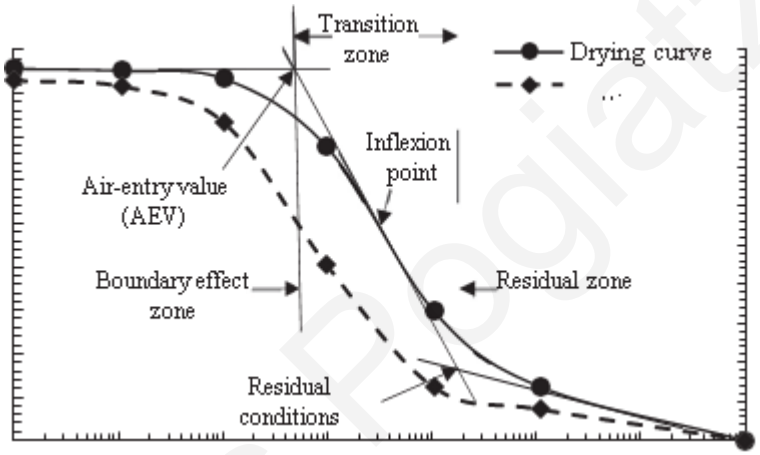

Figure 9. Typical features of the soil–water characteristic curve (SWCC). (Eyo et al., 2020)

2.3.2 Hysteresis in SWCCs

The relationship between the amount of water and matric suction (pore air pressure minus pore water pressure) in soil is not unique, and this phenomenon is known as hysteresis in SWCCs. Some reasons for the occurrence of the phenomenon can be changes in distribution, form, geometry, and connectivity of pores and entrapped air (Mady & Shein, 2020), such as the different radius of curvature of the menisci when the soil pores are filled and emptied of water. Specifically, during the drying phase of the soil material, the menisci that are formed have a small curvature and therefore there is a large suction value. On the contrary, during wetting phase, the radius of curvature is larger, with the consequence of a reduced suction.

The hysteresis adds considerable challenges to inclusion of the SWCC in constitutive models, analysis of boundary value problems, and design of unsaturated soil structures. Graphically, the position of a point on the SWCC relative to the water content and the matric suction axes depends on whether the soil was wetted or dried, the previous wetting and drying history, and the stress history of the soil. Since matric suction and the amount of water in the soil directly impact the soil skeletal stress, it stands to reason that the mechanical behavior of unsaturated soil is strongly dependent on the soil state relative to the SWCC (Miller et al., 2008).

2.4 SWCC mathematical expressions

Although in the technical literature there are many models for the mathematical representation of the soil-water characteristic curve (Table 2), the most widespread is the van Genuchten model (1980). According to the van Genuchten's (1980) expression, the SWCC has the following functional form:

$$\boldsymbol{S_e = \frac{\theta - \theta_r}{\theta_s - \theta_r} = [1 + (\alpha s)^n]^{-m}} \qquad (\boldsymbol{Eq.1})$$

where, S_e: effective saturation, s: matrix suction (kpa), θ_s: saturated volumetric water content, θ_r: residual volumetric water content and a, n, and m empirical fitting parameters. The a-parameter controls the point of inflection on the SWCC and bears a relation to the AEV of the soil. The n-parameter indicates approximately the pore size distribution of soils and hence controls the rate of desaturation (or absorption) as soon as the air entry is completed. This fitting parameter relates mainly to the slope portion of the SWCC. Meanwhile, the m-parameter relates to the portion of the SWCC that is close to the residual condition (residual moisture content and residual suction) and captures the overall symmetry of the SWCC (Eyo et al., 2020).

Table 2. Equations of the most common mathematical representations of SWCCs. (Lazarou, 2020).

Πηγή	Εξίσωση καμπύλης προσομοίωσης (S_r-s)	Εξίσωση καμπύλης προσομοίωσης (θ-s)
Burdine (1953)	$S_r = \frac{1}{\left[1+(as)^n\right]^{(1-2/n)}}$, (4.3)	$\theta = \theta_r + (\theta_s - \theta_r)\frac{1}{(1+as^n)^{1-2/n}}$, (4.4)
Gardner (1956)	$S_r = \frac{1}{1+as^n}$, (4.5)	$\theta = \theta_r + (\theta_s - \theta_r)\frac{1}{1+as^n}$, (4.6)
Brooks & Corey (1964)	$\begin{cases} S_r = 100\% & s < a \\ S_r = \left(\frac{s}{a}\right)^{-n} & s > a \end{cases}$ (4.7)	$\begin{cases} \theta = 1 & s < a \\ \theta = \theta_r + (\theta_s - \theta_r)\left(\frac{s}{a}\right)^{-n} & s > a \end{cases}$ (4.8)
Brutsaert (1966)	$S_r = \frac{1}{1+\left(\frac{s}{a}\right)^n}$, (4.9)	$\theta = \theta_r + (\theta_s - \theta_r)\frac{1}{1+\left(\frac{s}{a}\right)^n}$, (4.10)
Mualem (1976β)	$S_r = \frac{1}{\left[1+(as)^n\right]^{(1-1/n)}}$, (4.11)	$\theta = \theta_r + (\theta_s - \theta_r)\frac{1}{(1+as^n)^{1-1/n}}$, (4.12)
van Genuchten (1980)	$S_r = \frac{1}{\left[1+(as)^n\right]^m}$, (4.13)	$\theta = \theta_r + (\theta_s - \theta_r)\frac{1}{\left[1+(as)^n\right]^m}$, (4.14)
Boltzman (1984)	$\begin{cases} S_r = 100\% & s < a \\ S_r = \exp\left(\frac{a-s}{n}\right) & s > a \end{cases}$ (4.15)	$\begin{cases} \theta = 1 & s < a \\ \theta = \theta_r + (\theta_s - \theta_r)\exp\left(\frac{a-s}{n}\right) & s > a \end{cases}$ (4.16)
Fermi (1987)	$S_r = \frac{1}{1+\exp\left(\frac{s-a}{n}\right)}$, (4.17)	$\theta = \theta_r + (\theta_s - \theta_r)\frac{1}{1+\exp\left(\frac{s-a}{n}\right)}$, (4.18)
Fredlund & Xing (1994)	$S_r = \frac{1}{\left(\ln\left(e+\left(\frac{s}{a}\right)^n\right)\right)^m}$, (4.19)	$\theta = \theta_s\left(1-\frac{\ln\left(1+\frac{s}{s_r}\right)}{\ln\left(1+\frac{10^6}{s_r}\right)}\right)\frac{1}{\left[\ln\left(e+\left(\frac{s}{a}\right)^n\right)\right]^m}$, (4.20)

2.5 Plaxis 2D FEA Software

Plaxis 2D finite element program renders the van Genuchten's model with the following form:

$$S_r(s) = S_{r,res} + (1 - S_{r,res})\left[1 + (g_a \mid s\gamma_w \mid)\, g_n\right] g_c \qquad (Eq.\ 2)$$

where, Sr the degree of saturation, s the soil suction, γw the specific gravity of water, S_r, res the residual degree of saturation and g_a, g_c, ((g_c=1-g_n)/g_n) and g_n are the calibration parameters. (van Genuchten, , 1980), (Galavi, 2010).

3. FIELD WETTING EXPERIMENTS

Field wetting experiments were performed at three different sites (Fig. 10) where Nicosia khaki marl is outcropping in the context of the RPF research project EXPASOL. Two sites (Site 1 and Site 2) located in the main campus of the University of Cyprus (UCY) and one (Site 3) at the old UCY campus (Academia Park). Field work included site investigation, sampling, installation of instrumentation and execution of the wetting experiments. Three boreholes were drilled, one at each of the sites, from which samples were collected for the determination of the physical and mechanical properties of Nicosia marl.

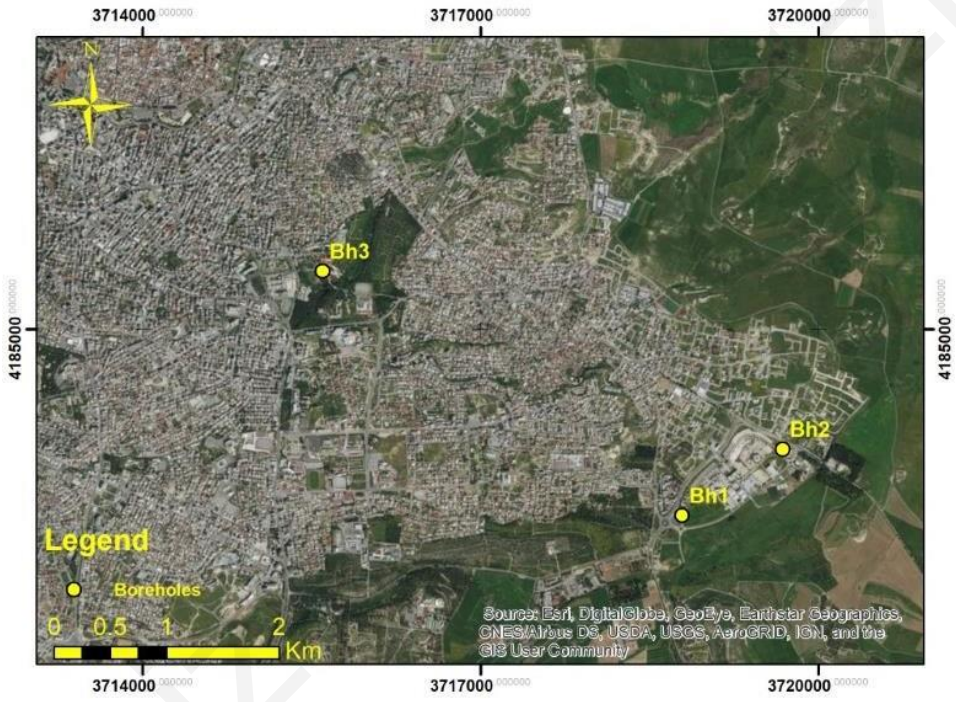

Figure 10. Map of exploratory boreholes at research sites.

3.1 Field Work for Ground Monitoring Station at Site 1

Site 1 is located in the new campus (southeast of Nicosia). The drilling work started on 4/4/2019 and was undertaken by the Cyprus Geological Survey Department (GSD). The drilling (Fig. 11) was done using continuous flight auger (without use of drilling mud or water), and the final depth of the drilling reached 5.50 meters. The observed soil stratigraphy column of BH 1 is shown in Figure 12. The first 1.5m consists of yellowish silty clayey marl, with an

incremental increase of calcite with depth and a decrease in clay content and until 5.5 m. No water level was observed.

For the determination of the properties of this formation several soil samples were taken (Fig. 13), in both bulk (every 0.5 m) and undisturbed at 1.5 m, 4.0 m, 4.5 m and 5.0 m U100 samplers 0.5m long. The appropriate sealing procedure with molten paraffin wax was followed to prevent U100 samples from drying out. The laboratory testing included gradation, Atterberg limits, calcite content, permeability, and water-retention characteristics (SWCC) of the formation.

Figure 11. Drilling at Site 1 (BH 1)

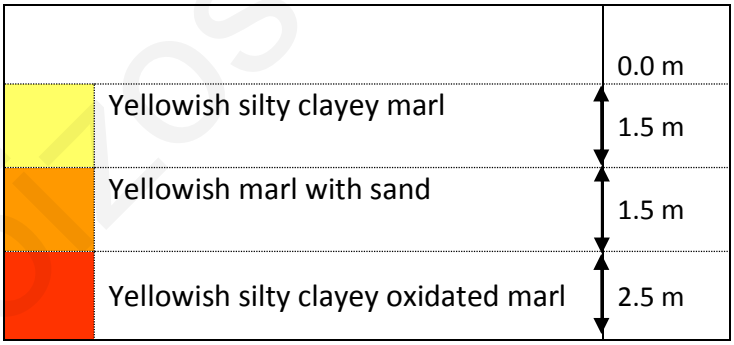

Figure 12. Stratigraphic column of BH 1 at the area of Site 1 (new UCY campus)

Figure 13. Bulk and undisturbed U100 samples from the boreholes.

Figure 14. Schematic of Site 1 and the new UCY campus showing test pit 1, borehole BH1 and mat foundation.

During 23-30 July 2019, a ground monitoring station (test pit 1) nearby an instrumented square concrete foundation (Fig. 14). Two types of ground sensors were installed:

1. TEROS 21 porous block FDR sensor by Meter Group for matric suction measurements. (Fig. 16).
2. TEROS 12 frequency domain reflectometry sensor by Meter Group for volumetric water content measurements.

To ensure good contact point between the matric suctions sensors and the ground, the sensors were first covered with remolded material from the excavation (Fig. 16) and then placed firmly into holes carved on the vertical wall of the excavation.

Figure 15. Site 1 with model mat foundation. Red arrow shows the location of test pit 1 and blue arrow shows the location of the wetting experiment.

Figure 16. TEROS 21 matric suction sensors covered with remolded soil before installation.

The test pit has dimensions 1 m width and 2 m length. Two pairs of Teros 21 and Teros 12 sensors was placed at 0.5 m depth from the surface and one pair at 1.5 m depth on the east side wall of the pit.

During the excavation large blocks of soil samples and undisturbed samples were collected in order to be used for the laboratory work. The pit was backfilled with native material (marl) which was compacted using a vibratory plate compactor. A side wall sealing procedure was also followed to avoid effects on the sensors by moisture migrating from the disturbed soil (backfill) (Fig. 18).

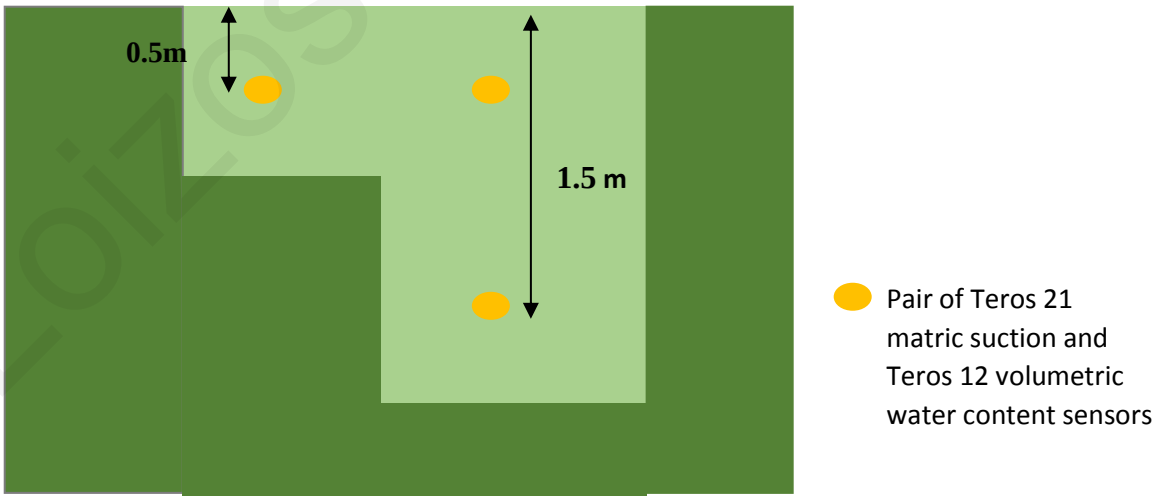

Figure 17. Front view of the excavation (test pit 1) side wall showing arrangement of ground sensors.

Figure 18. Backfilling and compacting test pit 1.

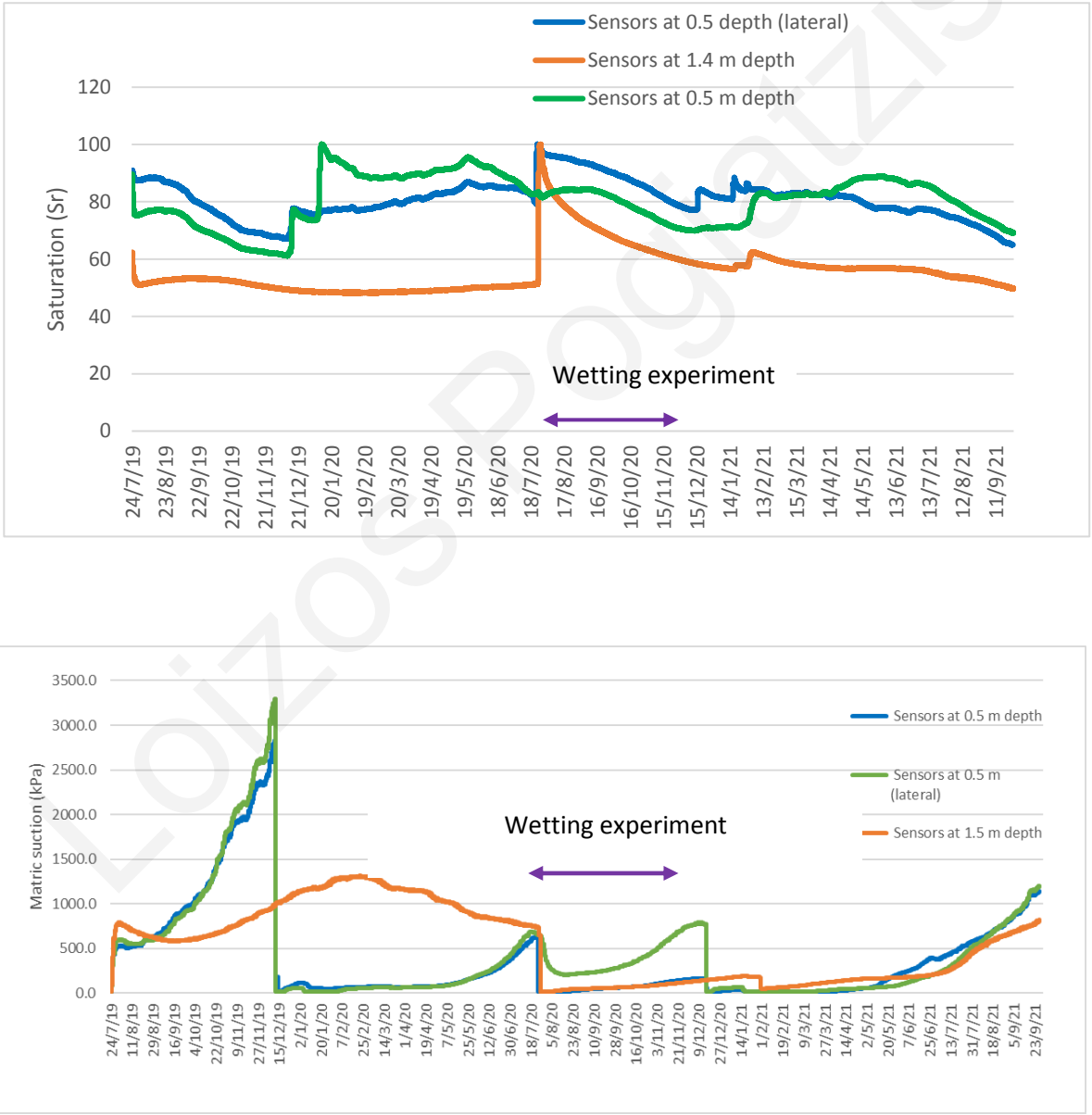

Figure 19. Field sensors data at Site 1 for the time period 7/2019 – 9/2021.

Figure 19 shows the continuous time history of inferred degree of saturation and matric suction for approximately 2 years, from the time of installation to September 2021. The upper pairs of sensors reach full saturation (zero matric suction values) in December of 2019 mainly because of water infiltration in the soil through desiccation cracks, with the previously recorded peak values being of the order 2-3 MPa. The wetting experiment started on 20 July 2020, during the dry summer period, and quickly reached full saturation state at both elevations. The data coming from the ground monitoring station continue to be recorded even after the conclusion of the wetting experiment and showed a continuous desaturation (with some fluctuations due to rainwater percolation during the following winter).

For the field wetting experiment, first the area was thoroughly cleaned and then a plastic container, from which the bottom was removed, was placed in the area above the sensors, the two pairs of sensors that lie at different depths. This container with dimensions of 35 cm in height and 48 cm in diameter was initially firmly attached inside an indentation made on the ground surface using marl putty and then then covered laterally with plastic sheets followed by more soil in order to eliminate leakage from the interface between the container and the soil. A square area of the ground surface was covered with plastic sheet to limit evaporation from the ground to the atmosphere. Overflow of the drum was controlled by a small hole drilled to a height of 30 cm to which a rubber pipe was connected, leading excess water far from the experiment area. On 20/7/20 the procedure started by filling the container with water and keeping the water head constant until 27/7/20 (end of wetting phase). This was followed by a period of desaturation, during which the area was kept covered by the plastic sheet for four months.

Figure 20. Wetting area protection with plastic sheets to prevent atmospheric evaporation (left) and initialization of the field wetting experiment (right).

3.2 Field Work for Ground Monitoring Station at Site 2

Exploratory drilling of borehole BH2 (Fig. 21) took place on 4/8/2019 and reached a depth of 5 meters. As in the case of BH1, successive samples of disturbed (bulk) samples were taken every 0.5 meters depth. Undisturbed samples were obtained at depths 1.2 m, 2.5 m, 4.0 m, and 4.5 m, using U100 samplers. Borehole BH2 at Site 2 soil profile is presented in the Fig 22. A 0.5 m thick layer of topsoil was recorded, overlying a 2.0 m thick layer of brownish silty-clayey marl with sandy intercalations. Underneath this layer, a yellowish marl layer of 2.0 m thickness is developed, and finally there is a high plasticity yellowish silt-clayey marl oxidated layer of 1.0 m thickness. No water table was struck during drilling.

Figure 21. Exploratory drilling at Site 2 (BH2).

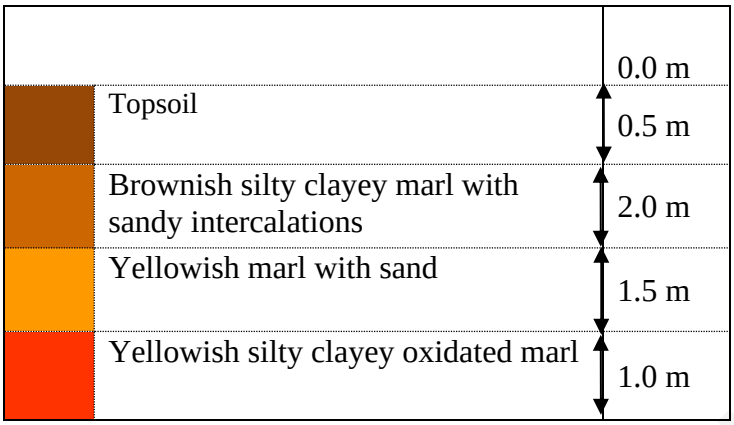

Figure 22. Stratigraphic column of BH2 at the area of Site 2 (new UCY campus).

Test pit 2 has dimension of 1 m width and 2.7 m length and is north-west of a UCY warehouse building (Fig. 23). Two pairs of Teros 21 and Teros 12 sensors were placed in test pit 1 at depths 0.6 and 0.67 m from the surface and one pair at 1.4 m depth on the side wall of the pit facing south-west. While the process of placing the sensors in this case was generally similar to that of Test pit 1, a slight modification was made to the method in order to minimize the effects of moisture migration from the backfill on the sensor measurements. More specifically, a hand drill was used to make horizontal inlets about 40 cm long on to the side wall of the test pit, in which the sensors were placed horizontally and sealed with remolded Nicosia Marl initially, followed by a 10-20 cm thick layer of non-shrinking cement mortar.

Figure 23. Area of Site 2 and test pit 2 location.

During the excavation large blocks of soil samples and undisturbed samples were collected in order to be used for the laboratory work. A side wall sealing procedure was also followed to avoid any effect of the sensors with any moving moisture due to disturbance of the soil during excavation. All six sensors' cables were connected to a Zentra datalogger and the pit was backfilled and compacted with native soil.

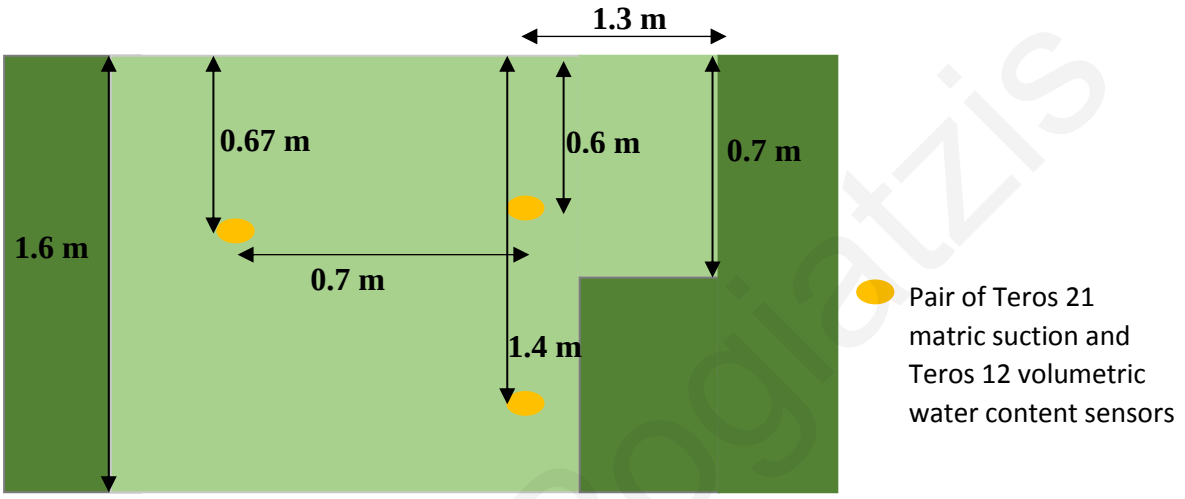

Figure 24. Schematic of the arrangement of the installed ground sensors at the side wall of excavated test pit 2.

Figure 25. Field work for the installation of sensors at Site 2.

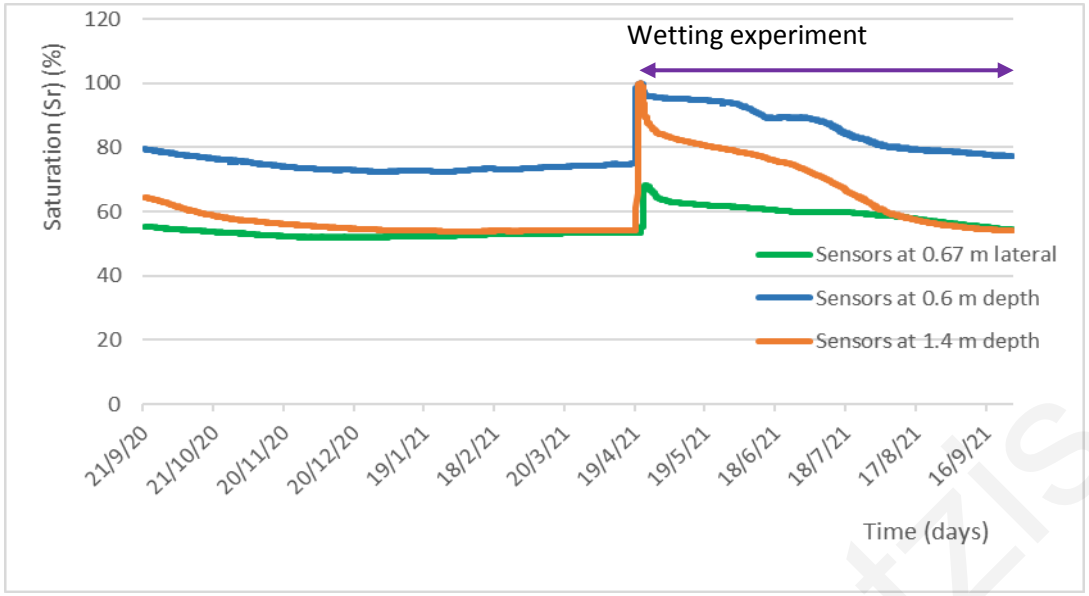

Figure 27. Degree of saturation time history inferred from field sensors recordings at Site 2 for the time period 9/2020 – 9/2021.

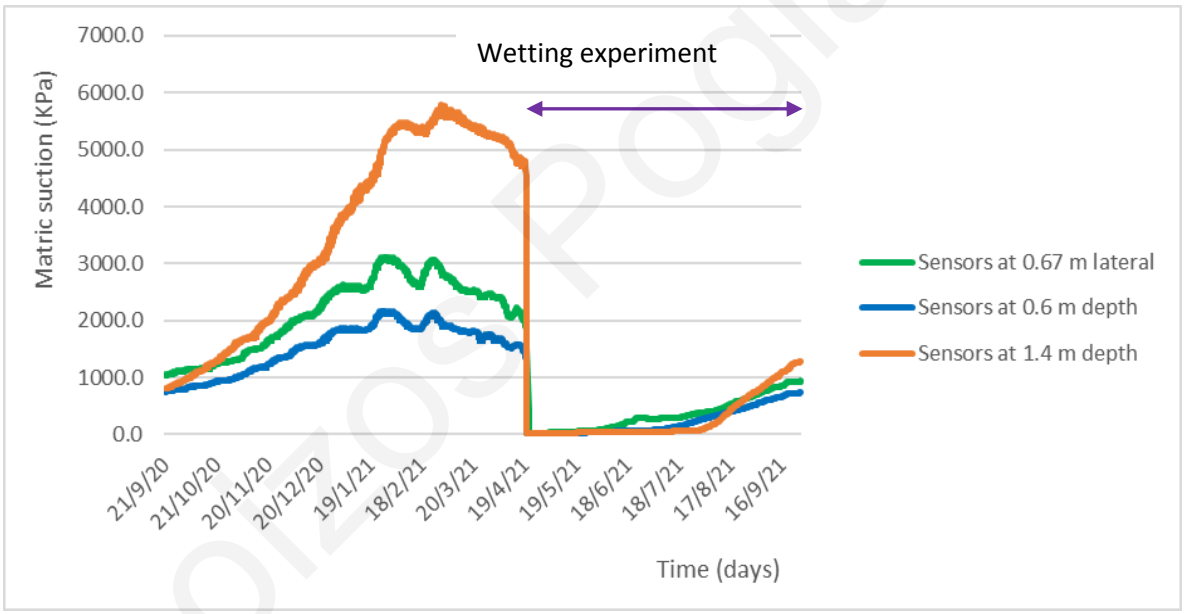

Figure 26. Matric suction time history from field sensors recordings at Site 2 for the time period 9/2020 – 9/2021.

In Figures 26, 27, all three sensors of test pit 2 showed a decreasing trend (~ of 10 %) in the values of degree of saturation a simultaneous increase of matric suction values during Fall 2020 and a slight rebound from January and on, until the start of the start of the wetting on 19/4/21. Then, the trend regained its original course until the end of the measurements.

For the field wetting experiment, the plastic drum with dimensions of 35 cm in height and 48 cm in diameter was initially firmly attached using marl putty inside an indentation 27 cm deep made on the ground surface and then then covered laterally with plastic sheets, followed by more soil in order to eliminate leakage from the interface between the container and the soil. A square area of the ground surface was covered with plastic sheet to limit evaporation from the ground to the atmosphere. On 19/4/21 the procedure started by filling the container with water and keeping the water head constant until 22/4/21 (end of wetting phase). This was followed by a period of desaturation, during which the area was kept covered by the plastic sheet for six months.

Figure 28. Initiation of field wetting experiment (left) and plastic drum with overflow (right).

3.3 Field Work for Ground Monitoring Station at Site 3

The exploratory borehole BH3 (Fig. 29) at Site 3 reached a depth of 14.5 meters. Drilling took place on 10-11/4/2019 at the area of the old University of Cyprus campus. Bulk samples were taken every 0.5 meters for the first 6 meters and then every 1 meter until the

final drilling depth of 14.5 meters. Undisturbed samples were collected using U100 samples, sealed with molten paraffin wax to prevent them from drying out. A piezometer (Fig. 29) was also installed to locate the level of possible shallow groundwater table. The soil stratigraphy column of BH 3 is show in Figure 30. The first 0.5 m consists of brownish silty-clayey marl who overlies the brownish marl of high plasticity. The grey marl was found below 13.6m. No water table was found neither during drilling nor in the long term in the piezometer.

Figure 29. Open- type piezometer installed at Site 3 in borehole 3 (left) and drilling of borehole 3 (right).

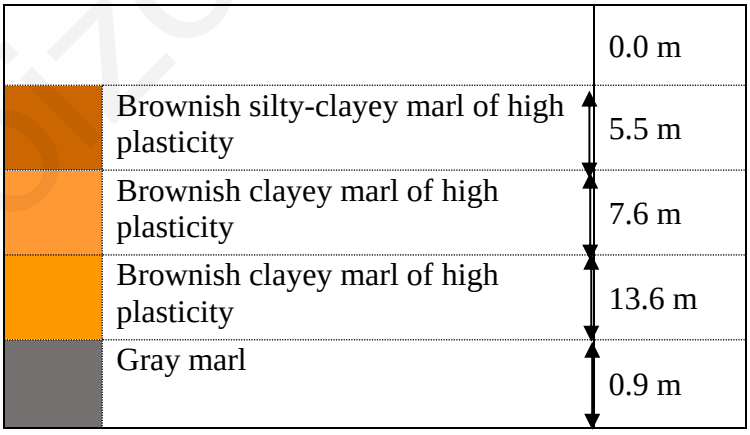

Figure 30. Stratigraphic column of BH3 at the area of Site 3 (old campus)

Figure 31. Study area of Site 3 at the old UCY campus.

At Site 3, except for drilling BH 3 and the construction of test pit 3 for the ground suction monitoring station, a pair of instrumented concrete piles was also constructed (Fig. 31, 32). The piles drilling and construction was undertaken by Themeliotechniki Ltd during 9-11 December 2019. Also, for the purposes of laboratory testing for the determination of in situ degree of saturation, bulk density, specific gravity, soil-water characteristic curve, large soil chunks both of brown khaki marl (6.5 m and 10.0m depth) and grey marl (13.5 m -14.0 m) were sampled from pile borehole cuttings and moved sealed to the Geomechanics Laboratory of UCY to avoid loss of moisture content.

Figure 32. Completed pile heads at Site 3. Location of test pit 3 is shown with an arrow.

Test pit 3 (Fig. 31-34) was excavated on 29 January 2020 southeast of the pile number 2, having dimensions 2.10 m x1.1 m. The installation of the monitoring sensors (Fig 34) followed the same procedure as the one in Site 2. Installation included three pairs of matric suction sensors (TEROS 21) and volumetric water content sensors (TEROS 12) embedded in northwest side wall of the pit (Fig. 34) inside horizontal holes 40cm long and sealed with marl putty followed by a 10-20 cm thick layer of non-shrinking cement mortar. All sensor cables were connected to a Zentra datalogger (MeterGroup Inc).

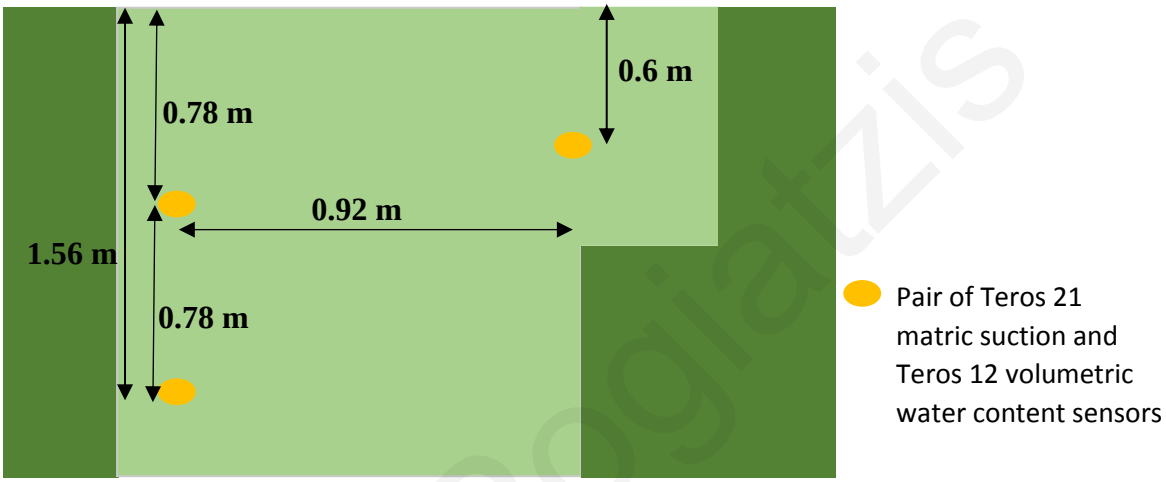

Figure 33. Front view of the excavation side wall showing arrangement of the sensors of the ground monitoring station at Site 3.

Figure 34. Installation of ground sensors in Site 3

For the wetting experiment at Site 3 (Fig. 35) the same procedure was followed as in Site 1, but this time the drum was made of stainless steel and had dimensions 23 cm in height and 32 cm in diameter, and the overflow hole was drilled to a height of 15 cm. The experiment started on 6/19/20 and continued with a steady supply until 11/19/20.

Figure 35. Wetting experiment configuration at Site 3

Figures 36-37. Shows the sensor measurements from their installation until September 2021. Initially, the same tendency was observed as in Site 1, at the sensor located at depth of 1.56 m with a sharp increase in suction due to the time required to the system to reach equilibrium in a recently disturbed soil. Then, a slight increase in matric suction was observed while volumetric water content values remained stable for about 2 months.

The experiment commenced at 27/7/20. The volumetric water content sensor at 0.78 m depth showed an increase immediately at the beginning of the experiment and stabilized below full saturation in just a few days, with the corresponding matric suction sensor showed full saturation-zero matric suction values. The moisture sensor at 1.56 m and both matric suction sensors reached full saturation in September 2020. This is probably due to the extremely low permeability of the high plasticity marl at Site 3. After the wetting phase, suction remained steady for about 5 months and saturation returned to the initial level of values. The wetting experiment was repeated on 24/6/2021, lasting until 6/11/2021 (removal of plastic covers). In the second experiment, the lower moisture sensor reached full saturation state first, 10 days after the start of the wetting, followed by the upper sensor one week later.

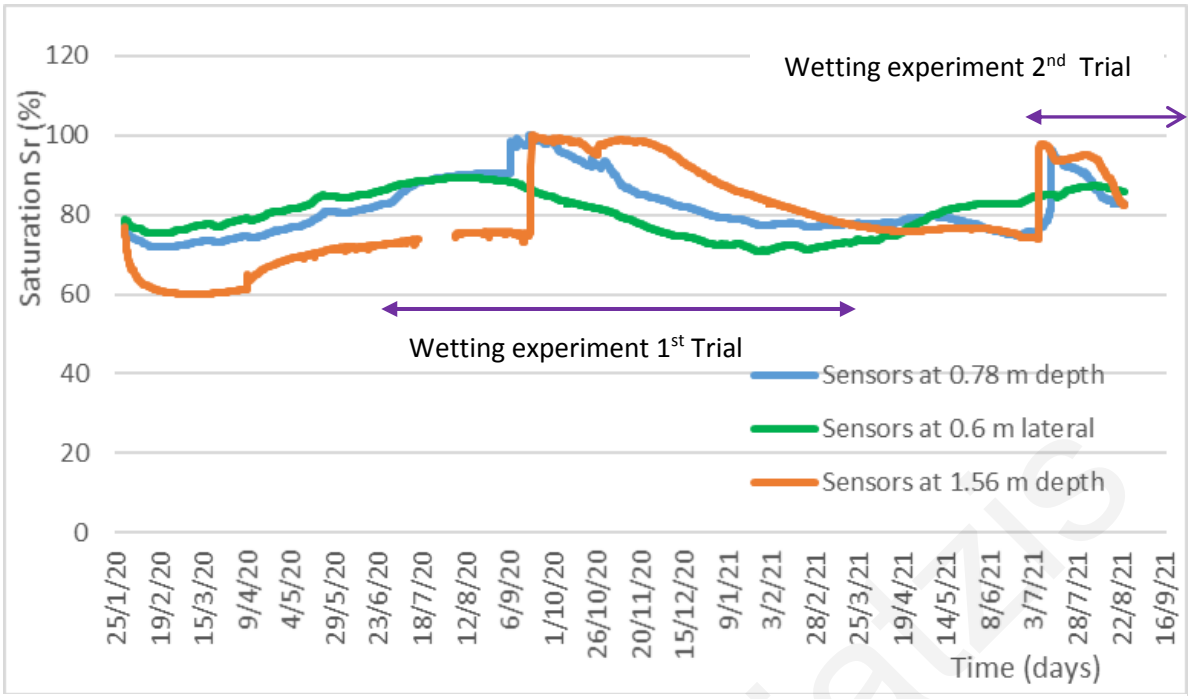

Figure 36. Field sensor recordings of saturation at the ground monitoring station (Test pit 3) and wetting experiment at Site 3.

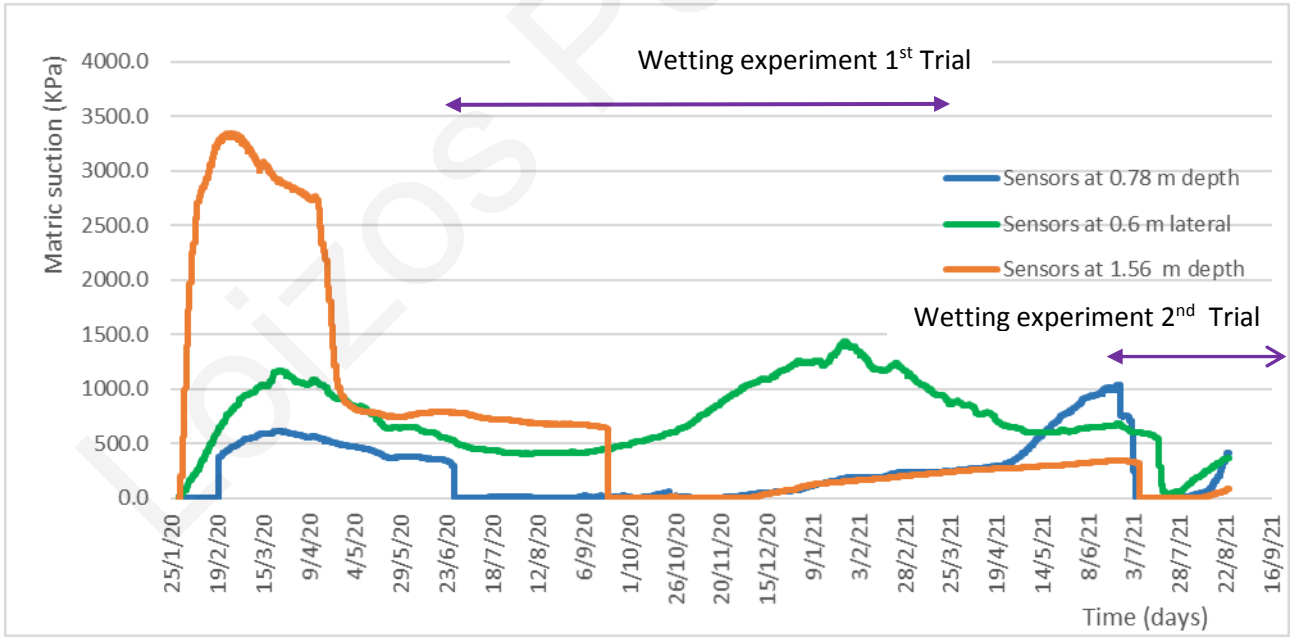

Figure 37. Field sensors recordings of matric suction at the ground monitoring station (Test pit 3) and wetting experiment at Site 3 (Loukidis et al., 2020).

4. LABORATORY TESTING

4.1 Natural (in-situ) Moisture Content and Clay Content

For the purpose of establishing the SWCC of Nicosia marl, a number of natural moisture content tests (A.S.T.M. D 2216- 98) on samples from the three boreholes (Fig.13) were performed and the results are summarized in Table 3. A total of 45 natural moisture content tests were performed on Nicosia marl samples (most of them on the brown-khaki marl and a few on the grey marl) recovered from the continuous flight auger cuttings and the undisturbed U100 samplers.

The samples were collected using U100 sampler, and more specifically, twelve undisturbed U100 samples of 0.50 m height each were collected from BH1 (depths 1.5 m, 4.0 m, 4.5 m, 5.0 m), BH2 (depths 1.2 m, 2.5 m, 4.0 m, 4.5 m) and BH3 (depths 1.0 m, 2.5 m, 4.0 m, 5.5 m) and transferred to the Geomechanics Laboratory of UCY wrapped in cling film to avoid moisture content loss. Also, some samples were paraffined for long term storage. Also, from the test pits, a number of block samples were collected and used.

Table 3. Measured in-situ moisture content

BH 1	BH 2	BH3
Up to 2.0 m: 16.6 %-23.3 %	Up to 2.0 m:23.3 %-29.9%	Up to 2.5 m:25.0 %-28.7 %
From 2.5- 4.0 m:14.0%-15.0%.	From 2.5-5.5 m:23.2 %-26.2 %	At 4.5 m: 33.4 %
After 4.5 m: 24.5%-25.5%		From 5.5 to 4.6 m:27.0 5-32.5 %

4.2 Unit Weight

For the determination of SWCC, it was also necessary to determine the marl's unit weight. Several tests were performed using the paraffin wax immersion method on brown-khaki samples. More specifically, 248 tests following the paraffin wax immersion method were performed.

In this method the samples were divided into smaller pieces weighing 10-20 grams, weighed and paraffinized, weighed again and immersed in a volumetric tube filled with water, and the volume change was recorded. By finding the volume, the unit weight was calculated and also the degree of saturation and the void ratio (e).

The results indicating that BH1 value of unit weight is between 17.2 kN/m^3 and 19.2 kN/m^3, for BH2 from 16.4 kN/m^3 to 17.44 kN/m^3 and between 17.4 kN/m^3 and 17.7 kN/m^3 for BH3.

4.3 Atterberg Limits

For the determination of the Liquid Limit (LL) the Casagrande method (A.S.T.M. D 4318-00) was used. Their Plastic Limit (PL) was also determined in order to establish the Plasticity Index (PI).

In detail a sample of about 300 g from the soil was prepared to a paste and placed on a glass plate and mixed for at least 10 min using two palette knives. If was necessary distilled water was added so that the first blow count is about 50 blows. With the cup of the apparatus resting on the base, a portion of the mixed soil placed in the cup without entrapping air. The soil surface was levelled parallel to the base and using a grooving tool the soil was divided into two equal parts by drawing the tool from the hinge towards the front in a continuous circular movement. Then the crank handle was rotated at the rate of 2 r/s so that the cup was lifted and dropped, counting the number of bumps, until the two parts of the soil came into contact at the bottom of the groove along a distance of 13 mm, measured with the end of the grooving tool or with a ruler. The number of bumps was recorded at which this occurred. Then a little more of the prepared soil from the glass plate was added and mixed with the soil in the cup, the procedure was repeated until two consecutive runs gave the same number of bumps for closure. After that about 10 g of soil was taken with a spatula from the portions of the sample that have flowed together, and the moisture content was determined. The procedure was repeated at least three more times using the same sample of soil to which further increments of distilled water have been added. Finally the moisture content of each test sample was calculated and the relationship between the moisture content and the corresponding number of bumps was plotted on a semi-logarithmic chart, with the percentage moisture contents as ordinates on the linear scale and the number of bumps as abscissae on the logarithmic scale, the best straight line fitting the

plotted points was drawn and the moisture content corresponding to the abscissa of 25 blows was marked and reported as the liquid limit.

For BH1 according to the results, liquid limit ranges between 48-93% with a plasticity index of 21-64. As such the marl falls mostly in category CH in the Casagrande chart (Fig. 38), with some samples falling into the MH category. BH2 and BH3 show results at both sides of the A-line of the chart. BH 3 ranges between 72-89 in terms liquid limit with a plasticity index value around 40.

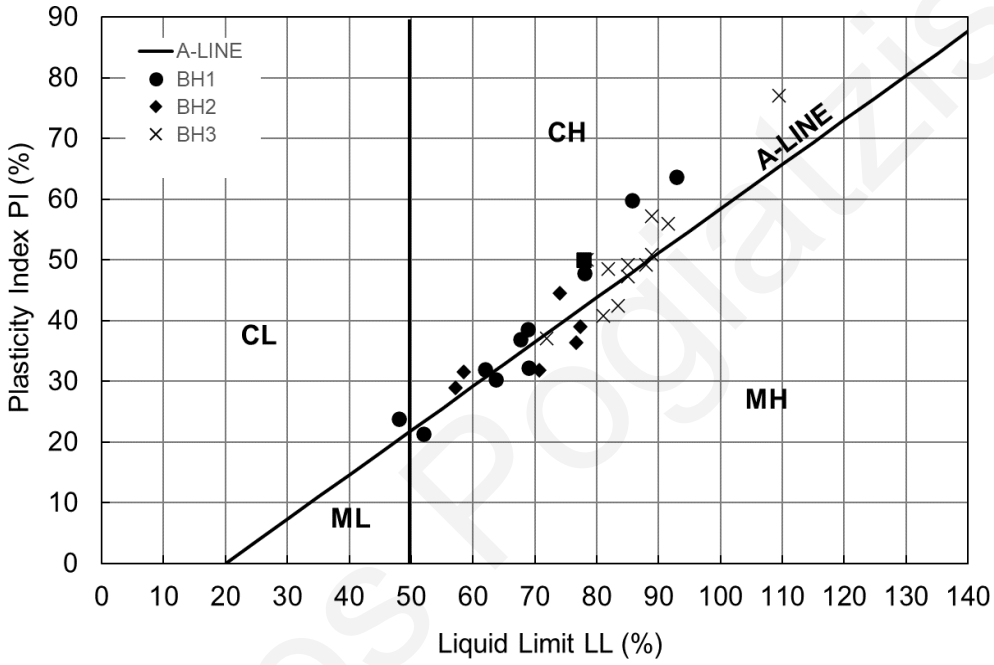

Figure 38. Characterization of the marl samples according to the Casagrande chart. (Loukidis et al., 2020)

4.4 Calcium Carbonate Content ($CaCO_3$) determination

The calcium carbonate content ($CaCO_3$) was determined using the Bernard method, i.e., through the CO_2 emitted upon reaction with diluted HCl (3N) along the lines pf the NF P94-048 standard. The results for calcium carbonate content ($CaCO_3$) determination and also the result for the clay content from particle size distribution analysis using hydrometer are shown at the tables below. It can be seen that the material in Sites 1 and 2 fit the classical definition of marl, since the calcium carbonate content is larger than 35% (35% - 47), with Site 2 being the most calcareous. On the contrary, the soil of Site 3 has a distinctively smaller $CaCO_3$ content (17%-33%), falling in the categories of calcareous clay and argillaceous marl. Moreover,

calcium carbonate content competes with the clay content, i.e., when the carbonate content is low the clay content is high.

Table 4. Calcium carbonate content (CaCO3) and clay content at BH 1

$CaCO_3$ content	*Clay content*
0-1.5 m: 35.2 %	43 %
1.5-3.0 m: 39.6 %	38 %
3.0 -5.5 m: 36.9 – 40 %	34 – 40 %

Table 5. Calcium carbonate content (CaCO3) and clay content at BH 2.

$CaCO_3$ content	*Clay content*
0.5-2.5 m: 34.8 %	32-44 %
2.5-4.0 m: 46.7 %	38 %
4.0-5.0 m: 43.1 – 46.6 %	34-40 %

Table 6. Calcium carbonate content (CaCO3) and clay content at BH 3

$CaCO_3$ content	*Clay content*
	54.0 %
0.5-6.0 m: 28.8 – 29.8 5%	43.0 – 49.0 %
6.0-13. 6 m: 16.9 – 32.5 %	43.0 – 63.0 %
13.6- 14.6 m: 22.3 %	46.0 %

4.5 Determination of Soil Water Characteristic Curves (SWCC)

For the study of the soil-water characteristic curve, the tested samples came from the 3 boreholes BH1-BH3 and from Test pit 1 excavated on 24/7/2019 (Fig. 15, 17), Test pit 2 excavated on 22/7/2020 (Fig. 23, 24, 25) in the University of Cyprus new campus (Sites 1&2)

and Test pit 3 excavated on 29/1/2020 (Fig. 33-34) in the old UCY campus (Site 3). The acquired samples, which had a size roughly in the range of 20–30 cm, were wrapped in cling film and plastic bags to prevent moisture loss during transportation.

4.5.1 Pure wetting curve

To establish the wetting curve (Fig. 40-43), one sample from each of the sites was left to air-dry down to a moisture approximately 2%. The monitoring of the course of humidity reduction was done with successive weightings. Then, the samples were divided into 12-15 parts of 80-100 grams each and water was added at different amounts to each part in order to achieve a distribution of the moisture content of the entire set within the range of 2% - 35%. After the moisture has reached the desired range of 2% -35%, the samples were wrapped in a cling film and waxed and left for 10 days to homogenize the moisture content throughout the sample. The samples were then opened, and each part was used to calculate their moisture content (BS 1377-2:1990) and total suction. Total suction was calculated using the WP4C chilled mirror hygrometer (Decagon Inc) (Fig. 39). The volume was also measured by immersion of paraffined bits in a graduated cylinder in order to be able to calculate the unit weight. Then, the moisture content and unit weight were used to calculate the saturation (S_r) and void ratio (e).

Figure 38. WP4C cold mirror hygrometer (Decagon Devices, Inc.).

4.5.2 Pure Drying Curve

For the drying part of the curve, the initial moisture content of the samples was determined, and water was added to achieve a moisture of 35%. Then the samples were wrapped in a cling film waxed and allowed for 10 days to homogenize the moisture content throughout the sample. Subsequently, the sample was opened and divided into 12-15 parts of 80-100 grams each and left to air-dray until the percentage of moisture content gradually decreases in the spectrum from 35% to 2% After desired moisture is reached through drying, the specimens were wrapped again in cling film and waxed and allowed for 10 days to homogenize the moisture content throughout the specimen before conducting further measurements. The samples were then opened for measurements of total suction, moisture content and unit weight.

4.5.3 Wetting and drying from natural moisture content

For the construction of the SWCC with initiation point the natural moisture content, initially the moisture content of the sample was calculated, and the sample was divided into 12-15 parts of 80-100 grams each. Due to the high degree of saturation of the samples at their natural state (70%-95%), most of the sub-samples were subjected to air-drying and only a few to wetting, so that a curve at the full range of moisture content from 2% to 35% can be obtained. Then the samples were wrapped in cling film waxed and allowed for 10 days to homogenize the moisture content throughout the sample. The samples were then opened for moisture content, total suction, and unit weight measurements.

4.5.4 Van Genuchten model curve fitting

The resulting clusters of datapoints were fitted by the Van Genuchten model using non-linear regression in Excel solver. The fitted curves are shown in Figures 40-43. The optimal values of the Van Genuchten parameters are:

BH1 (0.5-1.5 m) - $g_a = 0.0180$, $g_n = 1.31$, $S_{r,\,res} = 0$, $g_c = -0.237$

BH1 (4.5-5.5 m) - $g_a = 0.0048$, $g_n = 1.55$, $S_{r,\,res} = 10\%$, $g_c = -0.354$

BH2 (1.2-.7) - $g_a = 0.0075$, $g_n = 1.39$, $S_{r,\,res} = 0$, $g_c = -0.281$

BH3 (0.5-1.5 m) - $g_a = 0.0050$, $g_n = 1.39$, $S_{r,\,res} = 0$, $g_c = -0.281$

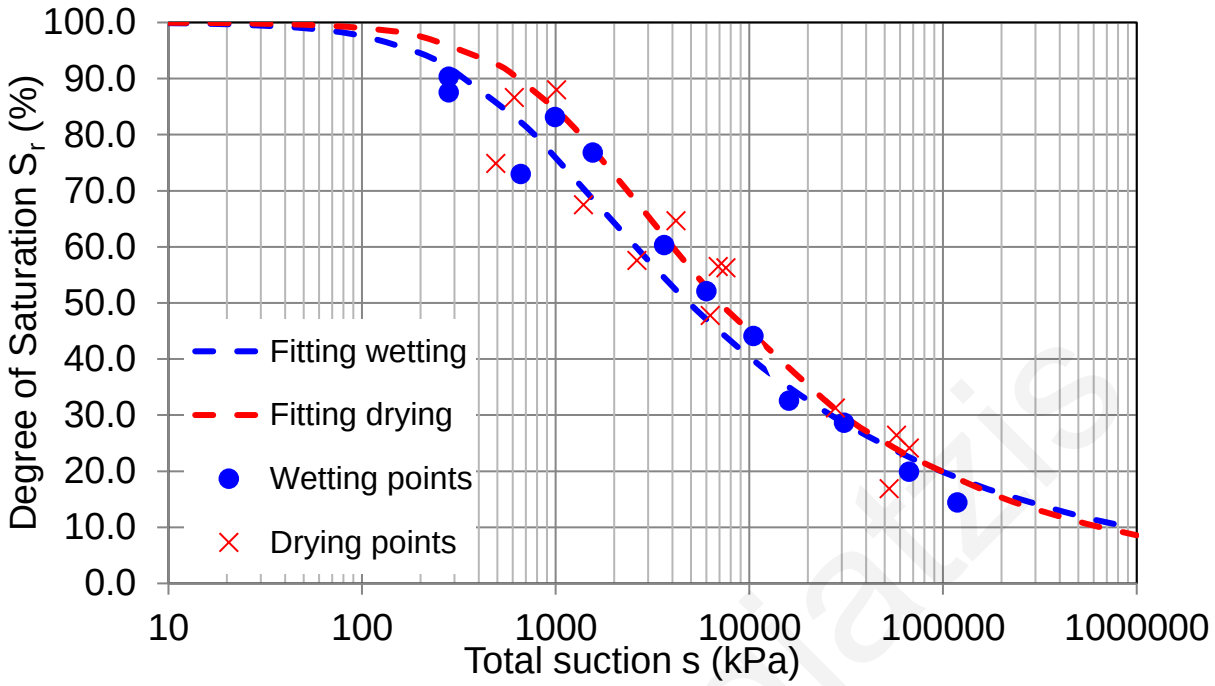

Figure 39. Drying and wetting SWCC for Site 1-Test pit 1 sample from 0.5-1.5m

The characteristic soil-water curve (SWCC) for sample from Site 1, depth 0.5-1.5m is shown in Figure 40. It seems that, when the material is 90% saturated, the corresponding total suction is equal to 330 kPa (wetting path), while for a degree of saturation ~ 20% its value rises to 100000 kPa. For the drying path it seems that when the material is 90% saturated, the corresponding total suction is equal to 620 kPa, while for a degree of saturation ~ 10 % its value rises to 60000 kPa. For this sample, the SWCC hysteresis appears to be small to moderate.

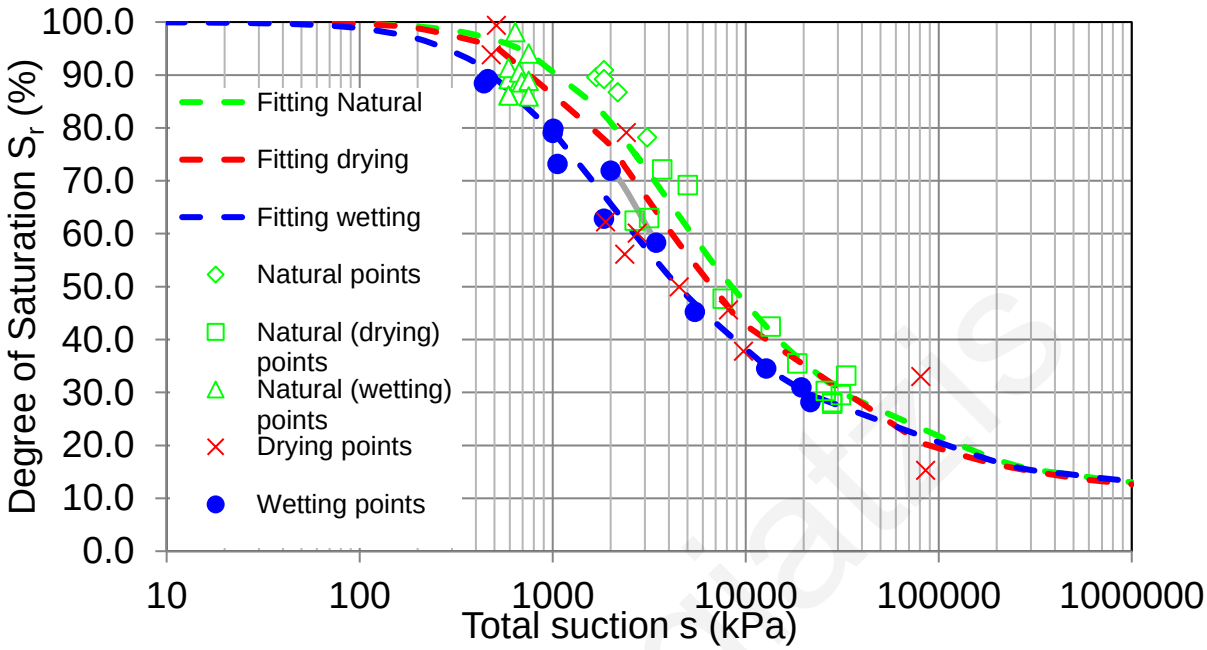

Figure 40. Drying and wetting SWCC for Site-1, borehole sample from 4.5-5.5m

The characteristic soil-water curve (SWCC) for borehole BH1 from 4.5-5.5m depth is shown in Figure 41. It seems that, when the material is 90% saturated, the corresponding total suction of the wetting curve is equal to 1000kPa and for the drying curve 1500 kPa. For a degree of saturation ~ 15%, the curves converge to 500000kPa. It is interesting to note that the SWCC from specimens with an initial state at the natural moisture content plots above the drying curve. This is probably due to the fact that the specimens that were first wetted to full saturation (at almost zero confining stress) and then dried developed intense shrinkage cracking that interfered with the accuracy of the volume measurements. Shrinkage cracking led to an overestimation of the void ratio measured using the paraffin wax immersion method, which results in the underestimation of the corresponding degrees of saturation. Thanks to the high natural water content of the samples, the green curve in Fig. 41 can be considered as a more reliable representation of the true drying curve.

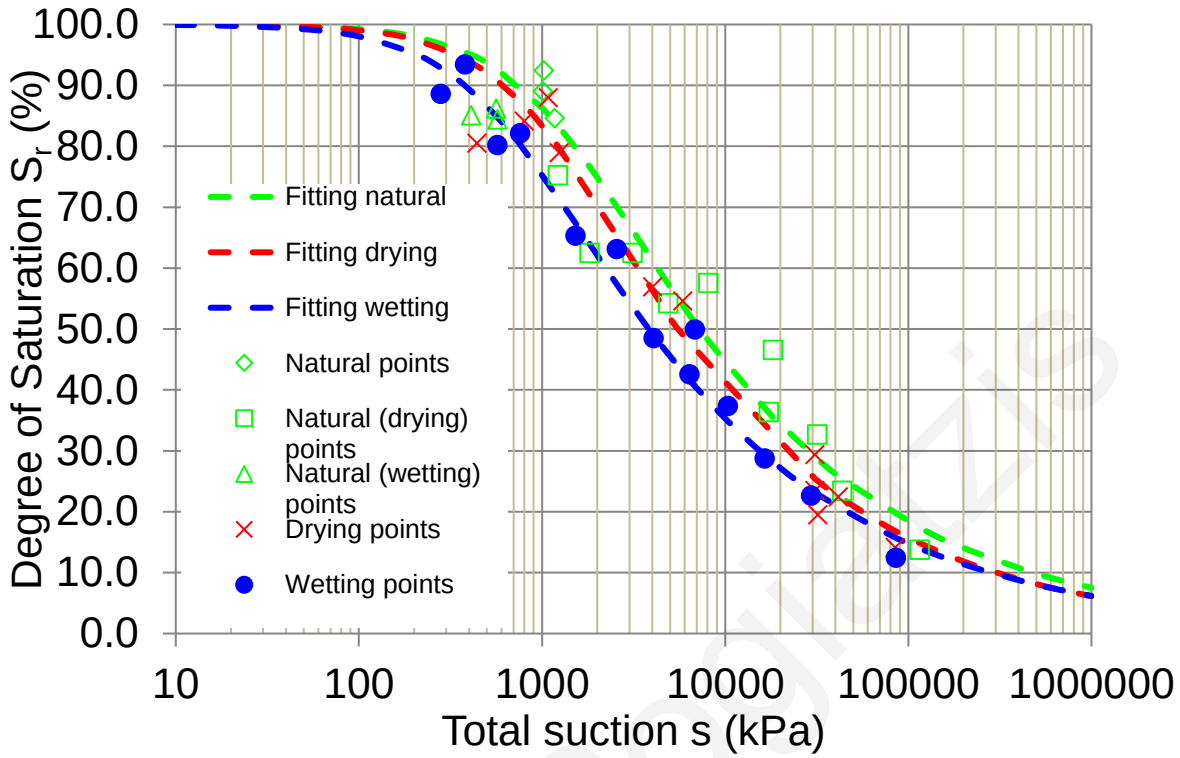

Figure 41. Drying and wetting SWCC for Site 2-Test pit 2 sample from 1.2m-1.7m

The characteristic soil-water curve (SWCC) for relatively low plasticity sample from Site 2, (Figure 42). It seems that when the material is 70% saturated, the corresponding total suction from the wetting curve is equal to 1300 kPa, while from the full drying and drying from the natural water content is 2000kPa and 2500kPa, respectively. For degree of saturation ~ 15% its value rises to 100000 kPa for both drying and wetting curves.

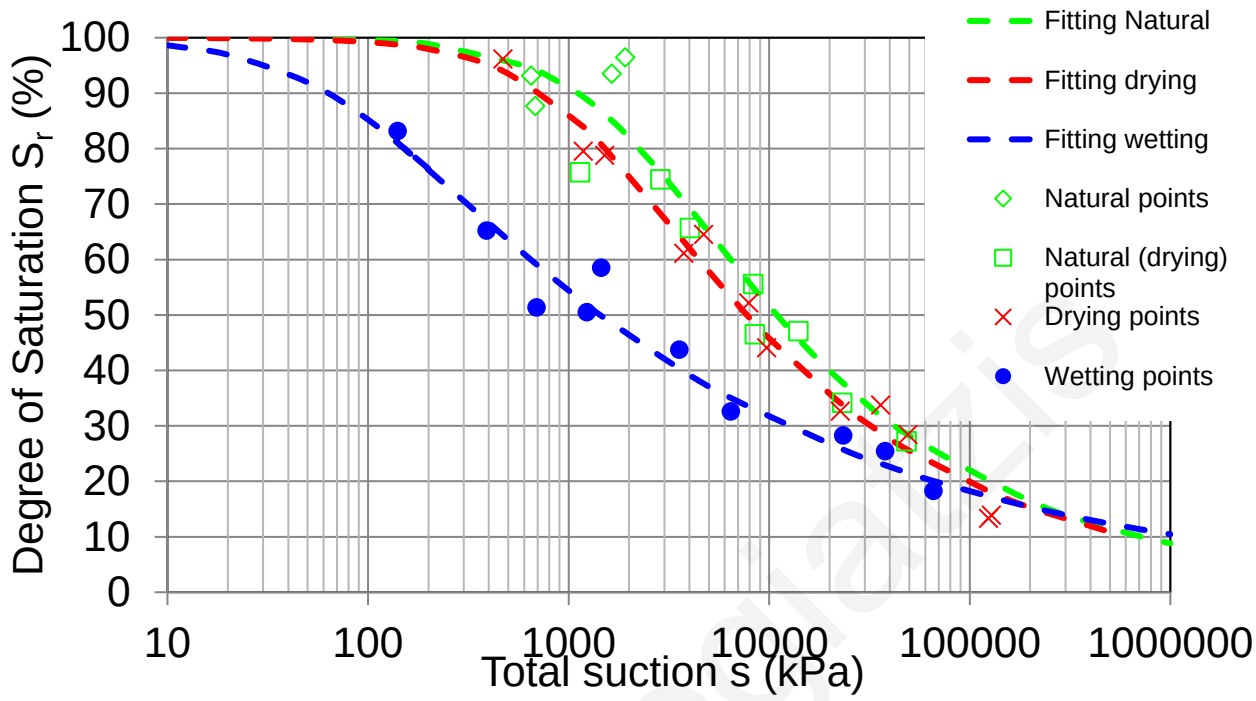

Figure 42. Drying and wetting SWCC for Site 3- Test pit 3 sample from 0.5m-1.5m

The characteristic soil-water curve (SWCC) for the high plasticity marl of Site 3 is shown in Figure 43. It seems that, when the material is 83% saturated, the corresponding total suction on the wetting curve is equal to 140 kPa, while from the full drying and drying from the natural water content is 2000kPa and 2500kPa, respectively. For the drying path it seems that when the material is 96 % saturated, the corresponding total suction is equal to 470 kPa, while for a degree of saturation ~ 14 % its value rises to 128110 kPa.

Naturally, due to the effect of hysteresis, the drying path of the curve is plotted above the wetting path with their difference to be in the order of few thousand kPa of matric suction, with the exception of the highly plastic khaki Marl of Site 3. Also, structural alteration of the marl caused by the unconfined saturation for a long period led to the paradox result of the appearance of the drying curve below the drying curve from the natural water content.

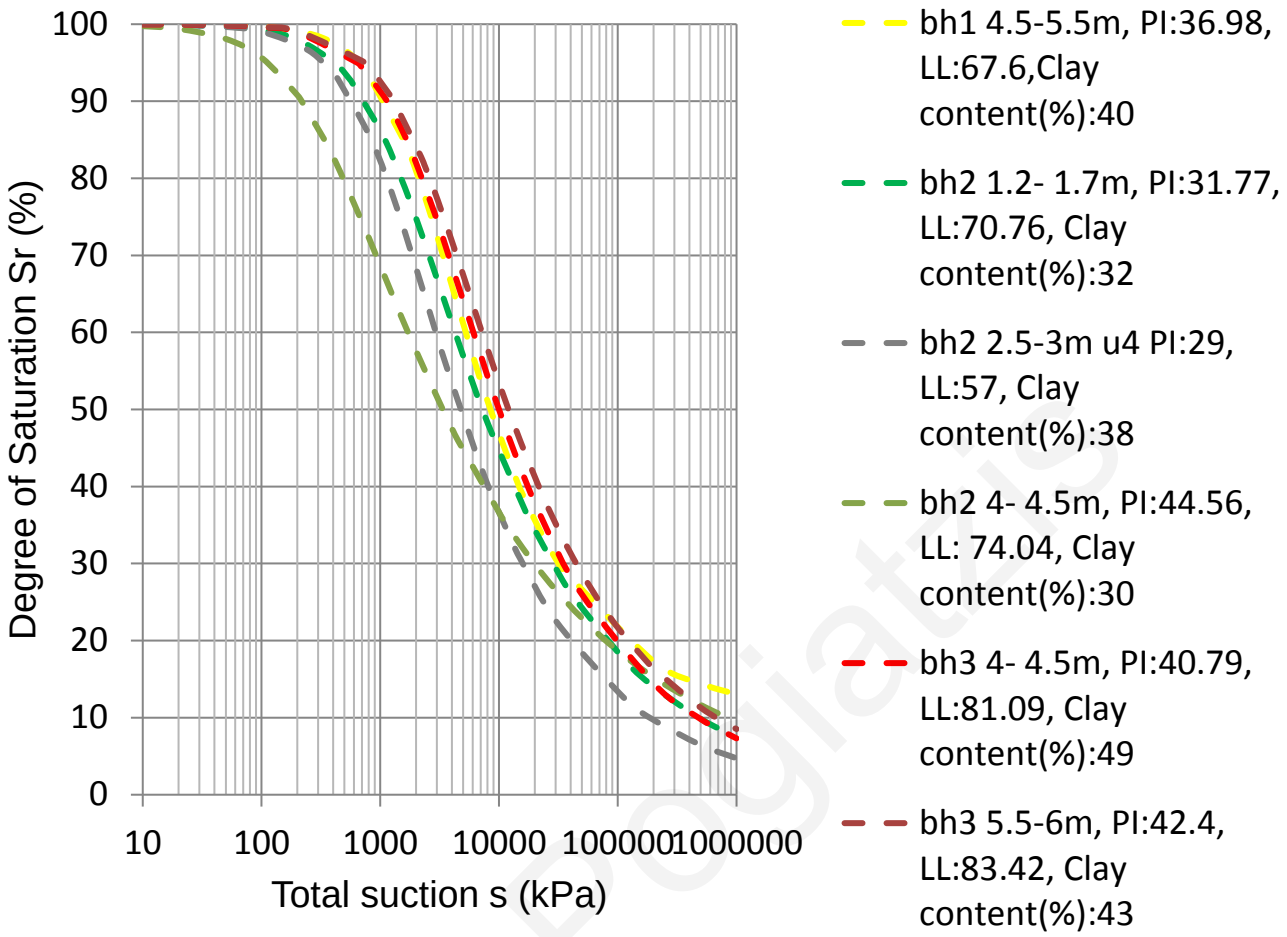

Figure 43. Fitted SWCC curves on borehole sample data for wetting/drying from natural water content (Loukidis et al., 2020).

Figure. 44 shows the fitted SWCCs from additional samples taken from boreholes BH1-BH3. The curves correspond to drying/wetting from the natural moisture state. It can be observed that the curves for the samples from Site 2, which exhibit smaller clay content and relatively lower plasticity, plot to the left of the curves from BH1 and BH3.

4.6 Filter paper measurements

The total suction measured by the WP4C chilled mirror hygrometer is the sum of two components, matric and osmotic suction. Field measurements of TEROS 21 sensors placed inside the trial pits recorded significantly lower values of matric suction than total suction

measured in the laboratory (Fig. 40-43),a fact that indicates high values of osmotic suction. This is probably due to the high concentration of cations in Nicosia marl, especially sodium cations. For this reason, an attempt was made to determine the values of osmotic suction through tests with the filter paper method on undisturbed samples according to ASTM D5298-10 (Loukidis et al., 2020).

First, the undisturbed specimens were formed into disks (the size and shape of oedometer specimens) and placed in a sealed glass container for one week to come to equilibrium with filter papers. The matric suction was determined via the contact method by placing 3 stacked filter papers between the undisturbed specimens, while the corresponding total suction was measured via the non-contact (suspension) method by placing 2 filter papers on a plastic wire screen above the specimens (Fig. 45). The difference between the two provides an estimate of the osmotic suction.

The results are shown in Table 8. It can be seen that, with the exception of the deep sample from BH1, the osmotic suction is of the order of several hundred and thousands of kPa. Moreover, it appears to be inversely proportional to the of water content. This is due to the fact that lowering the concentration of soluble salts in the pore water.

Table 7. Nicosia Marl osmotic suction results.

	BH 1		BH 2		BH3	
Depth (m)	4.5-5.5 m	0.5 m	4.0-4.5	4.0-4.5	5.5-6.0 m	5.5-6.0 m
Saturation (Sr) (%)	85-89 %		79,7	27.9	92.7 %	34.7
Moisture content		16.24-17.44	28.7			
Osmotic suction (kPa)	1-4	5180-1860	830	2040	1290	3720
Total suction (kPa)			930	28470		

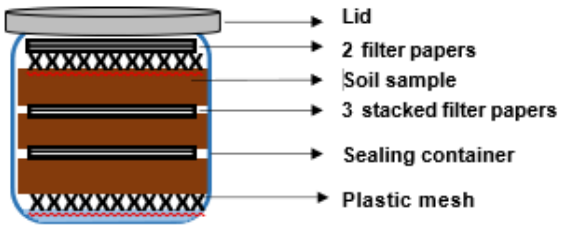

Figure 44. Schematic layout of filter paper method. (Loukidis et al., 2020)

4.7 Ground sensor measurements in the laboratory

With the transfer of the block samples to the laboratory, monitoring sensors matric suction (TEROS 21) and volumetric water content (TEROS 12) were placed in three of them to monitor matric suction (negative pore water pressure) and volumetric water content through a ZL6 datalogger and the Zentra utility software (Fig. 51) during air-drying. In more detail, in each sample, 2 inlets were carved (at a sufficient distance between them to avoid any interaction and after) where the sensors were installed. The samples were then thoroughly sealed using cling film, weighed and left for 15 days to homogenize moisture content throughout the sample volume. Then, to aid the gradual loss of moisture, holes were drilled with an electric hand drill, and the evolution of the moisture and matric suction was monitored through the aforementioned software, as well as with successive weighing for about 4 months (Fig 51).

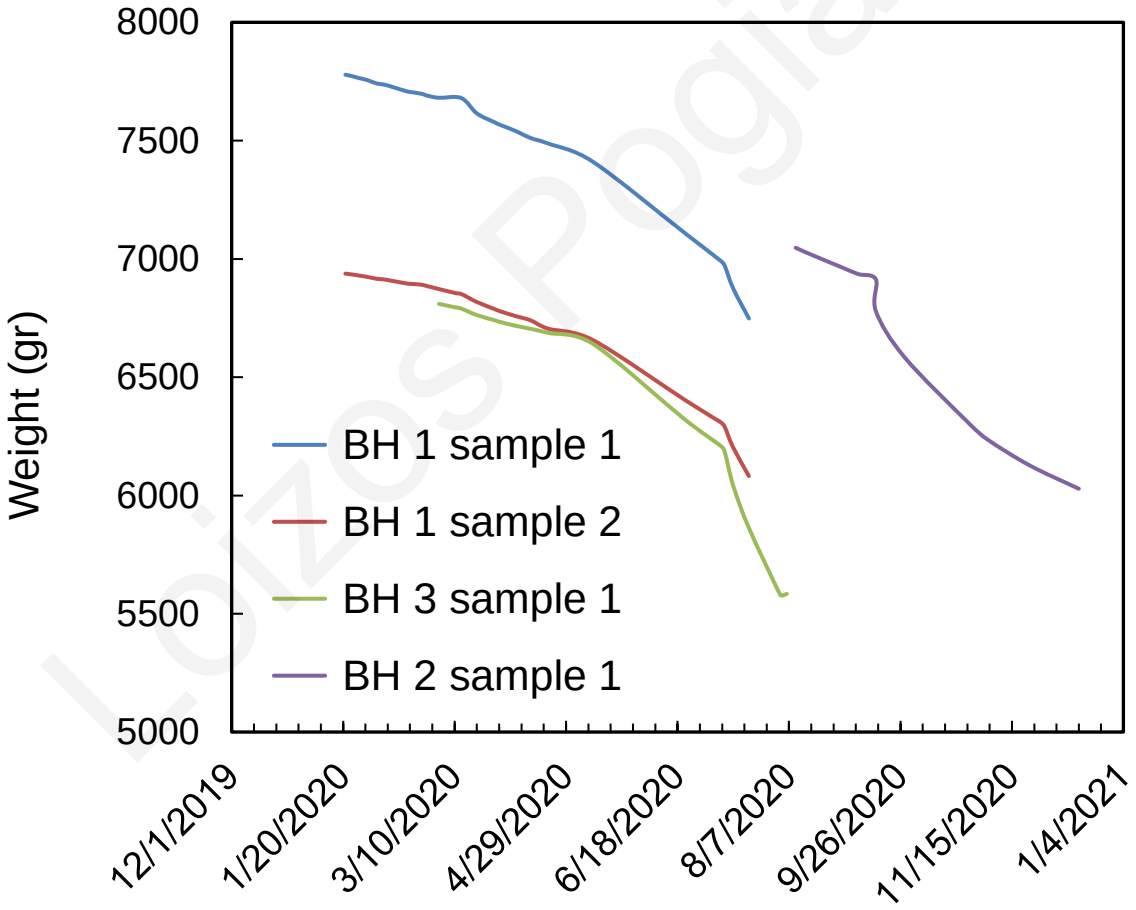

Figure 45. Progression of BH 1, BH 2, BH 3 block sample weights with time

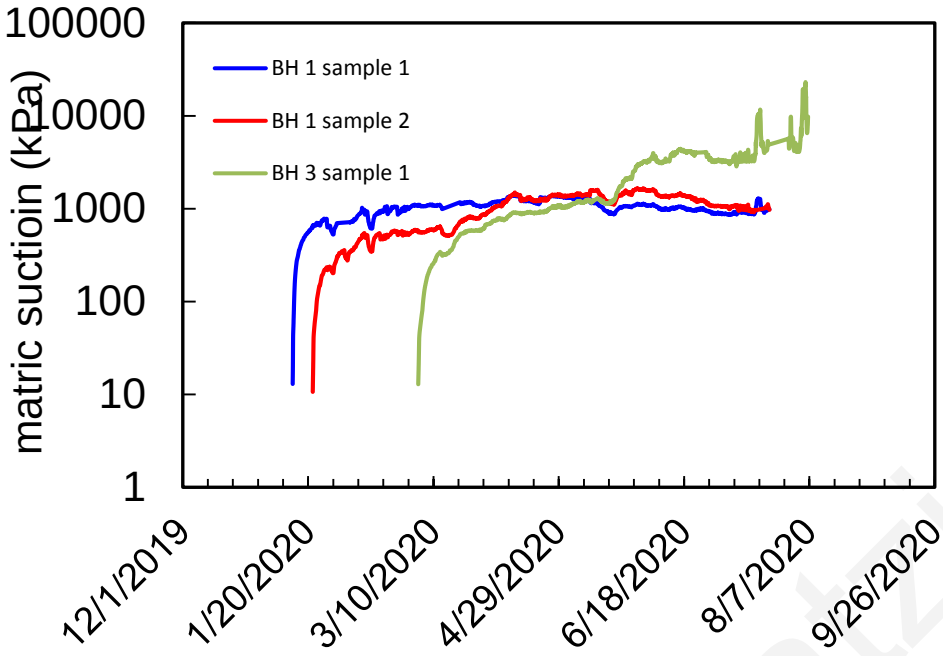

Figure 46. Matric suction recordings of BH1 and BH3 block samples during air-drying.

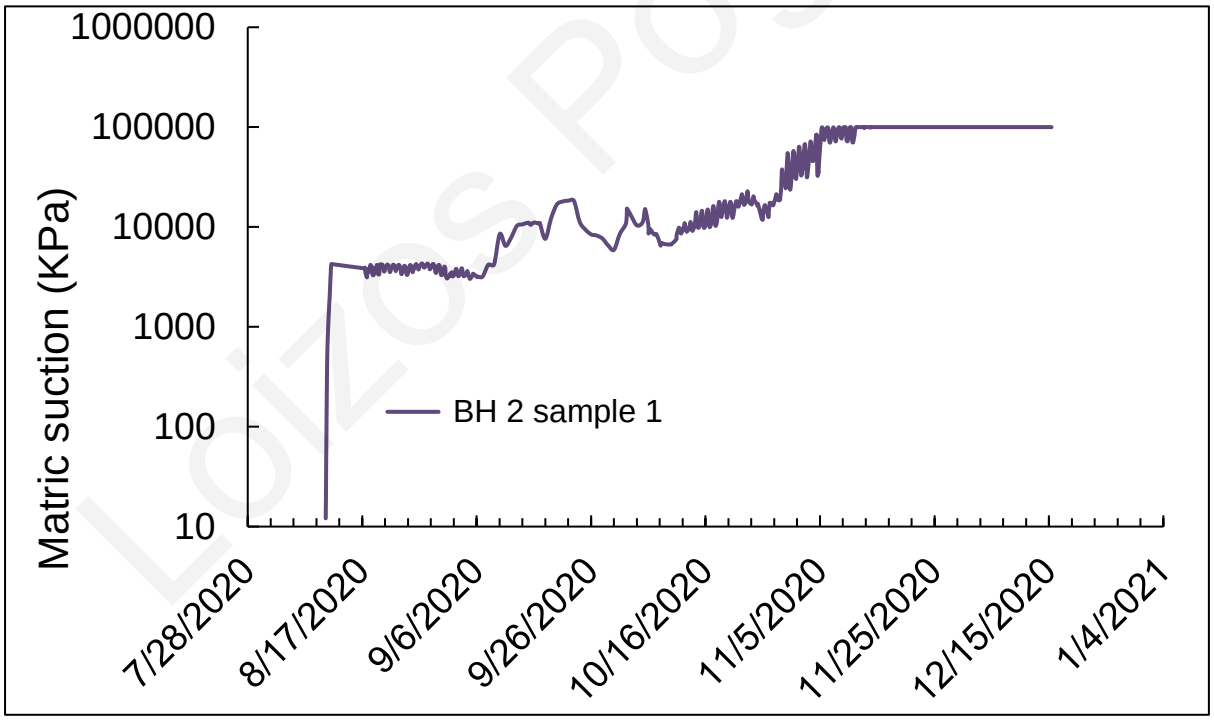

Figure 47. Matric suction recordings of BH2 block sample during air-drying.

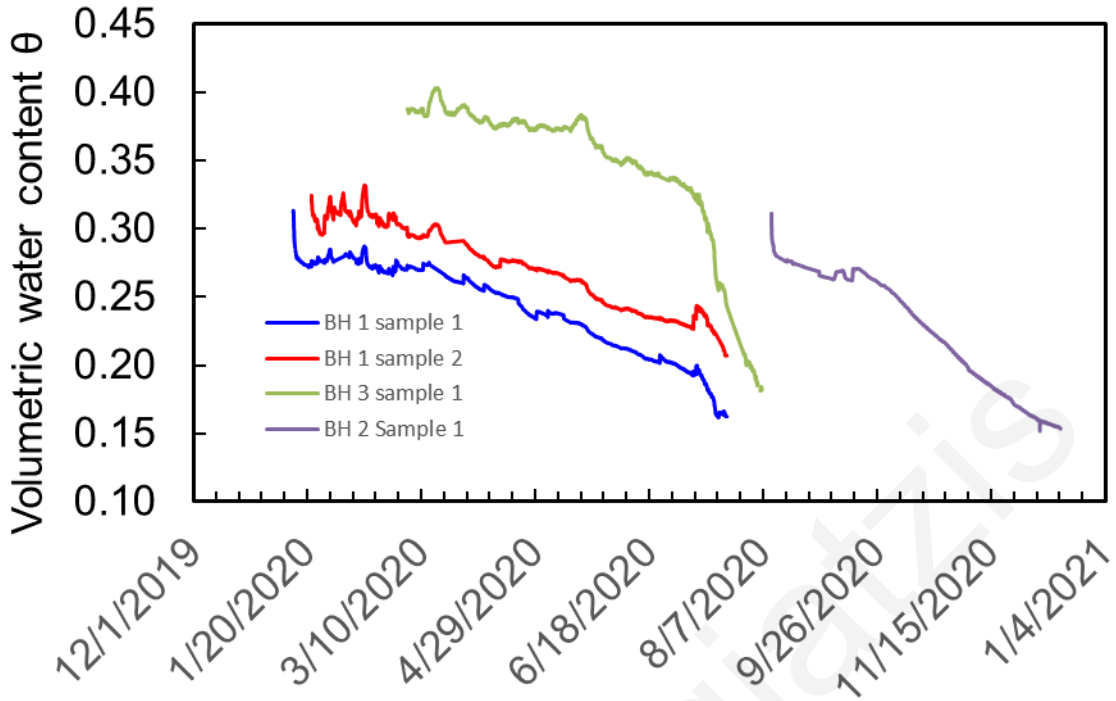

Figure 48. Volumetric water content sensor recordings during air-drying of block samples.

It can be seen that the matric suction after equilibration is of the order of a few hundreds of kPa (Fig. 47) while the total suction of the corresponding water content is around 1000kPa. These measurements also indicate the presence of significant osmotic suction, even for the relatively high initial degree of saturation.

Figure 49. Preparation of TEROS 21 matric suction sensors (placed in water for 24 hours) and TEROS 12 volumetric water content sensors prior to installation.

Figure 50. Block samples with inserted monitoring sensors of matric suction (TEROS 21) and volumetric water content (TEROS 12) and data recording through ZL6 datalogger.

5. SIMULATION OF FIELD WETTING EXPERIMENTS USING FEA

The field data from the 3 ground monitoring stations were used to evaluate the hydraulic properties of the Nicosia marl, through back-calculation analysis using the Plaxis 2D finite element program. At Site 3, the second wetting experiment that took place in June 2021 was simulated.

The dimensions of the models constructed are the following: height (depth of simulated ground profile) 8 m, 14.4 m, and 38 m and length 12 m for the areas of Site 1, Site 2 and Site 3, respectively. Given the circular geometry of the wetting pond, the models were considered 2D axisymmetric, with the axis of symmetry passing through the center wetting point. The lateral boundaries were considered closed borders (zero flow perpendicular to the border), while the lower border was left open with a constant hydraulic height (constant head boundary condition). At the location of the pond, open boundary with constant head conditions were applied was assigned during the wetting phase. During the desaturation phase, closed boundary conditions were assumed through the area of the ground surface that was covered by the plastic sheet.

The ground profile was then divided into seven different layers, 0.5 m thick for the first 5 layers and 1.0 m in the sixth layer and 4.5 m, 9.0 m, 34.5 m in the seventh layer for the three cases of Sites 1, 2 and 3 respectively (Fig. 52-54). This allowed the assignment of different parameters with depth, so as to reflect the actual conditions prevailing in the field (e.g., reduction of the hydraulic permeability with the depth due to closing of the cracks).

After defining the geometry of the soil profile and the boundary conditions, trial and error simulations were performed aiming at reproducing the evolution of saturation through time, as recorded by the sensors at 0.5m and 1.5m depth, 0.67/0.7 m and 1.4 m depth, and 0.78 m depth and 1.55 m depth for Sites 1, Site 2 and Site 3, respectively. Figs. 52-54 show the geometrical configuration of the numerical models.

This was achieved by changing the in-situ hydraulic permeability coefficient in the vertical direction under conditions of full saturation ($K_{y,\ sat}$), the ratio of the horizontal to vertical coefficient of hydraulic permeability in the field in conditions of full saturation ($K_{x,\ sat}$ / $K_{y,\ sat}$) and the dependence of the hydraulic permeability on suction, through the parameter g_l, which is the material parameter that controls the reduction of permeability k with decreasing degree of saturation S_r.

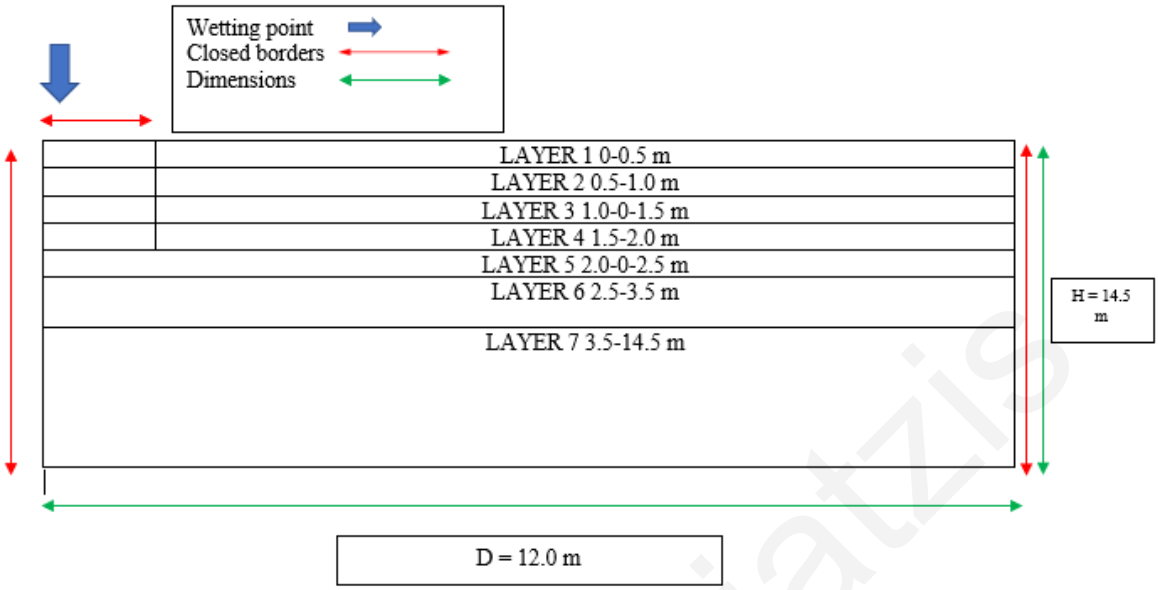

Figure 52. Model geometry and boundary conditions for simulating the wetting experiment of Site 2.

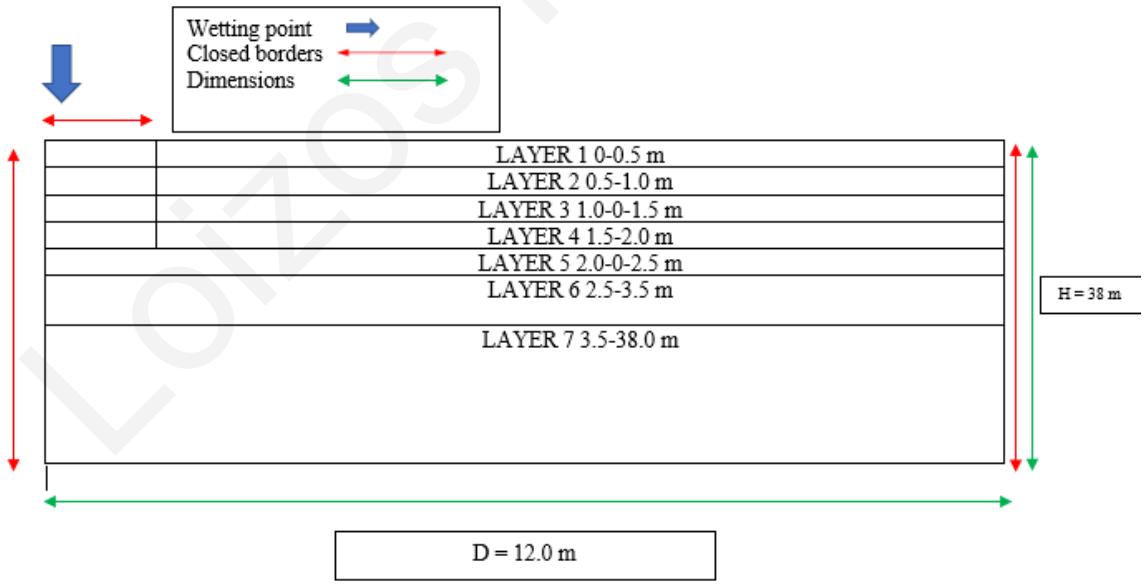

Figure 53. Model geometry and boundary conditions for simulating the wetting experiment of Site 3.

.

The values calculated experimentally SWCC were used, with only slight adjustments in certain cases, in the simulation of the wetting experiments in Plaxis (2D):

1. **BH 1**:

   g_a = 0.009 for the first 2 soil sub-layers, 0.007 for the next 3 sub-layers and 0.0048 for the last 2 sub-layers

   g_n = 1.36 for the first 2 soil sub-layers, 1.29 for the next 3 sub-layers and 1.55 for the last 2 sub-layers

   Sr, res = 0 for all sub-layers

2. **BH 2**:

   g_a = 0.0115 for the first 4 sub-layers, 0.009 for the next 2 sub-layers and 0.030 for the last sub-layer

   g_n = 1.32 for the first 4 sub-layers, 1.45 for the next 2 sub-layers and 1.29 for the last sub-layer

   $S_{r,res}$ = 0 for all sub-layers

3. **BH 3:**

   g_a = 0.0042, g_n = 1.41, $S_{r,res}$ = 0 for the entire soil profile

Before the start of the wetting phases, the initial suction and humidity conditions observed in the field, given the presence of the aquifer (6 m at Site 1, 10 m at Site 2 and 22 m at Site 3) , must be inserted into the simulation. To achieve this, the aquifer was initially set at a relatively shallow depth and then a suction value was imposed at the soil surface corresponding to the degree of saturation observed during the period before the start of the experiment. By applying this suction, moisture is removed from the soil to the atmosphere and the aquifer level is lowered. This suction was applied progressively in the course of six dummy years until steady state was reached and the aquifer level stabilized at the desired depth.

5.1 Back-Calculation Analysis

Through multiple trials, attempts were made to reproduce in Plaxis the degree of saturation time histories recorded by the installed sensors. More specifically, the trial-error process was aiming to achieve an adequate convergence between numerical results and experiment in the desaturation path following the full saturation that occurred in both sensor depths in a time of approximately 7 days from the start of the wetting experiment for Site 1, at approximately 5 days from the start of the wetting experiment for Site 2 and approximately 20 and 12 days for the lower and upper sensor respectively from the start of the wetting experiment at Site 3.

As part of research project EXPASOL at the University of Cyprus, permeability measurements calculated from undisturbed intact samples in the laboratory were used as a guide for the selection of values in the simulations, assuming that the laboratory measured permeability constitutes a lower bound to that in the field, where the presence of fissures and shrinkage cracks results create paths that facilitate percolation and drainage.

Also, it was considered that the hydraulic conditions prevailing in the lower sub-layer are isotropic, i.e., the hydraulic permeability in the horizontal direction is equal to that in the vertical direction. More specifically, $k_{y,sat} = k_{x,sat} = 1.41x10^{-7}$ cm/s for Site 1, $7.8x10^{-9}$ cm/sec for Site 2 and $6.42x10^{-9}$ cm/sec for Site 3.

5.2 Plaxis (2D) Simulation Results

5.2.1 Site 1

Figure 55 shows comparison of the best possible saturation time-history curves obtained from Plaxis FEA after several trial simulation with the time history inferred from the ground sensor measurements. The $k_{y,sat}$, $k_{x,sat}$ and g_l parameters established through the trial-and-error process are shown in Table 8. It can be seen that the equivalent permeability close to the ground surface (down to 1m depth) turns out to be 4000 times larger than the value below 3.5m depth, which corresponds to intact marl. This increased permeability, which gradually decreases with depth, is mostly due to the desiccation cracks that were evident on the ground surface prior the start of the experiment (July 2020) and secondarily on the natural fissures of the marl. It is interesting to note that Lazarou et al. (2019) found that the equivalent in-situ permeability ($k_{y,sat}=4.05\times10^{-5}$ cm/s) of medium plastic Nicosia marl down to a depth of 1.5m at a nearby site

is 150 and 400 times larger than that measured in the laboratory on intact samples from 1.5m and 6m depth, respectively.

For the topmost layers the parameter g_l, which controls the dependence of the unsaturated soil permeability on suction, is much larger than the one at depth, rendering the permeability much less sensitive to the variation of suction during wetting, suggesting that the desiccation cracks and fissures remained for most of the duration of the wetting phase.

Table 8. Equivalent ground permeability parameters established via trial-and-error simulations for Site 1.

sub-layer	$k_{y,sat}$ (m/day)	$k_{y,sat}$ (cm/s)	$k_{x,sat}$ (m/day)	$k_{x,sat}$ (cm/s)	g_l
1	0.487	5.64×10^{-4}	1.22×10^{-4}	1.41×10^{-7}	320
2	0.487	5.64×10^{-4}	1.22×10^{-4}	1.41×10^{-7}	10
3	1.22	1.41×10^{-3}	1.22×10^{-4}	1.41×10^{-7}	3
4	0.122	1.41×10^{-4}	1.22×10^{-4}	1.41×10^{-7}	3
5	0.0122	1.41×10^{-5}	1.22×10^{-4}	1.41×10^{-7}	2
6	6.09×10^{-4}	7.05×10^{-7}	1.22×10^{-4}	1.41×10^{-7}	2
7	1.22×10^{-4}	1.41×10^{-7}	1.22×10^{-4}	1.41×10^{-7}	2

The sensor at a depth of 0.5m (A) begins to record changes in humidity in time equal to 5 days, while the sensor at 1.5m depth (B) at a time equal to 7.5 days . Both sensors show full saturation upon completion of phase 12, i.e., 23 days after the start of the experiment. Regarding the drying path of the simulation immediately after the point where the full saturation of the two sensors is observed, the recording data of the wetting experiment and the results of the simulation are generally identical, particularly for the upper sensor.

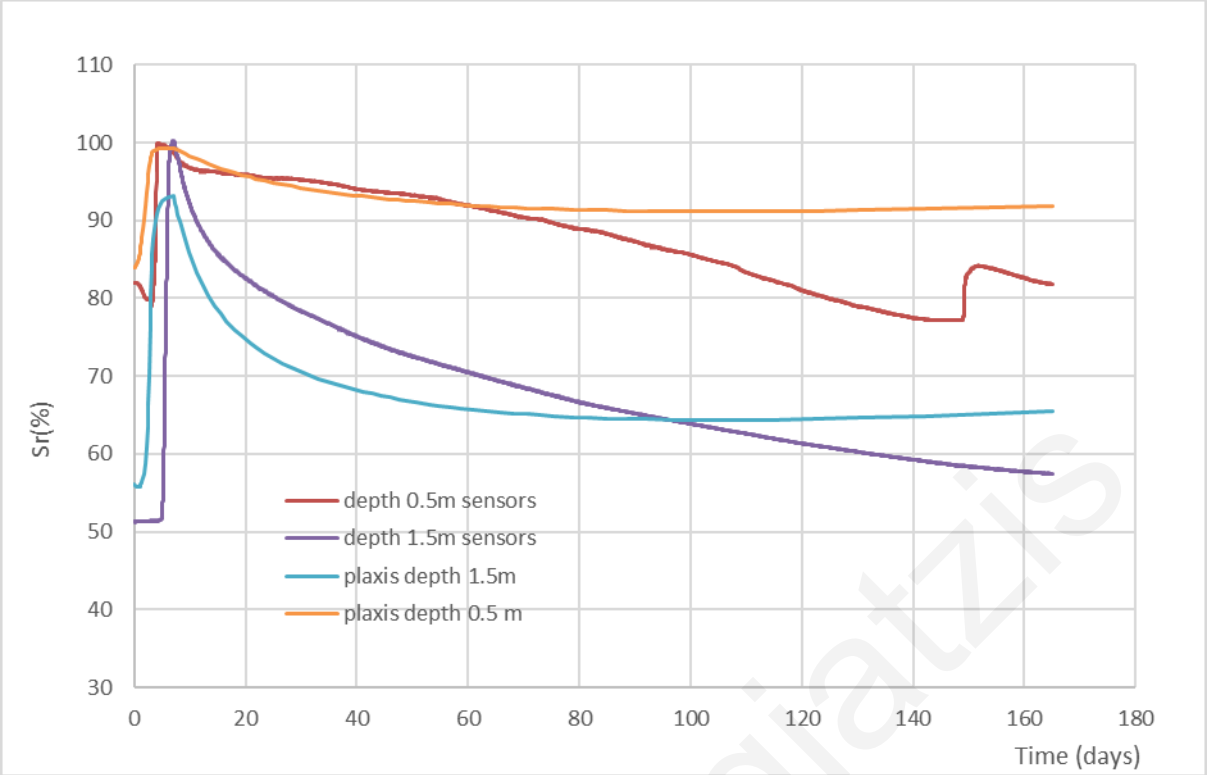

Figure 55. Plaxis simulation results of wetting experiment at Site 1 using parameters of Table 8 compared with the data of the field sensors.

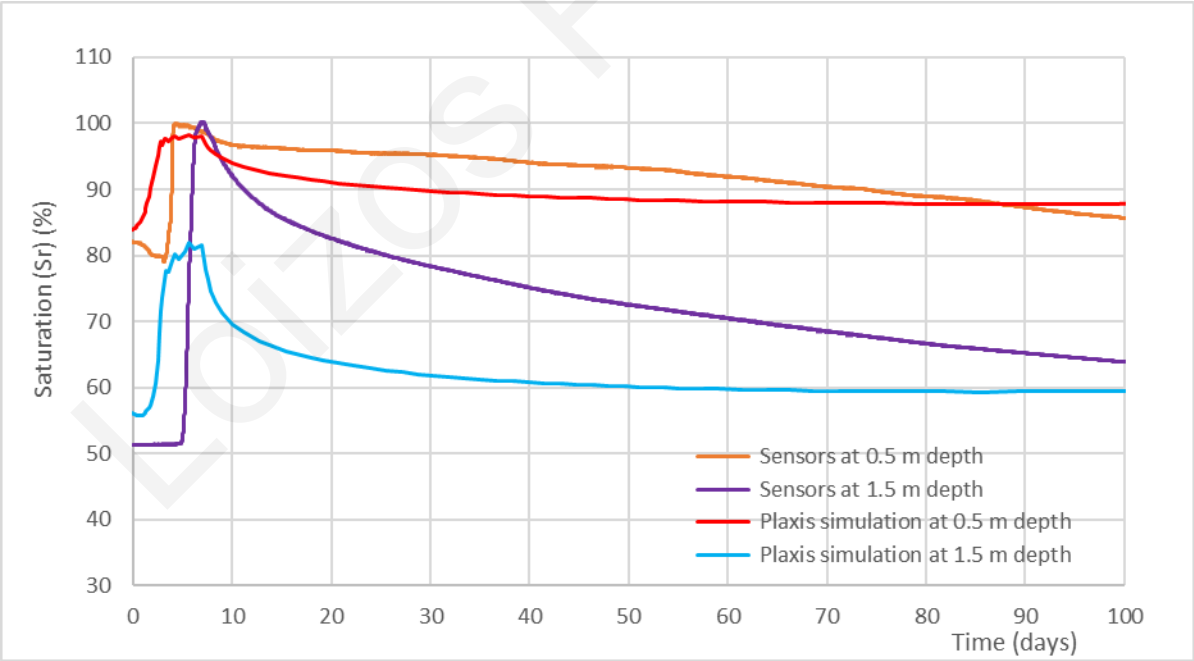

Figure 54. Plaxis simulation results of wetting experiment at Site 1 using larger horizontal permeability.

Fig. 56 shows the time-history curves if the horizontal permeability $k_{x,sat}$ is increased significantly at the 3rd, 4th, 5th and 6th sublayers (500, 200, 50 and 5, respectively) with respect to the optimal values of Table 8. In this simulation we observe the importance of the horizontal permeability, for which an increase in the value in the lower layers, below the depth of the upper sensor, results in a sharp decrease in the degree of saturation and the disagreement with the field measurements is worsened.

Figs. 57-61 show the evolution of the distribution of suction *s* in the soil profile during various stages of the finite element analysis (initial phase, first dummy year, last dummy year, end of wetting phase, end of desaturation phase). Figs. 62-66 show the corresponding distribution of degree of saturation S_r. It can be seen that in the absence of long-term evapotranspiration (initial phase), the soil is close to full saturation throughout the soil profile due to the presence of the shallow phreatic level. Prior to the start of the experiment (end of 6th dummy year), the degree of saturation in the upper layer is approximately 80% and 55-60% in the underlaying layer in which the marl is notably sandier. The wetting of the ground using a pond creates a full saturation bulb that is narrow, i.e., its lateral extend is barely larger than the radius of the pond. This can be attributed to the much smaller permeability in the horizontal direction compared to the vertical. During desaturation, moisture progressively diffuses both vertically and laterally. At the end of the simulation, the saturation profile has returned to its initial state.

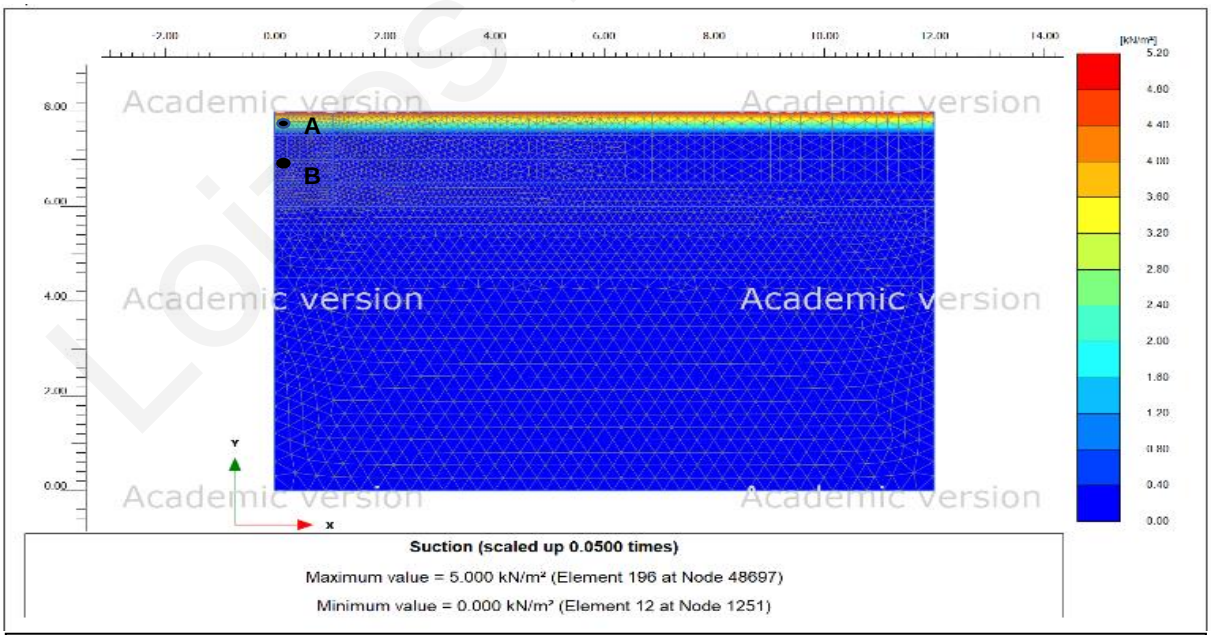

● Pair of Teros 21 matric suction and Teros 12 volumetric water content sensors at A: 0.5 m and B: 1.5 m depth.

Figure 57. Contours of soil suction at the end of the initial phase from simulation for Site 1.

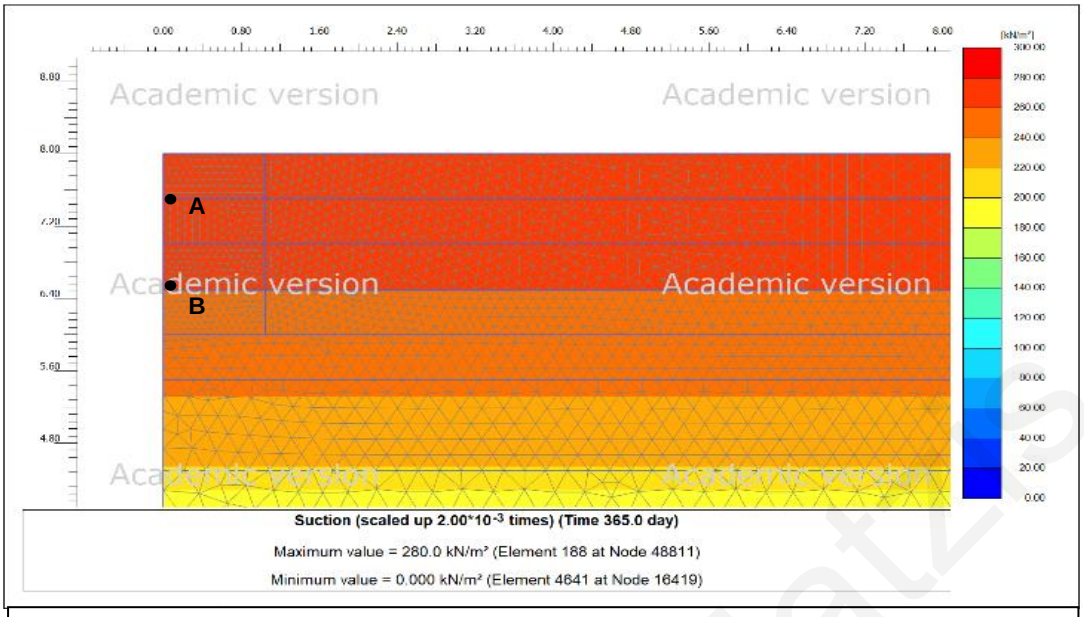

● Pair of Teros 21 matric suction and Teros 12 volumetric water content sensors at A: 0.5 m and B: 1.5 m depth.

Figure 58. Contours of soil suction at the end of 1st dummy year from simulation for Site 1.

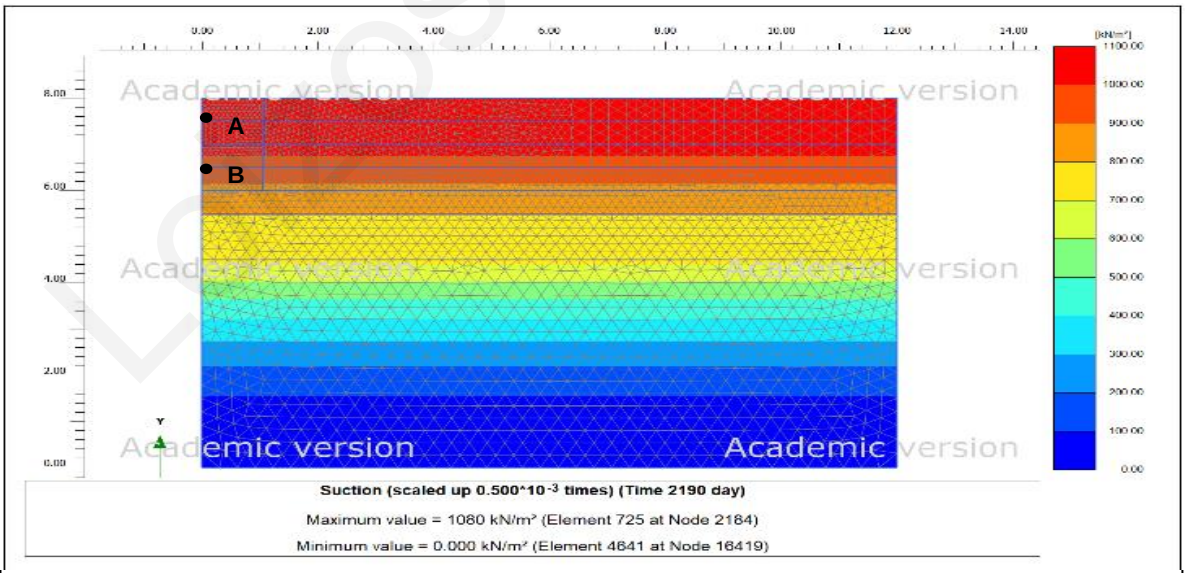

● Pair of Teros 21 matric suction and Teros 12 volumetric water content sensors at A: 0.5 m and B: 1.5 m depth.

Figure 59. Contours of soil suction at the end of the 6th (last) dummy year from simulation for Site 1.

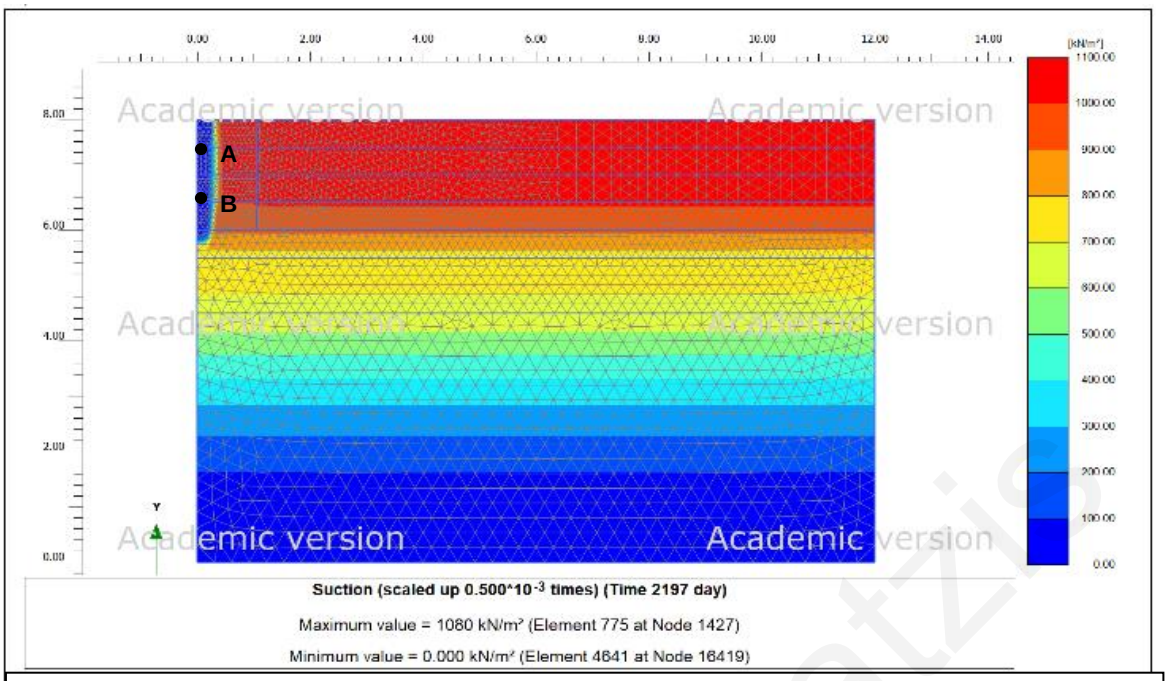

● Pair of Teros 21 matric suction and Teros 12 volumetric water content sensors at A: 0.5 m and B: 1.5 m depth.

Figure 60. Contours of soil suction at the end of the wetting phase from simulation for Site 1.

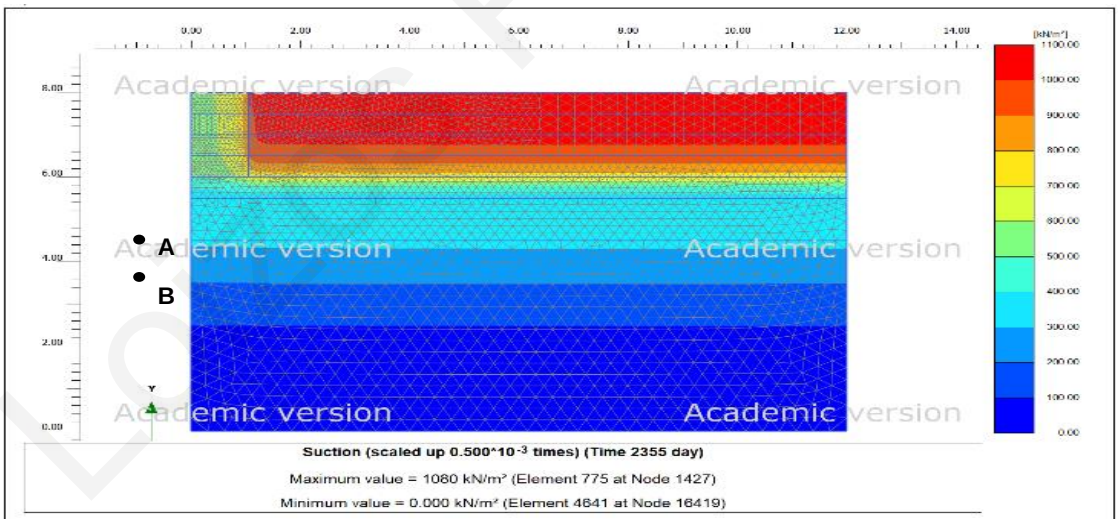

● Pair of Teros 21 matric suction and Teros 12 volumetric water content sensors at A: 0.5 m and B: 1.5 m depth.

Figure 561. Contours of soil suction at the end of the desaturation phase from simulation for Site 1.

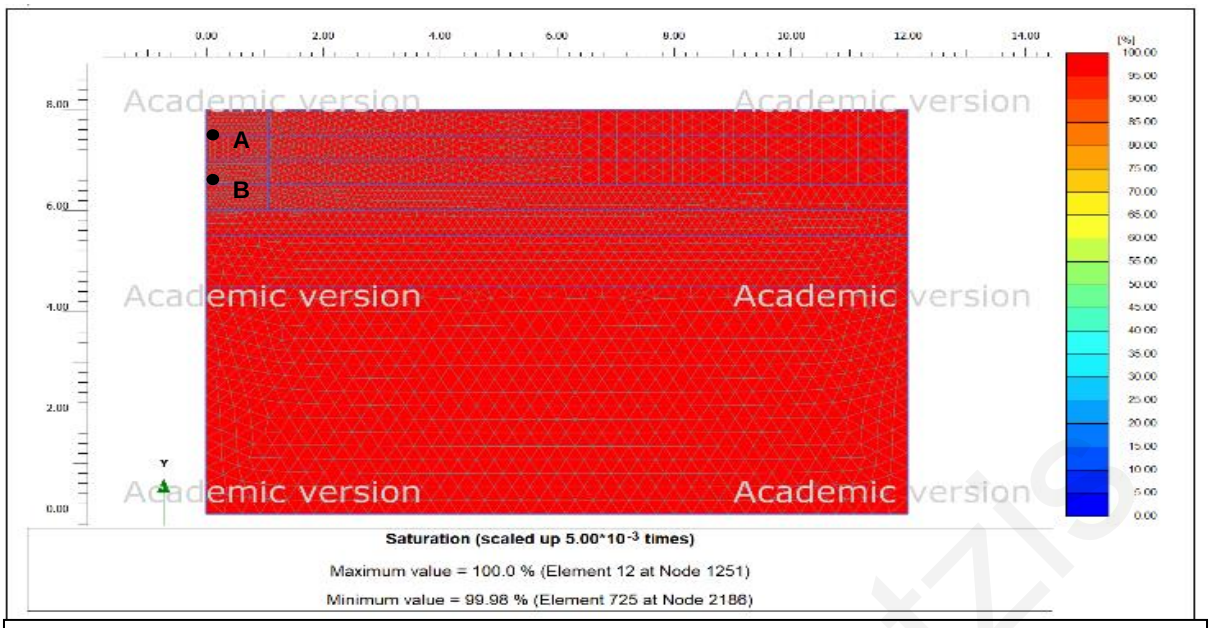

● Pair of Teros 21 matric suction and Teros 12 volumetric water content sensors at A: 0.5 m and B: 1.5 m depth.

Figure 572. Contours of degree of saturation at the end of the initial phase from simulation for Site 1.

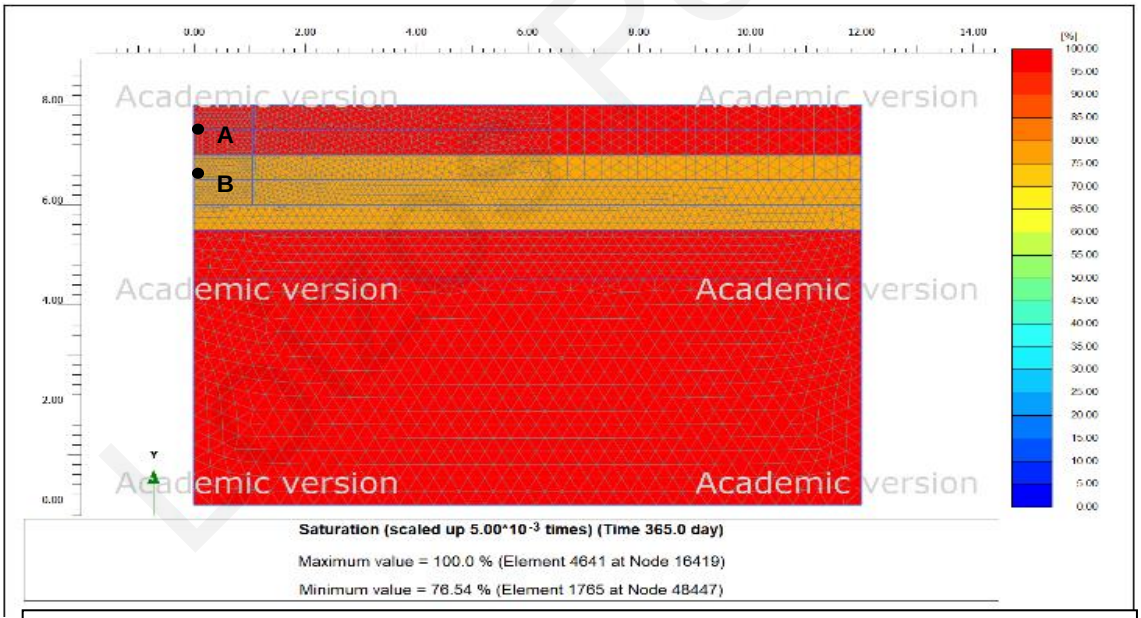

● Pair of Teros 21 matric suction and Teros 12 volumetric water content sensors at A: 0.5 m and B: 1.5 m depth.

Figure 63. Contours of degree of saturation at the end of the 1st dummy year from simulation for Site 1.

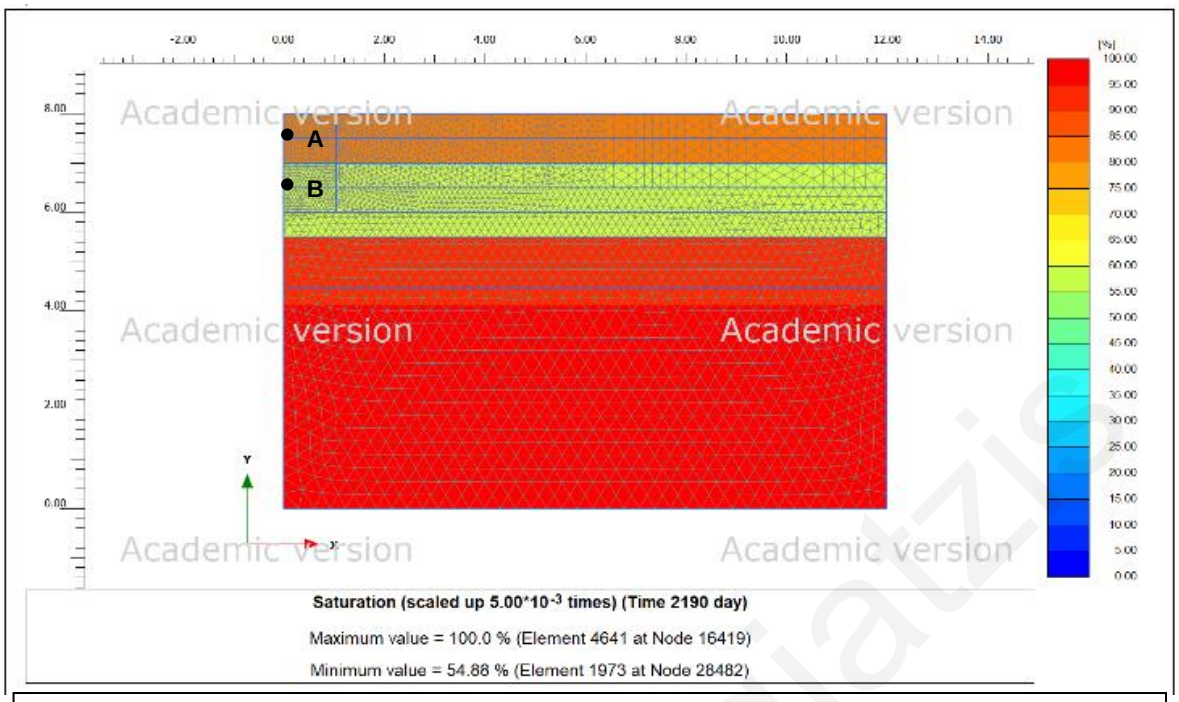

● Pair of Teros 21 matric suction and Teros 12 volumetric water content sensors at A: 0.5 m and B: 1.5 m depth.

Figure 64. Contours of degree of saturation at the end of the 6th (last) dummy year from simulation for Site 1.

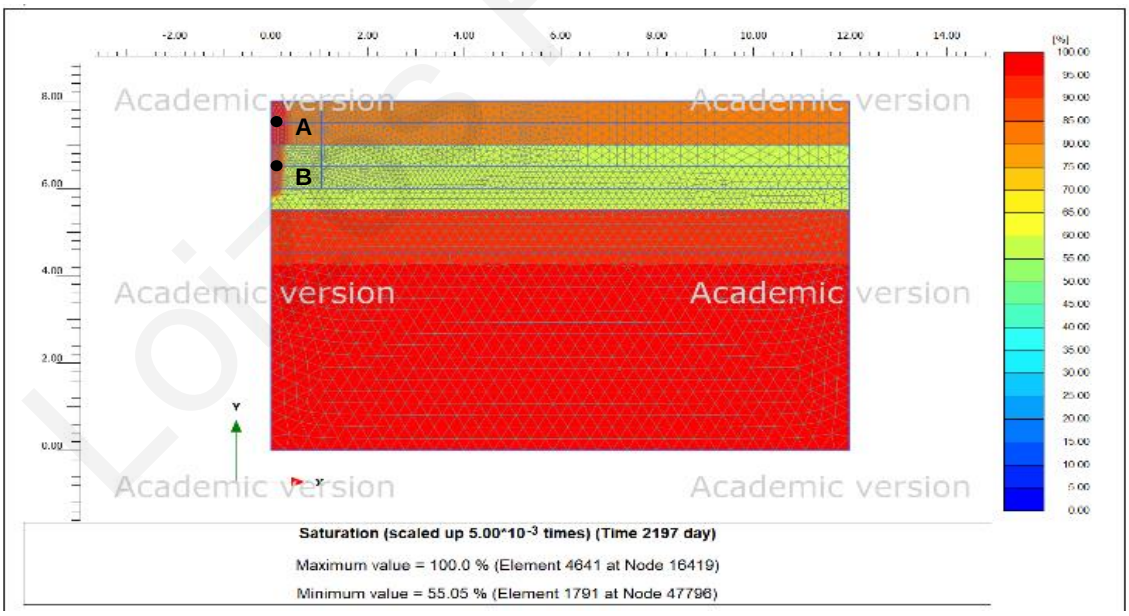

● Pair of Teros 21 matric suction and Teros 12 volumetric water content sensors at A: 0.5 m and B: 1.5 m depth.

Figure 65. Contours of degree of saturation at the end of the wetting phase from simulation for Site 1.

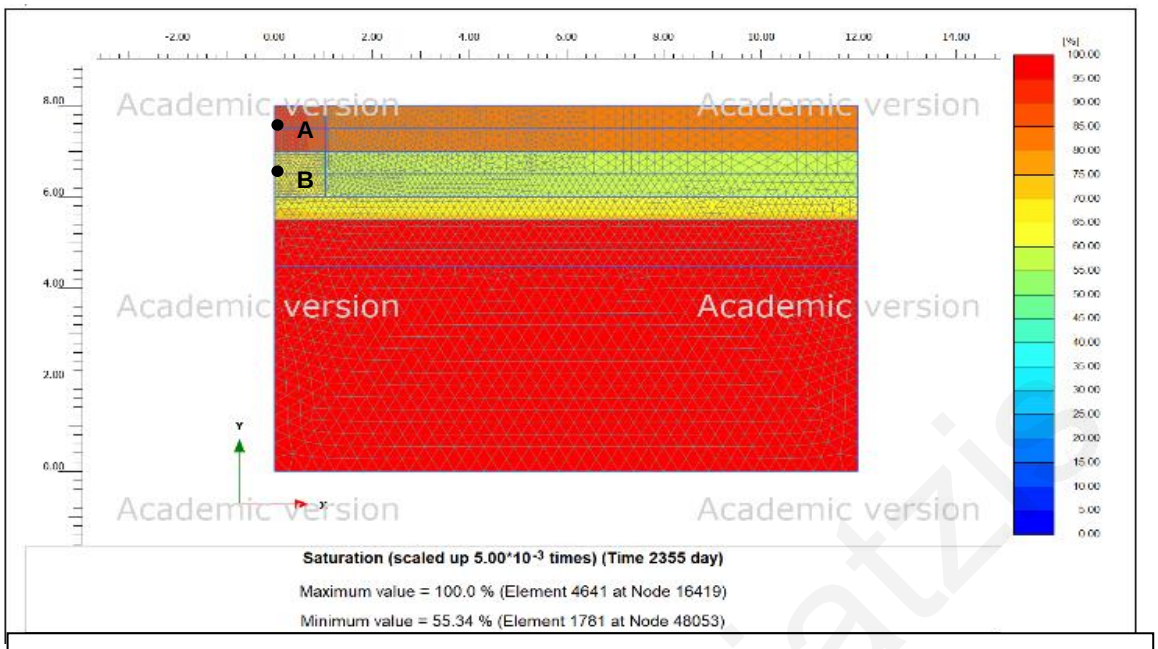

● Pair of Teros 21 matric suction and Teros 12 volumetric water content sensors at A: 0.5 m and B: 1.5 m depth.

Figure 66. Contours of degree of saturation at the end of the desaturation phase from simulation for Site 1.

5.2.2 Site 2

Fig. 67 shows comparison of the best possible saturation time-history curves obtained from Plaxis FEA after several trial simulation with the time history inferred from the ground sensor measurements. In this case the upper sensor considered is the one that lies not directly under the wetting pond, but the sensor that lies 0.7 m off center, which shows an increase is saturation during wetting without ever reaching a state of full saturation. This is because the upper sensor under the pond happens to be in very close proximity to the fill material placed behind the retaining walls of the nearby building.

The $k_{y,sat}$, $k_{x,sat}$ and g_l parameters established through the trial-and-error process are shown in Table 9. It can be seen that the equivalent permeability close to the ground surface (down to 0.5m depth) turns out to be 14000 times larger than the value below 3.5m depth, which corresponds to intact marl. In this case, the increased permeability, which gradually decreases with depth, is mostly due a dense network of open fissures, which became evident during the excavation of the trial pit, and less on desiccation cracks, given that the marl at Site 2 is more calcareous and less clayey. It is interesting to note that Barnes (2016), fissured and cracked

clays can exhibit hydraulic conductivity from k= 10^{-7} up 10^{-2} cm/sec, while when intact the k values are in the 10^{-9}-10^{-6} cm/sec, depending on the density and opening of these discontinuities.

Table 9. Equivalent ground permeability parameters established via trial-and-error simulations for Site 2.

sub-layer	$k_{y,sat}$ (m/day)	$k_{y,sat}$ (cm/s)	$k_{x,sat}$ (m/day)	$k_{x,sat}$ (cm/s)	g_l
1	0.101	1.17×10^{-4}	4.05×10^{-3}	4.68×10^{-6}	35
2	0.0675	7.81×10^{-5}	6.75×10^{-4}	7.81×10^{-7}	35
3	0.054	6.25×10^{-5}	6.7×10^{-5}	7.75×10^{-8}	7
4	6.75×10^{-3}	7.81×10^{-6}	4.5×10^{-5}	5.21×10^{-8}	3
5	2.02×10^{-3}	2.34×10^{-6}	4.3×10^{-5}	4.98×10^{-8}	3
6	6.75×10^{-4}	7.81×10^{-7}	4×10^{-5}	4.63×10^{-8}	2
7	7×10^{-6}	8.1×10^{-9}	7×10^{-6}	8.1×10^{-9}	2

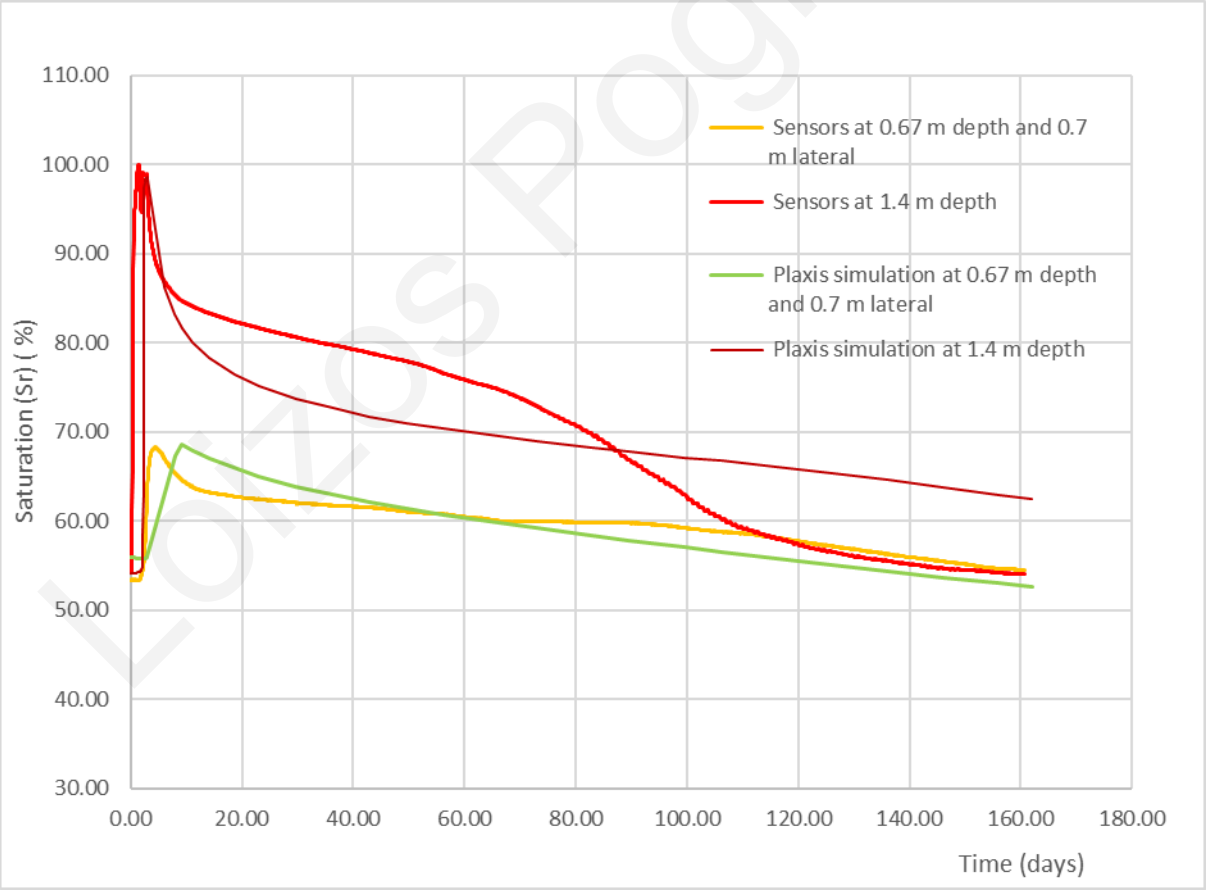

Figure 67. Plaxis simulation results of wetting experiment of Site 2 using Table 8 parameters and comparison with the data of the field sensors.

Both the sensors at a depth of 0.67 m and 0.7 m lateral (A) and the lower 1.4 m (B) show full saturation at the end of phase 12, i.e., 2-3 days after the start of the experiment. Also, in the simulation in this case, precipitation phases were inserted during precipitation at 21st of April. Regarding the drying path of the simulation immediately after the point where the full saturation of the two sensors is observed, the recording data of the wetting experiment and the results of the simulation are close, particularly for the upper sensor at the desaturation part of the simulation and for the lower sensor at the saturation part.

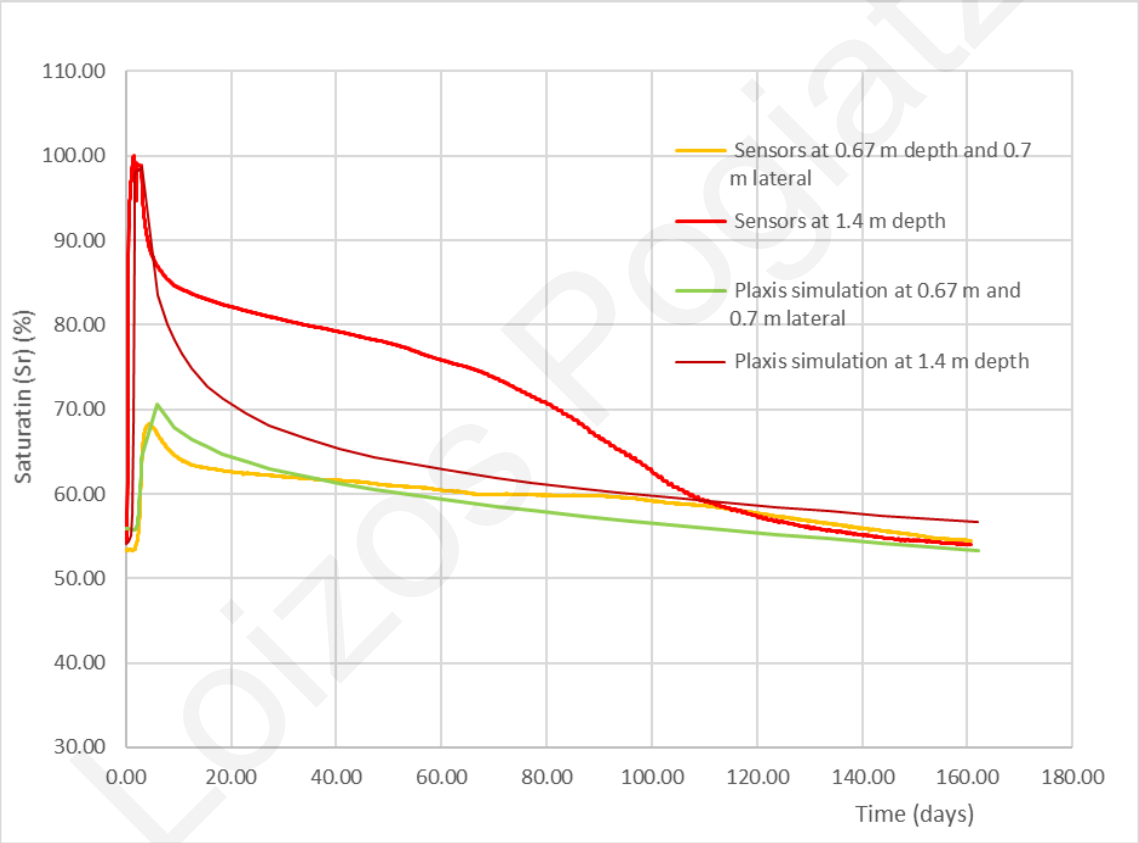

Figure 588. Plaxis simulation results of wetting experiment of Site 2 using smaller g_l value in the upper layers.

In Fig. 68, we observe that by decreasing the parameter g_l to 3 in the first 3 layers we have a much sharper drop in the degree of saturation in the upper sensor, enlarging the disagreement between the simulation results and the recorded data.

Figs. 69-74 show the evolution of the distribution of suction *s* in the soil profile during various stages of the finite element analysis (initial phase, first dummy year, last dummy year, winter precipitation, end of wetting phase , end of desaturation phase), while Figs. 75-81 show the corresponding distribution of degree of saturation S_r. It can be seen that in the in-situ suction values at the uppermost part of the profile are very high (of the order of 10MPa) and winter precipitation (prior to the wetting phase in April 2021) results in a reduction of suction in the superficial layers. As in the case of Site 1, ground wetting using a pond creates a full saturation bulb that is narrow. However, in the case of Site 2, due to the intense fissuring, which is exhibited in both vertical and horizontal directions, the lateral of the bulb is comparatively larger than in the Site 1 simulation.

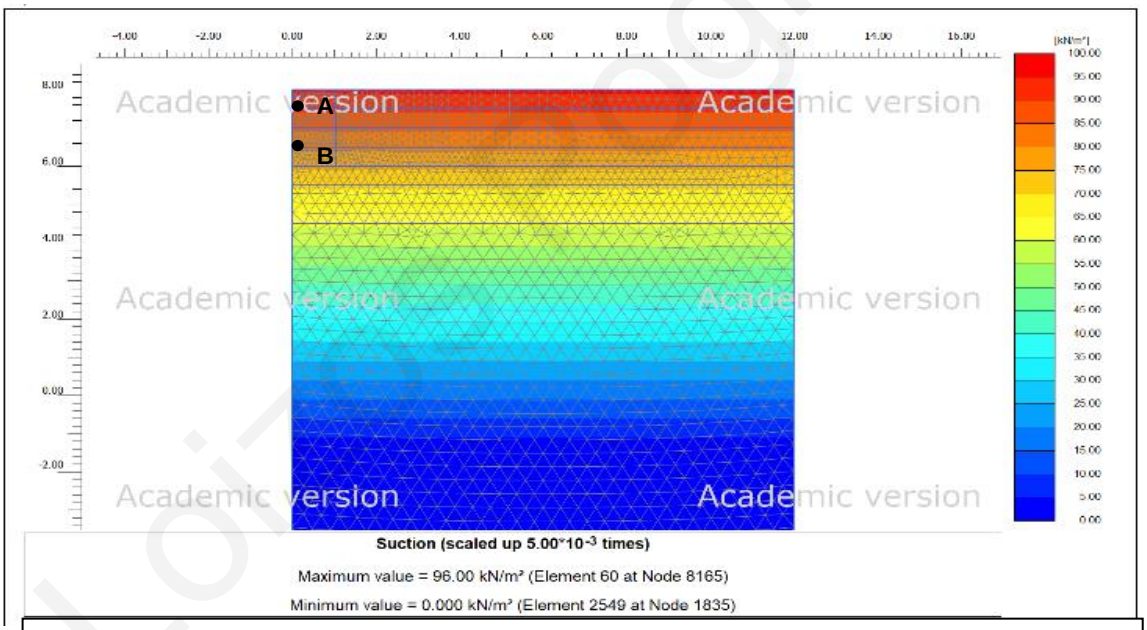

● Pair of Teros 21 matric suction and Teros 12 volumetric water content sensors at A: 0.67 m depth and side distance 0.7 m and B: 1.4 m depth.

Figure 69. Contours of soil suction at the end of the initial phase from simulation for Site 2.

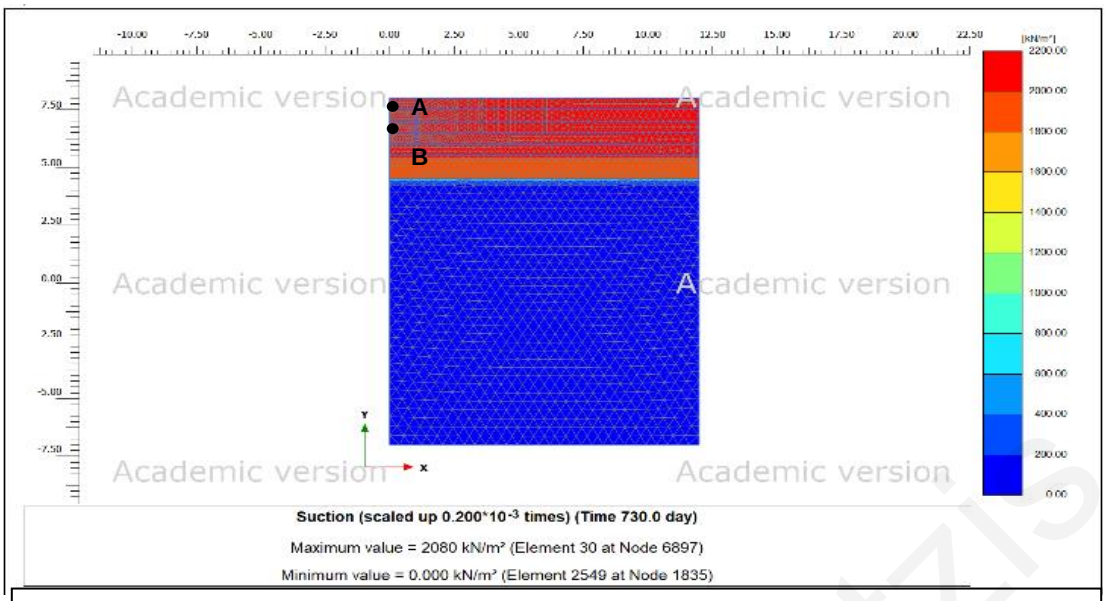

● Pair of Teros 21 matric suction and Teros 12 volumetric water content sensors at A: 0.67 m depth and side distance 0.7 m and B: 1.4 m depth.

Figure 70. Contours of soil suction at the end of the initial phase from simulation for Site 2

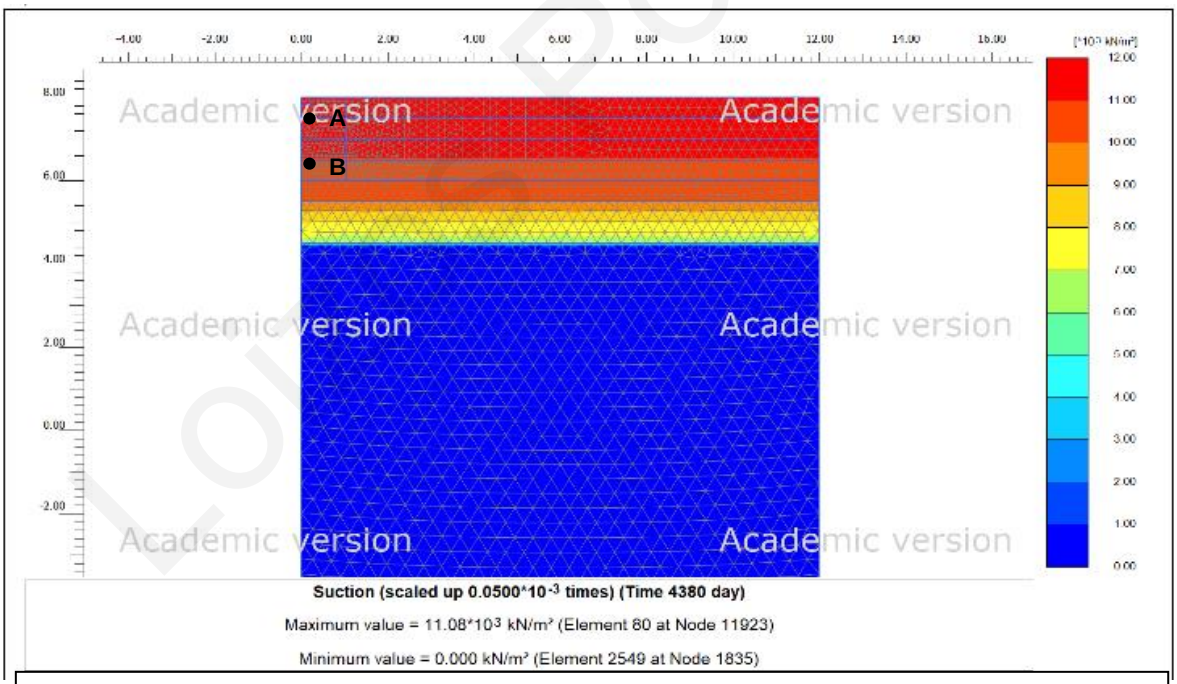

● Pair of Teros 21 matric suction and Teros 12 volumetric water content sensors at A: 0.67 m depth and side distance 0.7 m and B: 1.4 m depth.

Figure 71. Contours of maximum value of suction during precipitation at 21/4 from simulation for Site 2.

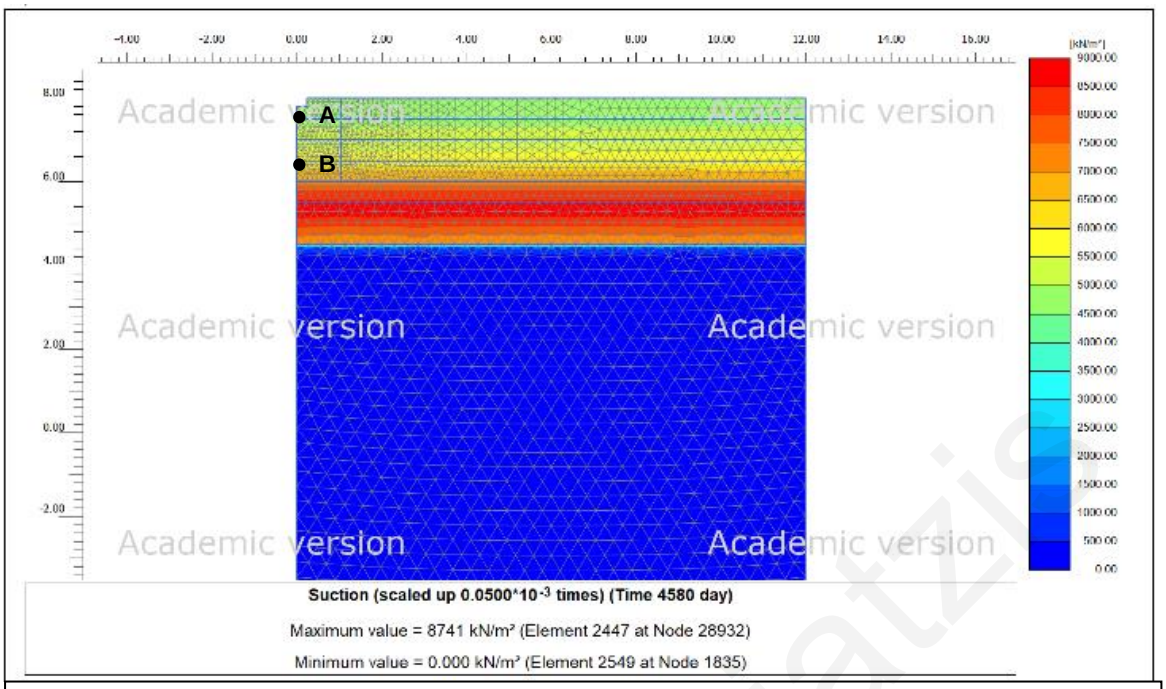

● Pair of Teros 21 matric suction and Teros 12 volumetric water content sensors at A: 0.67 m depth and side distance 0.7 m and B: 1.4 m depth.

Figure 72. Contours of soil suction at the end of the preparation digging for the wetting phase from simulation for Site 2.

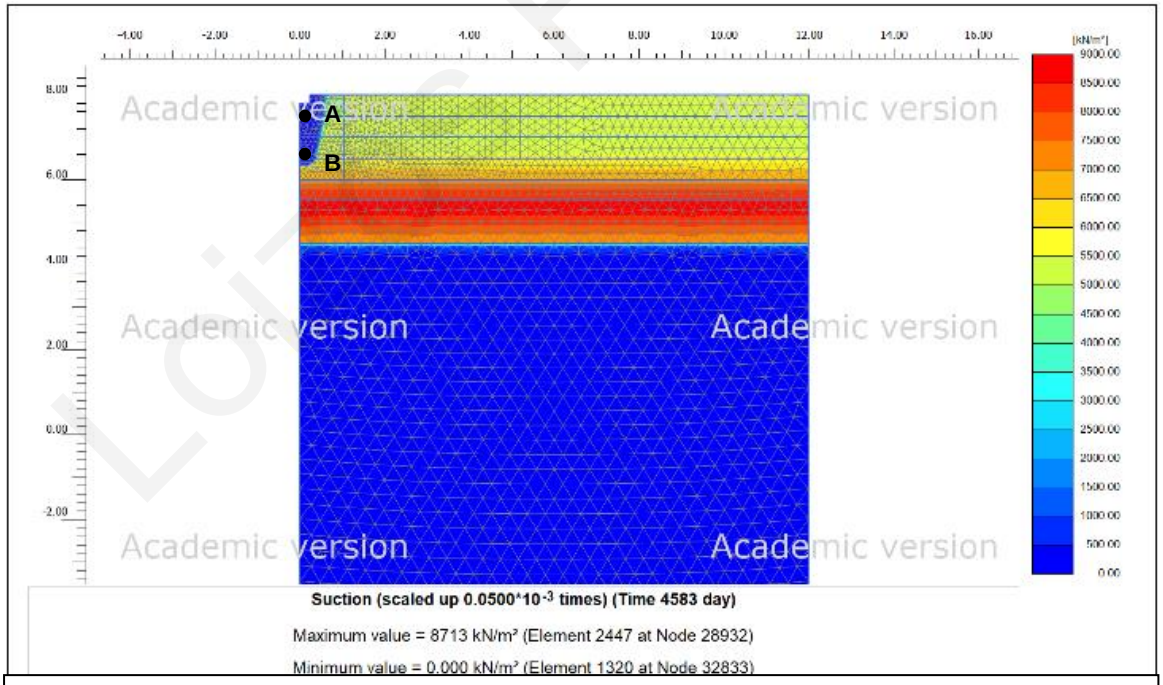

● Pair of Teros 21 matric suction and Teros 12 volumetric water content sensors at A: 0.67 m depth and side distance 0.7 m and B: 1.4 m depth.

Figure 73. Contours of soil suction at the end of the wetting phase from simulation for Site 2.

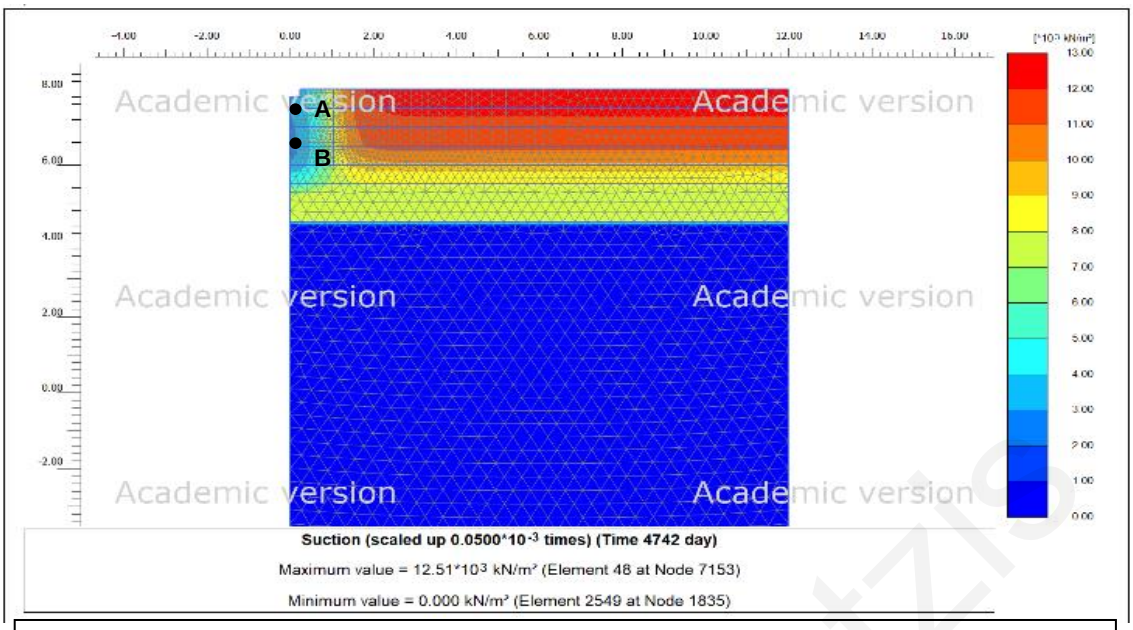

● Pair of Teros 21 matric suction and Teros 12 volumetric water content sensors at A: 0.67 m depth and side distance 0.7 m and B: 1.4 m depth.

Figure 74. Contours of soil suction at the end of the desaturation phase from simulation for Site 2.

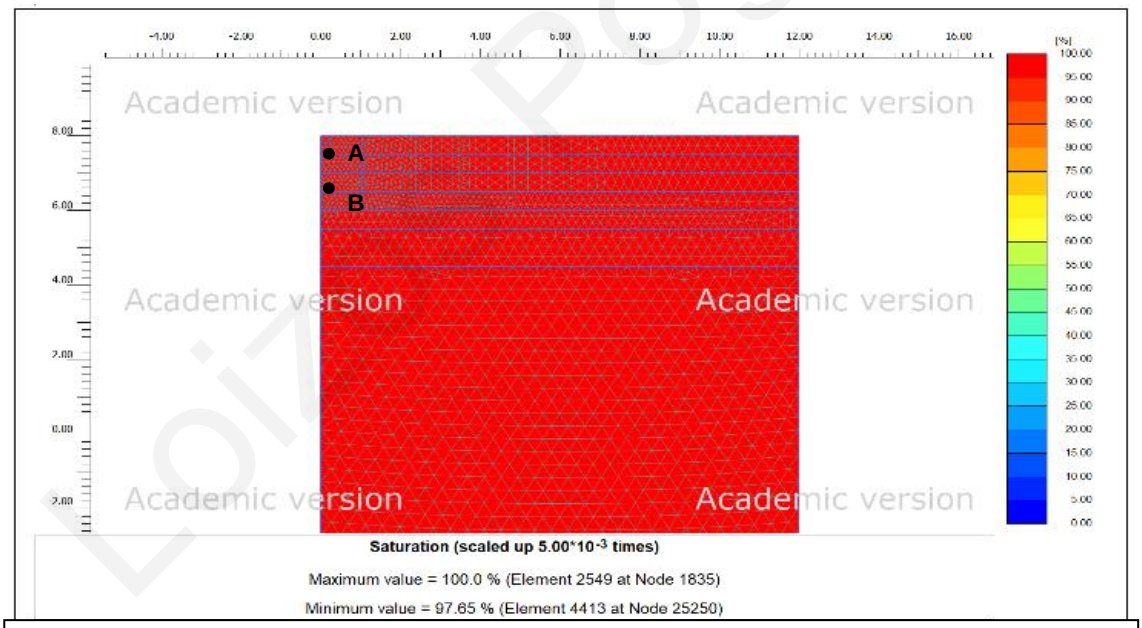

● Pair of Teros 21 matric suction and Teros 12 volumetric water content sensors at A: 0.67 m depth and side distance 0.7 m and B: 1.4 m depth.

Figure 75. Contours of degree of saturation at the end of the initial phase from simulation for Site 2.

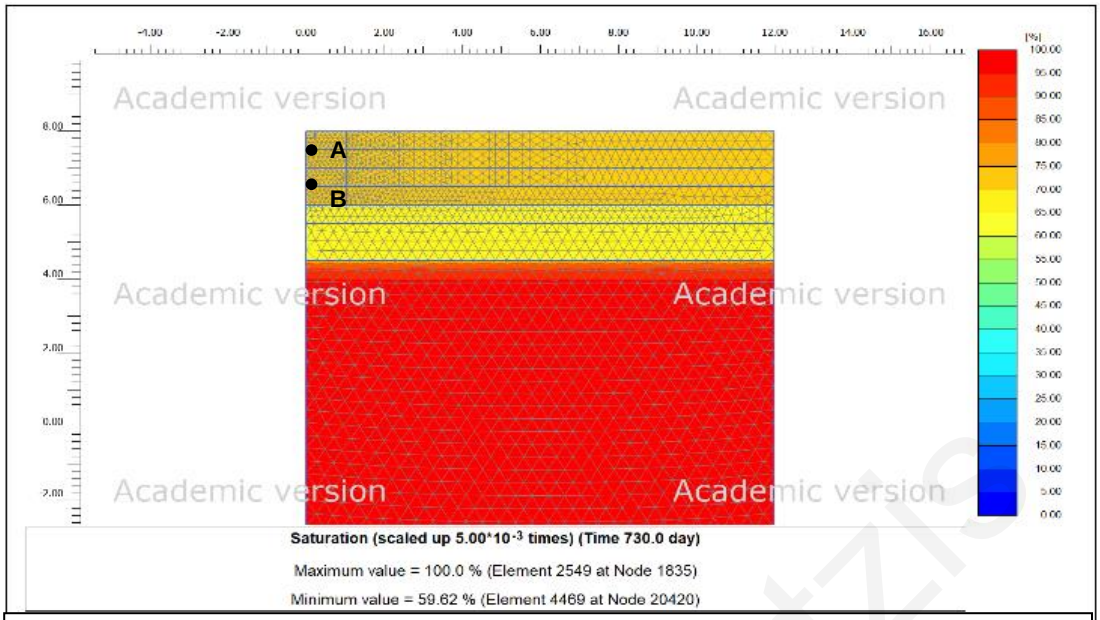

● Pair of Teros 21 matric suction and Teros 12 volumetric water content sensors at A: 0.67 m depth and side distance 0.7 m and B: 1.4 m depth.

Figure 76. Contours of degree of saturation at the end of the 1st dummy year from simulation for Site 2.

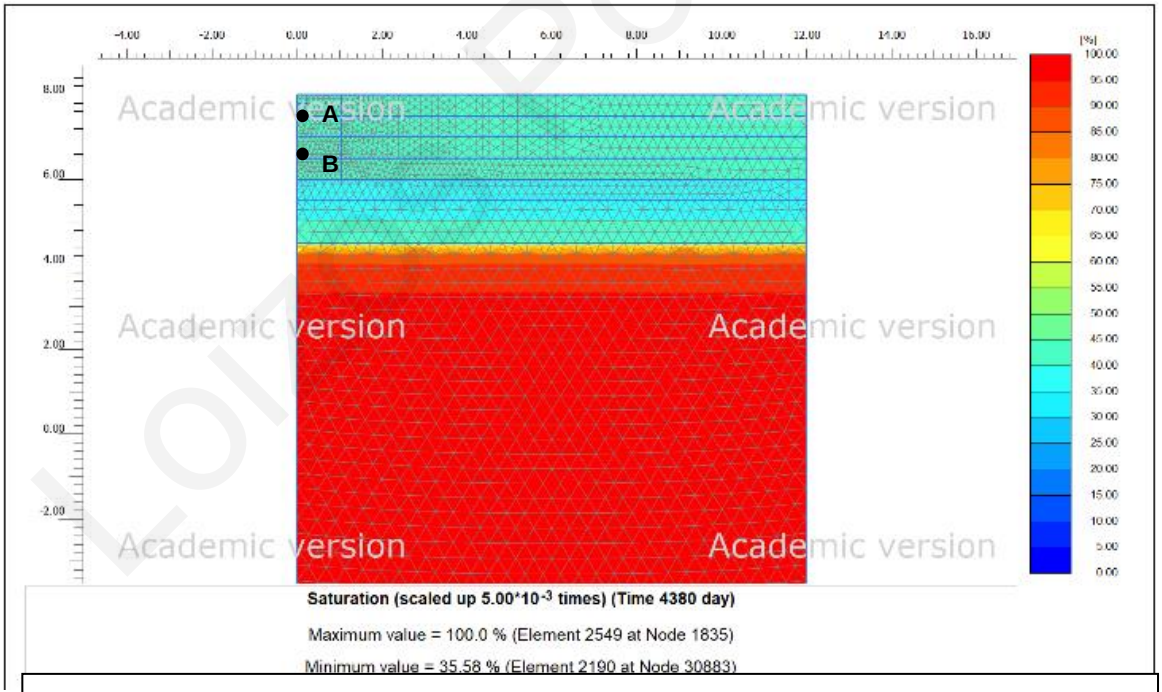

● Pair of Teros 21 matric suction and Teros 12 volumetric water content sensors at A: 0.67 m depth and side distance 0.7 m and B: 1.4 m depth.

Figure 77. Contours of degree of saturation at the end of the 6th (last) dummy year from simulation for Site 2.

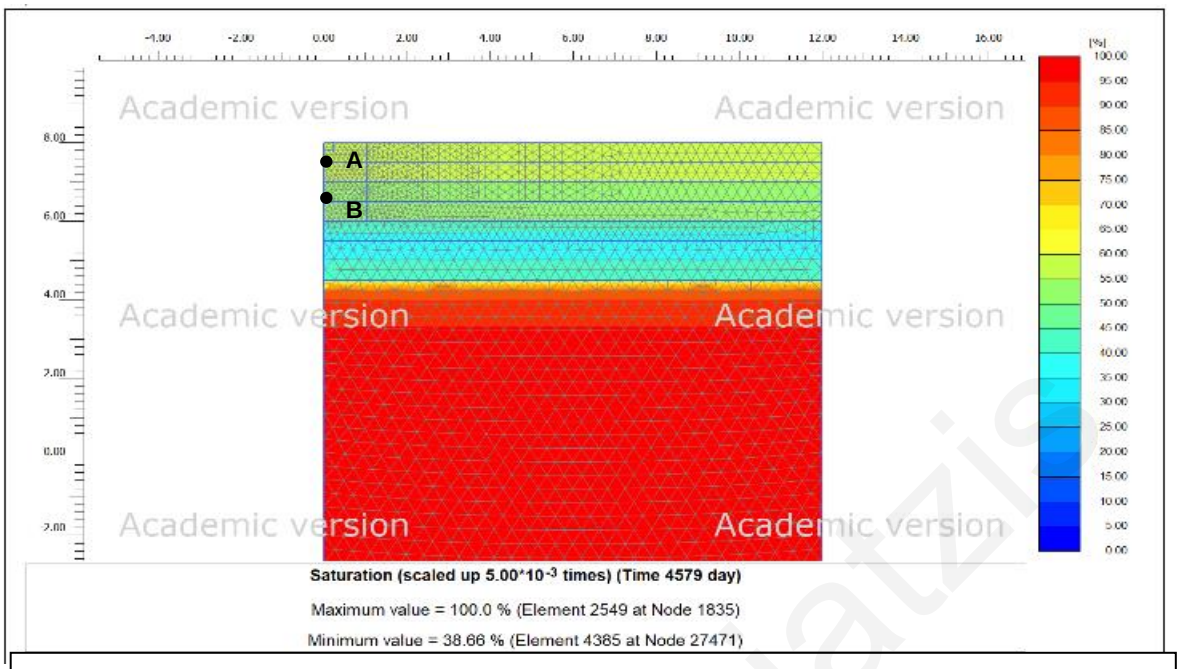

● Pair of Teros 21 matric suction and Teros 12 volumetric water content sensors at A: 0.67 m depth and side distance 0.7 m and B: 1.4 m depth.

Figure 78 . Contours of degree of maximum value of soil saturation from simulation for Site 2.

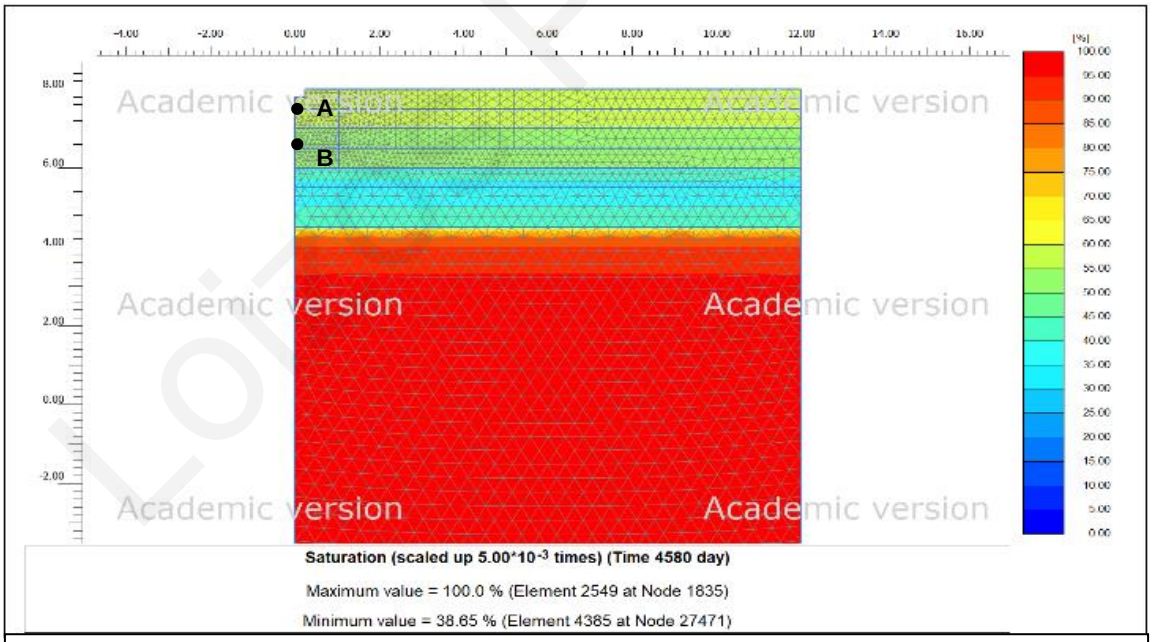

● Pair of Teros 21 matric suction and Teros 12 volumetric water content sensors at A: 0.67 m depth and side distance 0.7 m and B: 1.4 m depth.

Figure 79. Contours of degree of saturation at the end of the preparation digging for the wetting phase from simulation for Site 2

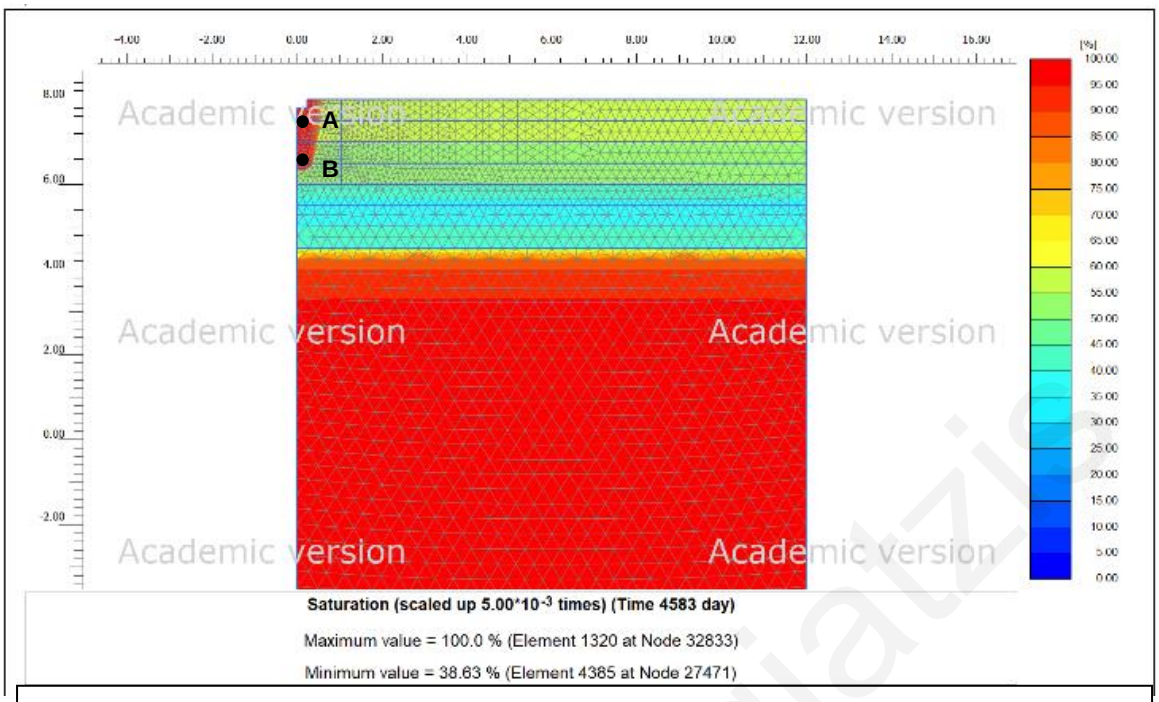

● Pair of Teros 21 matric suction and Teros 12 volumetric water content sensors at A: 0.67 m depth and side distance 0.7 m and B: 1.4 m depth.

Figure 80. Contours of degree of saturation at the end of the wetting phase from simulation for Site 2.

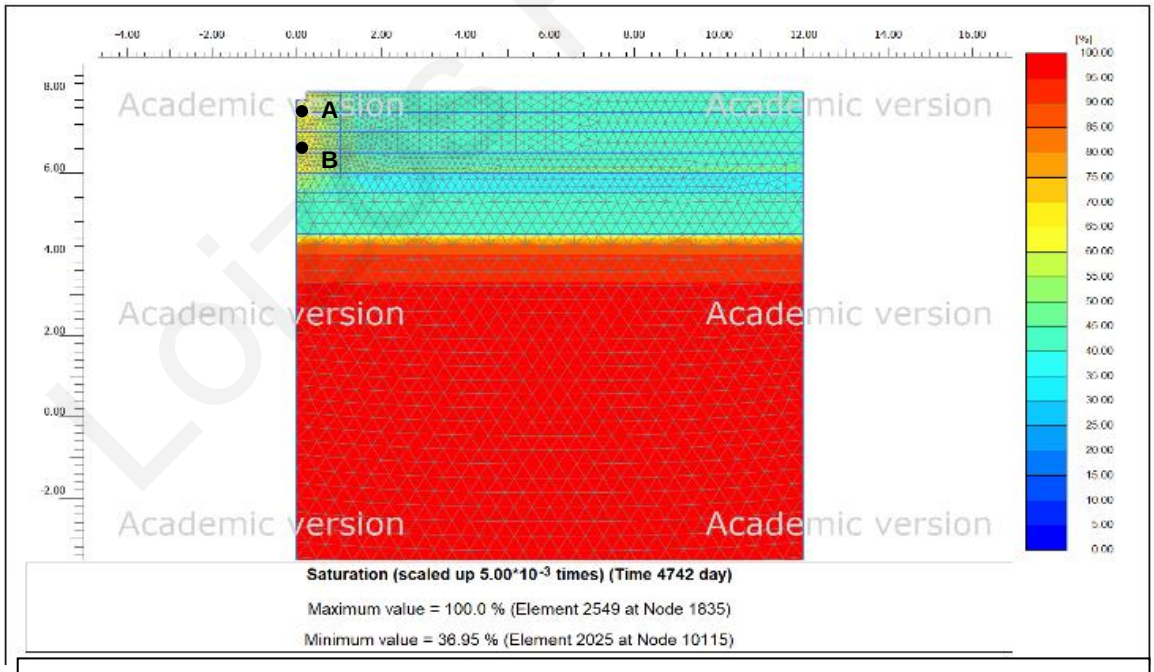

● Pair of Teros 21 matric suction and Teros 12 volumetric water content sensors at A: 0.67 m depth and side distance 0.7 m and B: 1.4 m depth.

Figure 81. Contours of degree of saturation at the end of the desaturation phase from simulation for Site 2.

5.2.3 Site 3

Fig. 82 shows comparison of the best possible saturation time-history curves obtained from Plaxis FEA after several trial simulation with the time history inferred from the ground sensor measurements. The $k_{y,sat}$, $k_{x,sat}$ and g_l parameters established through the trial-and-error process are shown in Table 10. It can be seen that the equivalent permeability close to the ground surface (down to 1m depth) turns out to be 5500 times larger than the value below 3.5m depth, which corresponds to the intact marl. The increased permeability, which gradually decreases with depth, is mostly due desiccation cracks, which were evident on the ground surface during the summer period of 2021. Fissures were observed in the marl during excavation of the trial pit, but (unlike Site 2) with little to no opening .

Table 10. Equivalent ground permeability parameters established via trial-and-error simulations for Site 3.

sub-layer	$k_{y,sat}$ (m/day)	$k_{y,sat}$ (cm/s)	$k_{x,sat}$ (m/day)	$k_{x,sat}$ (cm/s)	g_l
1	3.33×10^{-2}	3.85×10^{-5}	9.51×10^{-4}	1.1×10^{-6}	50
2	3.33×10^{-2}	3.85×10^{-5}	9.51×10^{-4}	1.1×10^{-6}	40
3	2.22×10^{-2}	2.57×10^{-5}	1.39×10^{-4}	1.61×10^{-7}	7
4	8.32×10^{-3}	9.63×10^{-6}	5.00×10^{-5}	5.79×10^{-8}	3
5	2.77×10^{-3}	3.21×10^{-6}	3.10×10^{-5}	3.59×10^{-8}	3
6	5.50×10^{-5}	6.37×10^{-8}	6.00×10^{-6}	6.94×10^{-9}	1
7	6.00×10^{-6}	6.94×10^{-9}	6.00×10^{-6}	6.94×10^{-9}	1

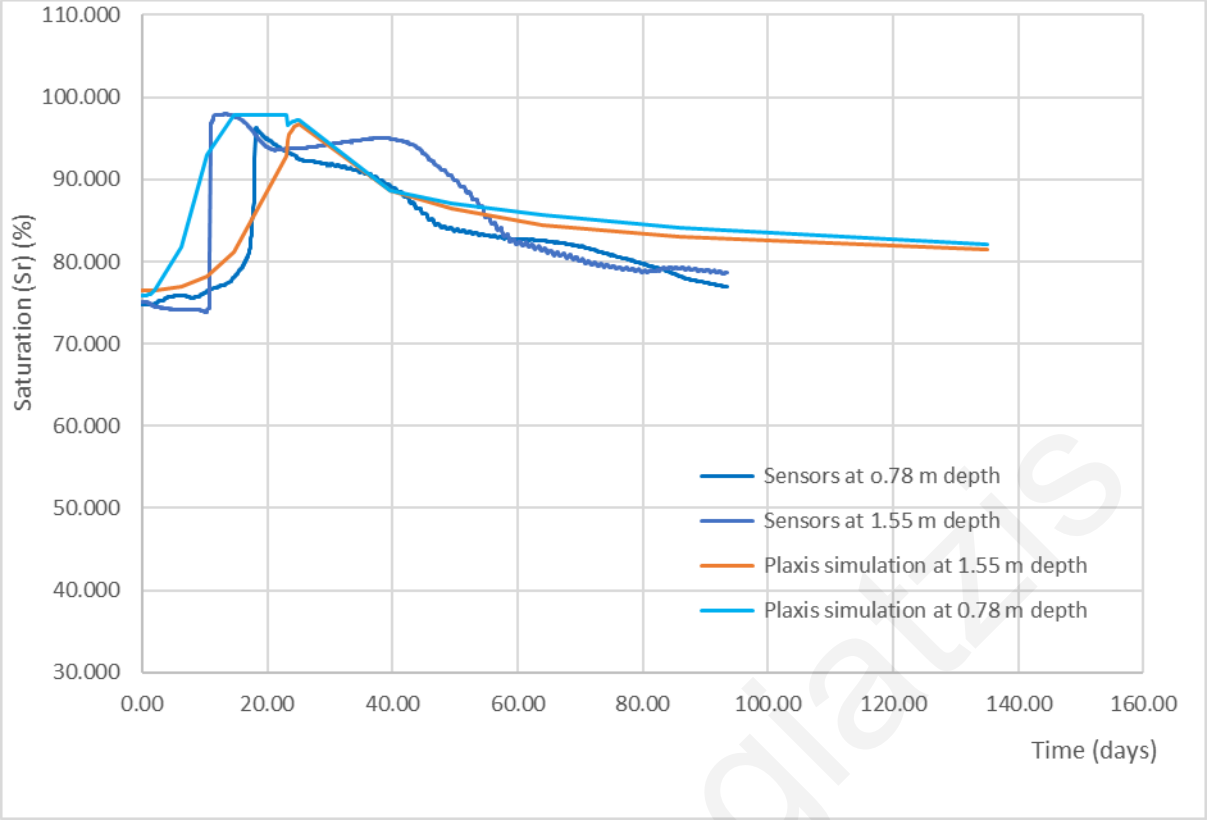

Figure 82. Plaxis simulation graph of Test pit 3 and wetting experiment data of Site 3-BH 3 showing the evolution of saturation with time using the data of the field sensors.

Figs.83-89 show the evolution of the distribution of suction *s* in the soil profile during various stages of the finite element analysis (initial phase, first dummy year, last dummy year, end of wetting phase, end of desaturation phase), while Figs. 90-96 show the corresponding distribution of degree of saturation S_r. It can be seen that in the in-situ suction values at the upper 4m of the profile are larger than 4MPa. Compared to the cases of the two previous sites, the saturation bulb in Site 3 is wider due the more intense diffusion during desaturation caused by the stronger water retention of this highly plastic Nicosia marl.

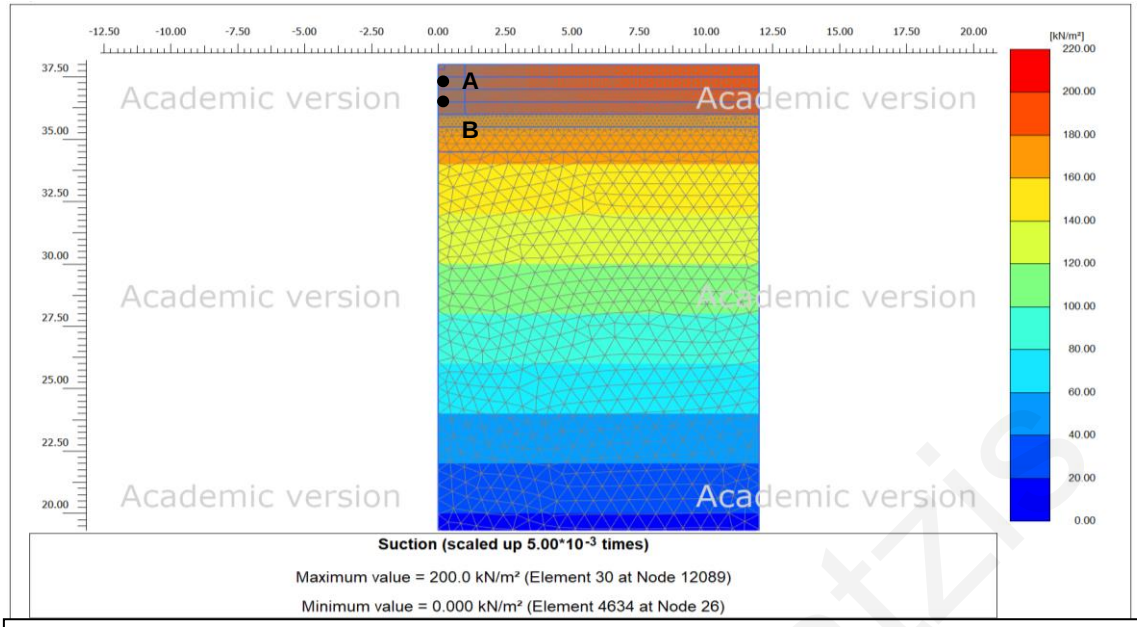

● Pair of Teros 21 matric suction and Teros 12 volumetric water content sensors at A: 0.78 m depth and side distance 0.6 m and B: 1.56 m depth.

Figure 83. Contours of soil suction at the end of the initial phase from simulation for Site 3.

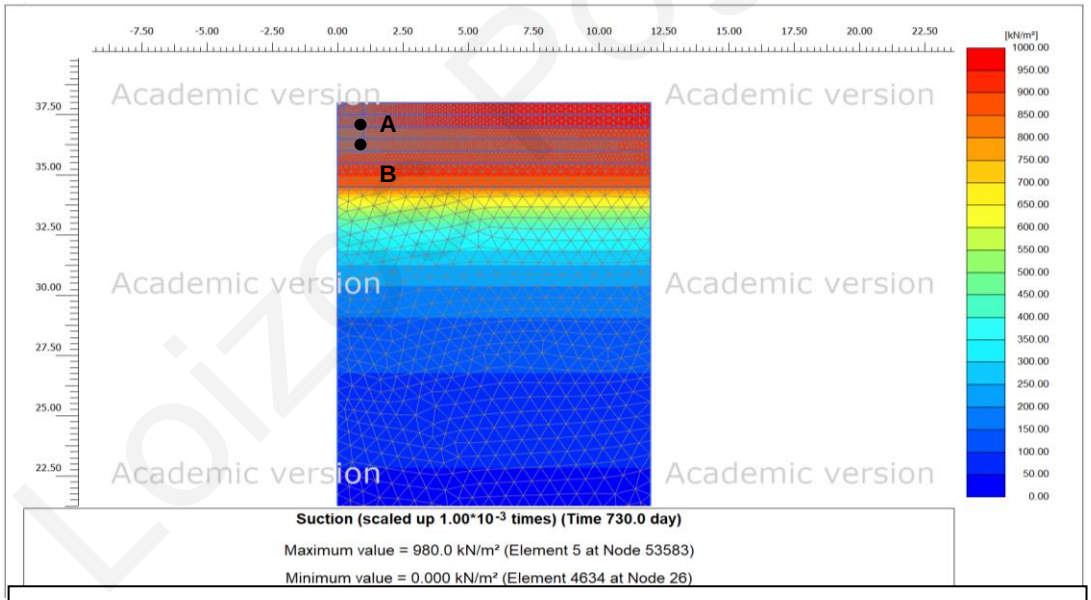

● Pair of Teros 21 matric suction and Teros 12 volumetric water content sensors at A: 0.78 m depth and side distance 0.6 m and B: 1.56 m depth.

Figure 84. Contours of soil suction at the end of the 1st dummy Year from simulation for Site 3.

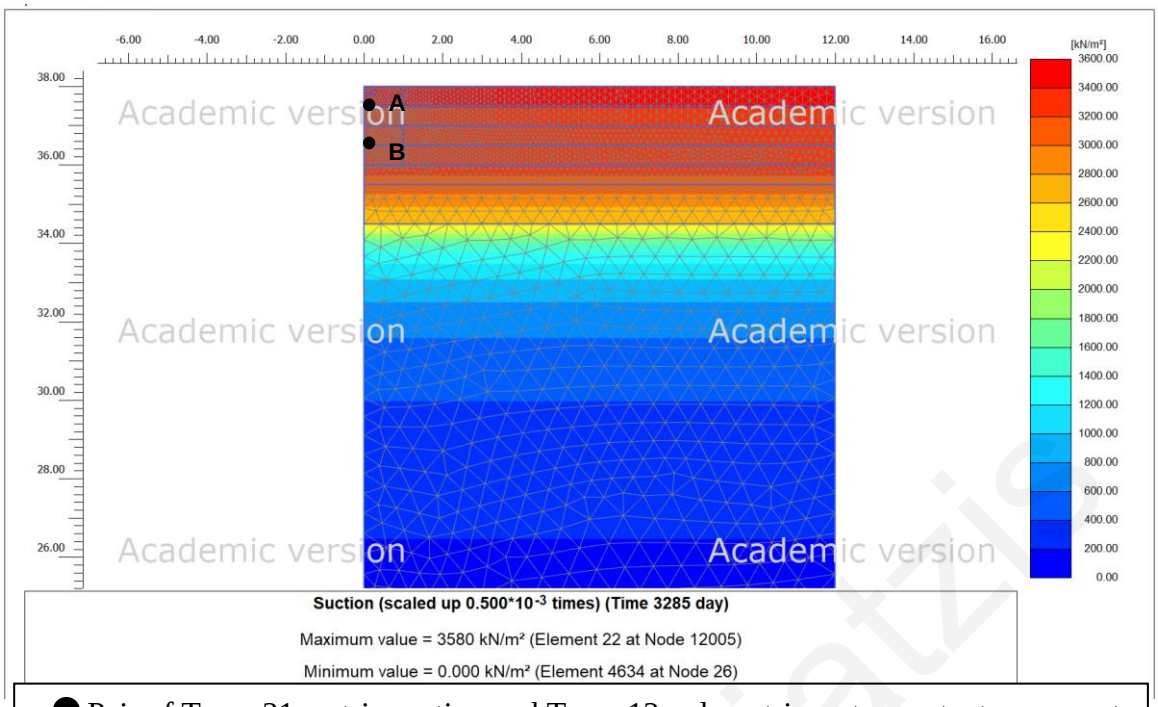

● Pair of Teros 21 matric suction and Teros 12 volumetric water content sensors at A: 0.78 m depth and side distance 0.6 m and B: 1.56 m depth.

Figure 85. Contours of soil suction at the end of the 5th dummy Year from simulation for Site 3.

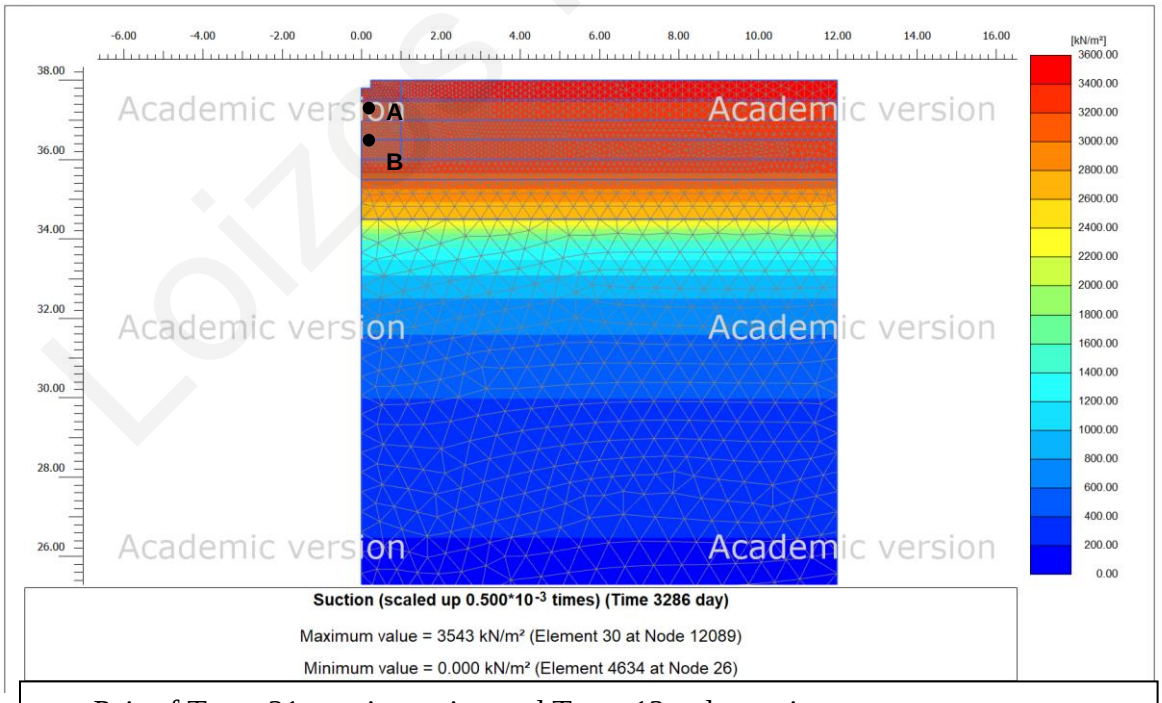

● Pair of Teros 21 matric suction and Teros 12 volumetric water content sensors at A: 0.78 m depth and side distance 0.6 m and B: 1.56 m depth.

Figure 86. Contours of soil suction at the end of the preparation digging for the wetting phase from simulation for Site 3.

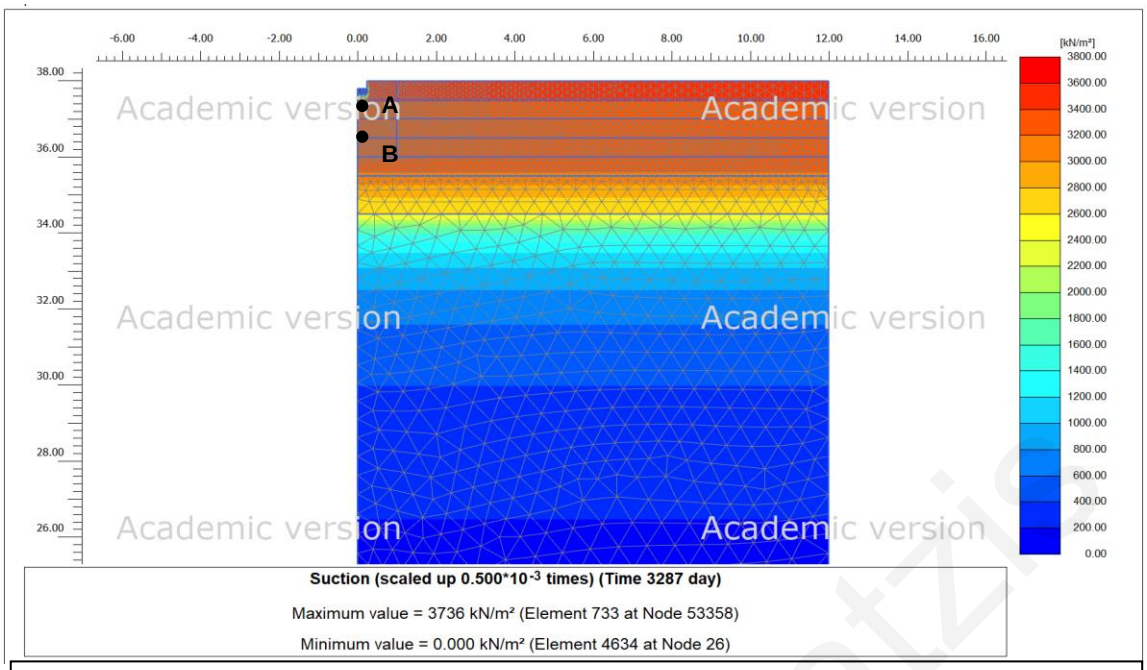

● Pair of Teros 21 matric suction and Teros 12 volumetric water content sensors at A: 0.78 m depth and side distance 0.6 m and B: 1.56 m depth.

Figure 87. Contours of soil suction at the initialization of the wetting phase from simulation for Site 3.

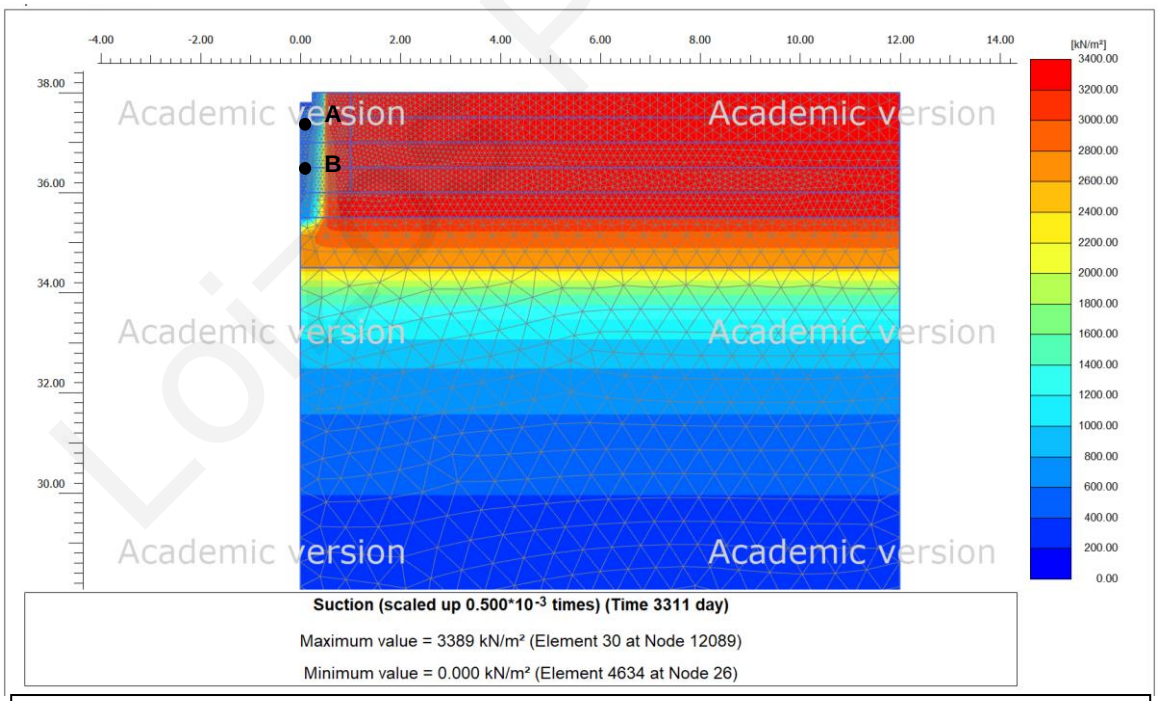

● Pair of Teros 21 matric suction and Teros 12 volumetric water content sensors at A: 0.78 m depth and side distance 0.6 m and B: 1.56 m depth.

Figure 88. Contours of soil suction at the end of the wetting phase from simulation for Site 3.

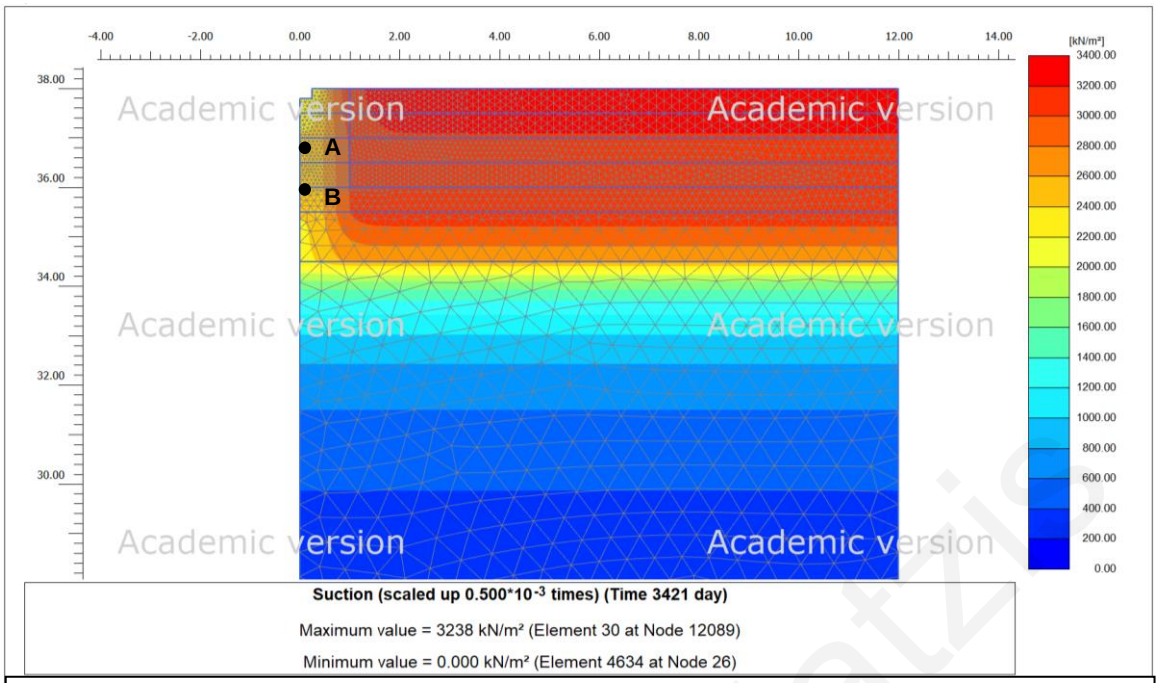

● Pair of Teros 21 matric suction and Teros 12 volumetric water content sensors at A: 0.78 m depth and side distance 0.6 m and B: 1.56 m depth.

Figure 89. Contours of soil suction at the end of the desaturation phase from simulation for Site 3.

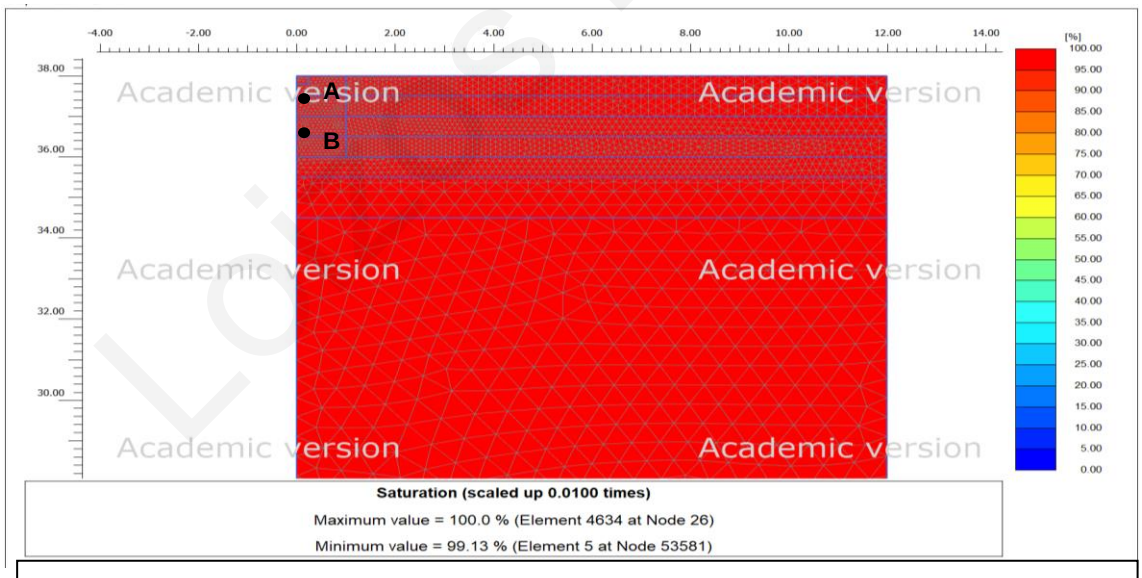

● Pair of Teros 21 matric suction and Teros 12 volumetric water content sensors at A: 0.78 m depth and side distance 0.6 m and B: 1.56 m depth.

Figure 90. Contours of degree of saturation at the end of the initial phase from simulation for Site 3

● Pair of Teros 21 matric suction and Teros 12 volumetric water content sensors at A: 0.78 m depth and side distance 0.6 m and B: 1.56 m depth.

Figure 91. Contours of degree of saturation at the end of the 1st dummy year from simulation for Site 3.

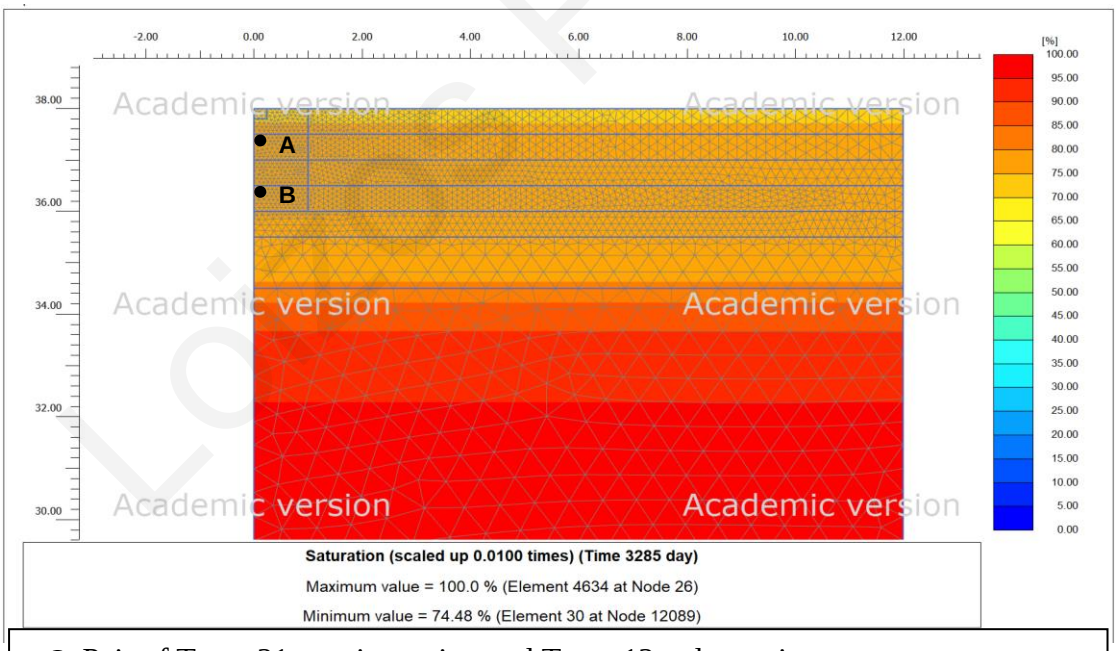

● Pair of Teros 21 matric suction and Teros 12 volumetric water content sensors at A: 0.78 m depth and side distance 0.6 m and B: 1.56 m depth.

Figure 92. Contours of degree of saturation at the end of the 5th dummy Year from simulation for Site 3.

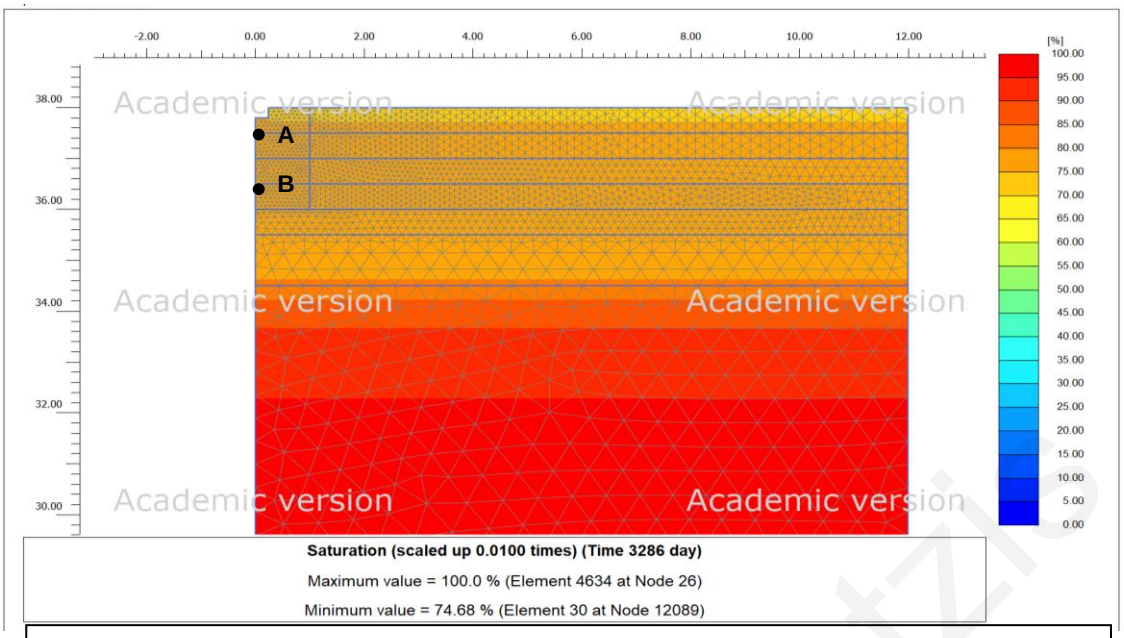

● Pair of Teros 21 matric suction and Teros 12 volumetric water content sensors at A: 0.78 m depth and side distance 0.6 m and B: 1.56 m depth.

Figure 93. Contours of degree of saturation at the end of the preparation digging for the wetting phase from simulation for Site 3.

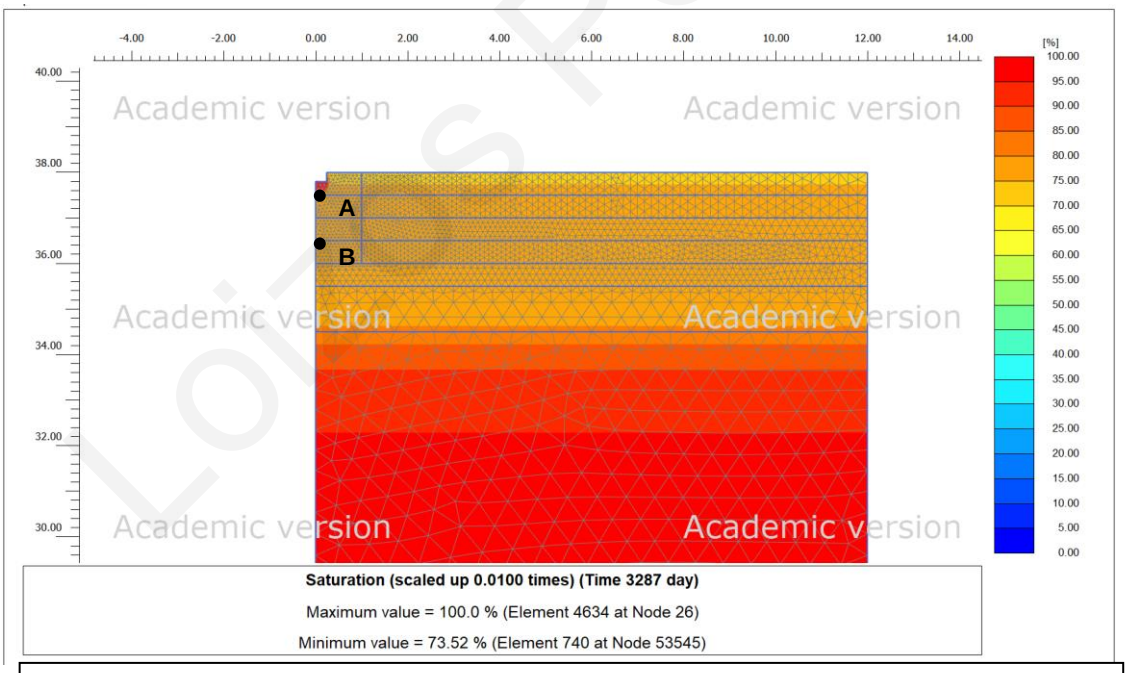

● Pair of Teros 21 matric suction and Teros 12 volumetric water content sensors at A: 0.78 m depth and side distance 0.6 m and B: 1.56 m depth.

Figure 94. Contours of degree of saturation at the initialization of the wetting phase from simulation for Site 3.

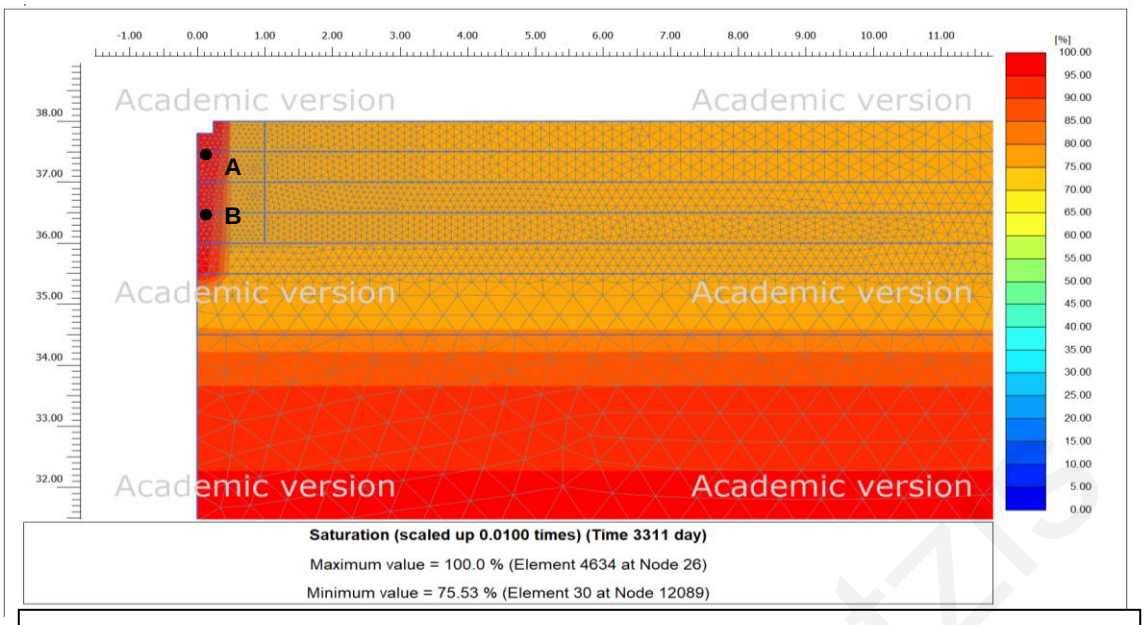

● Pair of Teros 21 matric suction and Teros 12 volumetric water content sensors at A: 0.78 m depth and side distance 0.6 m and B: 1.56 m depth.

Figure 95. Contours of degree of saturation at the end of the wetting phase from simulation for Site 3.

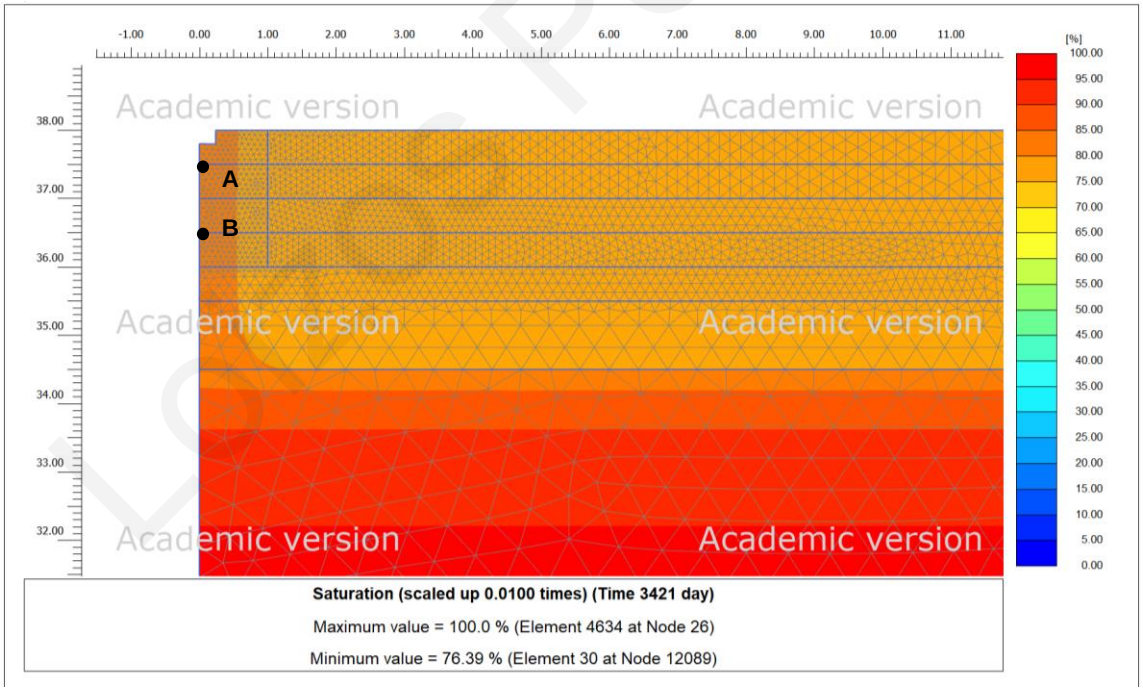

● Pair of Teros 21 matric suction and Teros 12 volumetric water content sensors at A: 0.78 m depth and side distance 0.6 m and B: 1.56 m depth.

Figure 96. Contours of degree of saturation at the end of the desaturation phase from simulation for Site 3

6. CONCLUSIONS

This research investigated the in-situ permeability of Nicosia marl, in an effort to understand the potential of infiltration and migration of rainwater inside the unsaturated zone. Initially the soil-water characteristic curves from three different sites at the University of Cyprus campuses were determined using a chilled mirror hygrometer and samples were examined by laboratory testing to determine the physical and mechanical properties of the soil. Then, the data acquired by installed field volumetric water content and matric suction monitoring sensors were used in FE simulations for the back calculation of the in-situ permeability in both vertical and horizontal direction.

The main findings of this research can be summarized as follows:

1. Nicosia marl has a very large water retention potential, with exception the marl encountered at the top layer in BH2 due to its lower clay content.
2. Total suction in the upper 2m of the active zone has very high values of the order of MPa's.
3. Nicosia marl appears to be almost saturated several meters higher than the water level due to capillary suction.
4. SWCC hysteresis becomes important for the highly plastic marl of the old campus of the University of Cyprus.
5. The variations of saturation with depth depend on the characteristic soil-water curve (SWCC) and the hydraulic properties of the soil profile. Large values of the parameter g_a indicating less active soil combined with low permeability values, give a small range of humidity impact.
6. The penetration of water into the ground, which will undoubtedly change the degree of saturation and eventually will change the shape of the characteristic curve at the beginning of the winter period is done rapidly through the drying cracks that were created during the dry season.
7. The equivalent in-situ vertical permeability (under full saturation conditions) is found to be 3 to 4 orders of magnitude larger than that for the intact material. More specifically, its value is of the order of 10^{-4} cm/s for all three examined sites. This is due to the presence of inherent fissures and desiccation cracks. The horizontal

permeability appears to be 1 to 3 orders of magnitude smaller than the one for the vertical direction.

8. The bulb of full saturation during ground wetting is relatively narrow and progresses mostly in the vertical direction, partly because of the lower hydraulic permeability values set in the horizontal direction.
9. Despite the large number of tests performed, the analyses fail to match closely field sensor recordings, including the desaturation part of the experiment. This is most likely due to i) the effects of SWCC hysteresis which is not included in the Plaxis mathematical formulation and ii) the closing and reopening of the desiccation cracks of the marl which may alter dramatically the permeability during the course of the wetting experiment.

Recommendations for future research

Despite the existence of a plethora of new mathematical simulation models that consider the effect of hysteresis of the SWCC in contrast with the original van Genuchten's (1980) model, any of them so far is not widespread and commonly accepted, so it is recommended to perform more trials with different models, to understand which models mimic better the real in-situ conditions of the soil.

BIBLIOGRAPHY

Barnes, G. (2016). Soil mechanics: principles and practice. Macmillan International Higher Education.

Braddock, R., Parlange, J.-Y. & Lee, H. (2001). Application of a Soil Water Hysteresis Model to Simple Water Retention Curves. *Transport in Porous Media* , 407–420.

Clinton, T. (2015). Electokinetic Stabilisation as a Subsidence Remediation Technique. Birmingham.

Constantinou, G., Panagides, I., Xenophontos, K., Afrodisis, S., Michaelides, P. & Kramvis, S. (Bulletin No. 10, 2002). *The geology of Cyprus*, Cyprus Geological Survey Department.

Eyo, E. U., Ng'ambi, S. & Abbey, S. J. (2020). An overview of soil–water characteristic curves of stabilised soils and their influential factors. Coventry, United Kingdom.

Fernandez, F. & Quigley, R. (1989). Organic liquids and the hydraulic conductivity of barrier clays. (pp. 1867-1870). Rotterdam, Netherlands: Publ by A.A. Balkema.

Galavi, V. (2010). G*roundwater flow, fully coupled flow deformation and undrained analyses in PLAXIS 2D and 3D*. Internal Report, Delft, Netherlands: PLAXIS bv Research Department.

Head, K. & Epps, R. (2006). *Manual of Soil Laboratory Testing.* Dunbeath: Whittles Publishing.

Hobbs, P.R.N., Loucaides, G. & Petrides, G. (1986). *Geotechnical properties and behaviour of Pliocene marl in Nicosia, Cyprus*. British Geological Survey Rep. No. EGARP-KW/86/1 and Geological Survey Department, Cyprus Rep. No. GJEG/12.

Lazarou, G., Loukidis, D. & Bardanis, M. (2019). Moisture migration under mat foundations in Nicosia Marl. *Geotechnical and Geological Engineering*, 37(3), 1585-1608.

Lazarou, G. M. (2020). *Investigation of the effect of swelling/shrinkage of clays on the analysis and design of mat foundations.* PhD Thesis, University of Cyprus, Nicosia, Cyprus.

Liaki, C. (2006). Physicochemical study of electrokinetically treated clay using carbon and steel electrodes. Birmingham.

Likos, W., ASCE, M., Lu, N., ASCE, F. & Godt, J. (2013). Hysteresis and Uncertainty in Soil Water-Retention Curve Parameters. *American Society of Civil Engineers.*

Loukidis, D., Bardanis, M. & Lazarou, G. (2016). Classification, soil-water characteristic curve and swelling/collapse behaviour of the Nicosia marl, Cyprus. *3rd European Conference on Unsaturated Soils – "E-UNSAT 2016"*, (p. 6).

Loukidis, D., Tzampoglou, P., Lazarou , G. & Stylianou, T. (2020). *"EXPASOL - The effects of soil expansion/shrinkage on building foundations and their mitigation.Interim technical report",* Project INTEGRATED/09160049,University of Cyprus, Nicosia. Nicosia.

Lu, N. & Likos, W. (2004). *Unsaturated soil mechanics.* Hoboken, New Jersey, Canada: John Wiley & Sons, Inc.

Mady, A. & Shein, E. (2020). Assessment of pore space changes during drying and wetting cycles in hysteresis of soil water retention curve in Russia using X-ray computed tomography. *Geoderma Regional*.

Miller, G. A., Khoury, C. N., Muraleetharan, K. K., Liu, C. & Kibbey, T. C. (2008). Effects of soil skeleton deformations on hysteretic soil water characteristic curves:Experiments and simulations. *Water Resources Research,* vol 46.

Mitchell, J. & Soga, K. (2005). *Fundamentals of Soil Behavior* (3rd ed.). Hoboken, N.J. : Wiley, 2005.

Pham, H., Fredlund, D. & Barbour, S. (2005). A study of hysteresis models for soil-water characteristic curves. *Can. Geotech. J. 42*, 1548–1568.

Satyanaga, A., Kim, J., Moon, S.-W. & Wijaya, M. (2020). Exponential Functions for Modelling Hysteresis of Soil-Water Characteristic Curves. *E3S Web of Conferences 195, 02002E-UNSAT.*

van Genuchten, M.T (1980). A closed-form equation for predicting the hydraulic conductivity of unsaturated soils. Soil Science Society of American Journal, vol. 44(5), p. 892–898.

Wang, A. & Wang, W. (2019). *Nanomaterials from Clay Minerals: A New Approach to Green Functional Materials.* Elsevier Inc.

Williams, L. & Shelley, H. (2010). Evaluation of the medical use of clay minerals as antibacterial agents. International geology review. *International geology review.*, 745-770.